Zhang Zhaoqiang

IRONLESS PERMANENT MAGNET GENERATORS FOR DIRECT-DRIVEN OFFSHORE WIND TURBINES

O NTNU
Kunnskap for en bedre verden

Acknowledgements

First and foremost, the deepest appreciation goes to my supervisor Professor Robert Nilssen. His support is overall and far beyond the technical aspect. Having the opportunity to feel his tolerance, kindness, and wisdom is a treasure that I would cherish and share in my life.

I would like to thank my co-supervisor Professor Arne Nysveen for his valuable comments on papers. I also thank Doctor S. M. Muyeen, my co-supervisor in the Petroleum Institute, United Arab Emirates, for a short stay in his laboratory where we worked together on common interest.

I wish to express my sincere thanks to SmartMotor AS and Doctor Alexey Matveev, Head of Research in SmartMotor AS, for supplying the test machine, instruction on the research topics, and important comments on papers.

Meanwhile, I thank service team at the Department of Electric Power Engineering for the assistance of building the test setup, and NTNU HPC Group for the access to super computers and the support of software compiling.

I also express my gratitude to Ms. Astrid Røkke who helped improving the language of several chapters.

Finally, I am grateful to my colleagues at the Department of Electric Power Engineering, and to all who, directly or indirectly, gave their support during the course of this project.

Abstract

Since the beginning of this century, the offshore wind power industry has witnessed fast development, as the result of the increasing awareness of climate change and the need for diversifying power supply. Offshore has vast area available with high wind speed, which is an ideal place for large-scale wind power exploitation. However, these advantages come with technological challenges.

One of the key challenges is to develop high-power cost-effective wind turbines with high reliability. Previous publications have demonstrated the potential of using ironless permanent magnet generator (iPMG) to reduce the total weight and cost of a wind turbine. Unfortunately, before the start of the research reported in this thesis, there was no systematic investigation of the iPMG concepts.

As shown in this thesis, if the traditional direct-driven high-power iron-cored PMG is used for offshore wind turbines, instead of iPMG concept, a significant amount of the total weight goes to the supporting structures (inactive parts). The supporting structures maintain the machine reliability by counter-reacting to various forces, such as the machine gravity, electromagnetic torque, rotor-to-stator force (for iron-cored machine), rotor-to-rotor force (if there are multiple rotors), and force caused by faults. The "secret" of iPMG roots at the negligible normal stress between its rotor and stator (active parts). By using non-magnetic material in the stator, the rotor will not exert attracting force on stator. Having low rotor-to-stator force means lower requirement to the supporting structures, i.e., the supporting structures can be lightweight and low-cost.

Due to the low air gap field and thus low tangential stress, iPMG has low torque production. Therefore, iPMG is normally designed with large diameter to produce higher torque with longer force arm.

Classical machine design theory has concluded that the machine torque is roughly proportional to its volume. A large-diameter iPMG will therefore have short axial length, which means small aspect ratio (the machine axial length divided by its outer diameter). This ring-shape feature requires 3D approach to analyse the magnetic and thermal fields. Traditionally, it is a common practice to do machine preliminary design and optimization with analytical methods. The 2D or even 3D finite element method (FEM) is considered to be accurate but time-consuming, though the performances of computing codes and

hardware are being steadily improved. Multi-core computers and distributed-memory clusters are normally available to most machine designers. Some academic users even have the access to super computers.

The objective of this research is to investigate the iPMG technologies with the help of advanced modelling approaches. The main results reported in this thesis are

- An overview of the ironless permanent magnet machines (iPMM) (Chapter 1).

- A comprehensive overview of the generator technologies for operational offshore wind turbines, the comparison of the efficiencies for different drive trains, and a review of the new generator concepts (Chapter 2).

- A method for evaluating the goodness of any generator design and predicting the generator total weight, and a design and optimization strategy for investigating the weight variation of iron-cored high-power PMGs (Chapter 3).

- A design and optimization strategy for investigating the performances of various single-stage and multi-stage iPMGs (Chapter 4 and 5).

- A comparison of 10-MW iron-cored PMG and iPMG (Chapter 4).

- A 3D multiphysics design approach where all the calculations are done with open source codes (Chapter 6).

- An investigation of the machine efficiency improvement with the instantaneous ABC theory borrowed from power system theory (Chapter 7).

It is also the aim to explore the frontier of machine modelling techniques. In this thesis, different calculation codes are used, including both open source codes and commercial codes. The machine modelling covers 1D, 2D, and 3D approaches. The computing resources used range from ordinary PCs, multiple workstations, a computing server, and a super computer (tried). To assist this research and other computation-demanding projects, a scientific computing lab was built with the financial support from the Department of Electric Power Engineering. The modelling approach was validated with an existing 23-kW axial-flux iPMG provided by SmartMotor AS.

The main conclusions are: Geared drive trains with induction generators are the dominant solutions in offshore wind farms. Direct-driven iron-cored PMGs are heavy and expensive, and most of the weight and cost go to their inactive parts, which makes this solution not weight-/cost-effective. iPMMs are normally used in low-power (several kW) high-speed (above 1000 rpm) applications. Using iPMM technology in high-power (e.g. 10 MW) low-speed (e.g. 12 rpm) offshore wind turbines can significantly reduce the generator cost and weight. It is preferred to build a machine at single stage rather than multiple stages in terms of torque density and efficiency. For a single-stage iPMG solution, two-rotor conventional-array PMGs have the optimal performances among all the

investigated topologies, and the performance difference between radial flux and axial flux PMGs gets reduced when their outer diameters are greater than 25 m. Multi-stage solution may outperform the single-stage solution, if the machine outer diameter is constrained and the design has multiple objectives. At 10 MW level, a 12-rpm single-stage iPMG with a diameter of 20 m is lighter and less expensive than a 12-rpm iron-cored PMG with a diameter of 9.9 m. Even though the state of the art commercial finite-element-analysis and genetic-algorithm codes are used, and the specially developed design and optimization strategy can reduce the total calculation time, it takes a week to ten days to solve an optimization with five free variables. A 3D multiphysics design and optimization strategy can take into account the effects due to small aspect ratio of iPMGs, and executing such a strategy with open source codes on a super computer can reduce the computational cost, but it is still a challenge to parallelize the calculation and optimization. An active shunt filter controlled with the instantaneous ABC theory can reduce the generator loss, but the system efficiency is not significantly improved. Nonetheless, it is still attractive to use the diode rectifier in a converter as a trade-off of cost, reliability, and power yield.

Following publications are produced during the course of the project.

Journal papers:

- Z. Zhang, A. Chen, A. Matveev, R. Nilssen, and A. Nysveen, "High-power generators for offshore wind turbines," *Energy Procedia*, vol. 35, pp. 52-61, 2013. Chapter 2.

- Z. Zhang, A. Matveev, R. Nilssen, and A. Nysveen, "Ironless permanent magnet generator for offshore wind turbines," *IEEE Trans. Ind. Appl.*, vol. 50, No. 3, pp. 1835-1846, 2014. Chapter 4.

- Z. Zhang, S. M. Muyeen, A. Al-Durra, R. Nilssen, and A. Nysveen, "Multiphysics modelling of ironless permanent magnet generators," *Energy Procedia*, vol. 53, pp. 34-43, 2014. Chapter 6.

- Z. Zhang, R. Nilssen, S. M. Muyeen, A. Nysveen, and A. Al-Durra, "Ironless multi-stage permanent magnet generators for offshore wind turbines." Submitted to *Energy Procedia*. Chapter 5.

Conference papers:

- Z. Zhang, A. Matveev, S. Øvrebø, R. Nilssen and A. Nysveen, "State of the art in generator technology for offshore wind energy conversion systems," *IEMDC2011*, Canada, pp. 1131-1136. Chapter 3.

- Z. Zhang, A. Matveev, S. Øvrebø, R. Nilssen, and A. Nysveen, "Review of modeling methods in electromagnetic and thermal design of permanent magnet generators for wind turbines," *ICCEP2011*, Italy, pp. 377-382. Chapter 1.

- Z. Zhang, A. Matveev, R. Nilssen, A. Nysveen, "Large-diameter ironless permanent magnet generator for offshore wind power application," *ICEM2012*, France, pp. 684-690.

- Z. Zhang, M. Molinas, A. Matveev, R. Nilssen, and A. Nysveen, "Efficiency Calculation and Improvement of a Large-diameter Ironless Permanent Magnet Generator," *ICEMS2012*, Japan, pp. 1-6. Chapter 7.

- Z. Zhang, A. Matveev, R. Nilssen and A. Nysveen, "Ironless multi-stage axial-flux permanent magnet generator for offshore wind power application," *12th Joint MMM/Intermag Conf.*, USA, 2013. Chapter 5.

Poster and oral presentations at conferences:

- A. Matveev, Z. Zhang, S. Øvrebø, R. Nilssen and A. Nysveen, "Novel PM generators for large wind turbines," *EPE WECS & T&D Seminar*, Norway, 2011.

- A. Matveev, Z. Zhang, S. Øvrebø, R. Nilssen and A. Nysveen, "Three special solutions for wind power converters," *VDI-Fachkonferenz Getriebelose Windenergieanlagen*, Germany, 2012.

Contents

Chapter 1

Introduction

As a solution of supplying electricity to areas far from the grid, harnessing wind energy started over 100 years ago. Modern wind energy technology was developed to deal with the energy crisis in 1970s and with more focus on climate change nowadays. Onshore wind energy application encounters issues from the land-use dispute, noise and visual pollution, to engineering challenges, such as transportation of machines with large dimensions. Vast areas are available offshore. The wind at sea is stronger and more stable than onshore wind. Offshore wind farms have less interference with residential areas in terms of noise and visual pollution than those onshore. Marine ecosystems and aquaculture may benefit from substructures of offshore wind turbines [1]. Therefore, offshore seems to be an ideal place for large scale wind energy exploitation.

There are several significant features in offshore wind energy application. Firstly, the design of wind energy conversion system (WECS) should take into account the harsh environment: humidity and salted air, which may damage the sensitive components, such as generator windings. Secondly, WECS with high rating per unit is preferred, because offshore wind is strong, and there are less constraints than that on land to transport large machines, if the logistics are properly arranged. Thirdly, the reliability is essential for the offshore wind business, because offshore maintenance is difficult, expensive and weather-dependent. Fourthly, compact and lightweight design is desired, given the difficulty of handling heavy equipment offshore. Last but not least, the cost of the whole WECS should be well controlled. The generator is one of the key components in a WECS. Different drive trains demand corresponding generators, and the cost, efficiency, and reliability of the whole system will be affected accordingly. Therefore, the generator designer will have to bear the aforementioned points in mind.

One of the promising generator concepts for offshore wind turbines is the direct-driven ironless permanent magnet generator (iPMG). This technology was first proposed for high-power wind turbine publicly in 2005 with [2], which demonstrated a one-rotor-one-stator (1R-1S) radial-flux (RF) iPMG with spokes structures for multi-MW offshore wind

12

turbines. The stator coil is encapsulated and supported by non-magnetic material (Figure 1.1a). Because of no iron in stator, the rotor exerts no magnetic force to the stator, and a lightweight structure was claimed to be possible to achieve. An 11.1 kW prototype was built to demonstrate this concept.
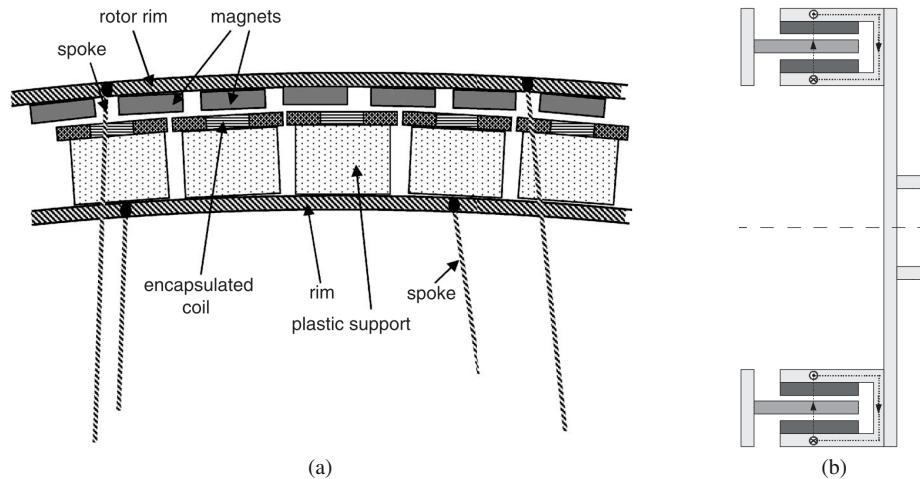
Figure 1.1: Ironless RFPMG: (a) 1R-1S [2]; (b) 2R-1S [4].

In 2007, using an analytical mechanical design method, [3] compared the mass of iron-cored PMGs and two-rotor-one-stator (2R-1S) axial-flux (AF) iPMGs with power up to 5 MW, and concluded that *at higher torque ratings, the structural mass is a greater proportion of the total machine mass*. iPMG was reported to be larger, lighter, and more expensive than iron-cored PMG. The RF version of this 2R-1S iPMG was further developed in [4] to a C-core machine (Figure 1.1b), which was described to be lightweight and simple to assemble. It showed that the normal stress could be 10 times the shear stress in an iron-cored PMG. A comparison to a commercial 100 kW iron-cored PMG, showed that the proposed concept could save 55% of the total machine mass. A 20 kW prototype was built for demonstrating the manufacturing advantages.

In 2009, [5] investigated multi-stage (MS) ironless AFPMG at 5-7 MW with the layouts in Figure 1.2. This machine was emphasized to have no cogging torque and no stator iron loss. The discussion concluded that the layout in Figure 1.2a is smaller, lighter, and cheaper than the one in Figure 1.2b, but it is more difficult to assemble the magnets inside its stacks.

Previous research have mainly demonstrated the iPMG concept. There has been no systematic investigation on the design of iPMG and other possible layouts. These untouched topics form the main frame of the whole thesis. This chapter presents an overview of the thesis, including the objectives, technological state of the art on the research of ironless permanent magnet machine (iPMM), main contributions, and research scope.
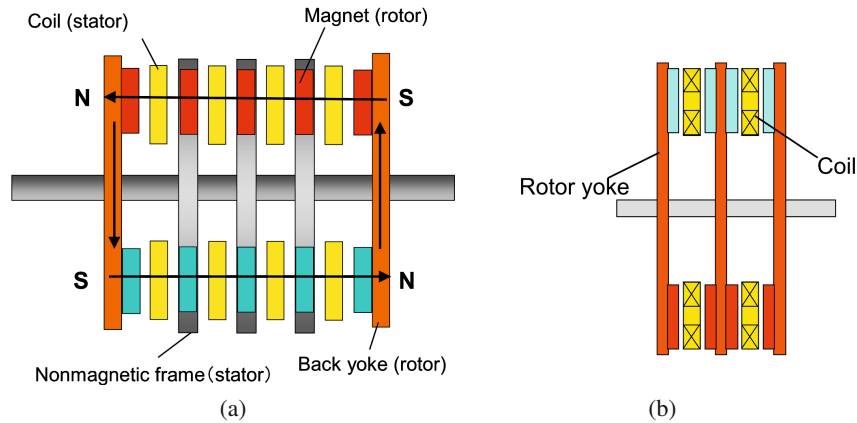
Figure 1.2: Multi-stage ironless AFPMG [5]: (a) without inter-stage rotor yoke; (b) with inter-stage rotor yoke.

1.1 Objectives

The general objective of this thesis is to investigate the design, modelling, and optimization of iPMG together with the state of the art modelling approaches. To be specific, the following concerns are to be investigated:

- What is the state of the art on generator technologies for offshore wind power application? Which generator concept is the dominant one? and why? Are there any emerging technologies? and what are the strengths and drawbacks of these new concepts?

- The technology of low-power iron-cored PMGs for onshore application is becoming mature, should iron-cored PMGs be among the recommended solutions for future high-power offshore WECS? What are the main challenges?

- iPMG has been reported to be promising for achieving a lightweight wind turbine, among different types of iPMGs, which type is recommended? What are the design features?

- Analytical approach is widely used in machine preliminary design and optimization, what are the advantages and challenges for using finite element method (FEM) instead? How well can machine designers take advantage of commercial codes to address challenging problems, such as 3D problems, multiphysics problems, and machine optimization? Are open source codes capable of these tasks? What is the frontier of machine simulation techniques?

- Ordinary PCs and workstations are normally used in machine design and optimization, should the machine designers demand more, or even consider the high per-

formance computing and super computers? How to take advantage of large-scale computing resources (LCR)?

- It has been investigated to use serial compensation and d-q theory for compensating the current harmonics in the variable-speed iron-cored PMGs. Instantaneous ABC theory is never tried, what is effect of using this theory to improve the efficiency of iPMG?

1.2 State of the art iPMM technology

Most of the electrical machines, from the spindle motors for washing machines to huge hydro generators, have to use steel. This is not just for having a solid structure, actually, the supporting structures of electrical machines do not need to be made of steel [6]. The function of steel is to collect and route the magnetic flux in the machine stator and rotor (active parts). This capability relies on the high permeability of iron that the steel contains. A pure iron can have a relative permeability up to 200,000. By adding some other elements (silicon etc.), the mechanical properties of electrical steel for electrical machines are largely improved, while the relative permeability can still maintain several thousand. In addition, iron is ranked the fourth most abundant element in the earth's crust, after oxygen, silicon, and aluminium, which all have the relative permeability merely around one.

Electrical steel is normally used in rotor, stator teeth, and stator yoke. In this thesis, *iron-cored machine* is used to refer to the machine that has electrical steel in these three parts. Any machine that does not have steel in one of the three parts, is referred as *ironless machine*.

iPMM is a well-known technology. The relevant patents date back to at least 1969 [7]. A series of publications on iPMM came in late 1990s and early 2000s, and numerous patents were published in 2000s, e.g. [8]. As shown in Table 1.1, iPMM is normally used in low-power high-speed applications. The research on high-power low-speed iPMMs, such as generators for multi-MW wind turbine, is mainly on the level of concept demonstration. Before the start of this thesis, there was no work focusing the systematic investigation of iPMM technology.

Table 1.1: List of iPMM applications.

No.	Power(kW)	Speed (rpm)	Topologies	Types	Applications	References
1	0.00623	10,000	2R-1S-AF	prototype	computer hard disk drive	[9]
2	0.23	450	2R-1S-AF	prototype	micro wind turbine	[10]
3	0.39	3,000	2R-1S-AF	prototype	cost-sensitive application	[11]
4	1	300	2R-1S-AF	commercial product	vehicle wheel motor	[12]
5	1	20,000	2R-1S-AF	prototype	portable power source	[13]
6	1.8	1,060	2R-1S-AF	used in application	vehicle wheel motor	[14]
7	2	500	2R-1S-AF	prototype	small wind turbine	[15]
8	2	6,000	2R-1S-AF	prototype	automobile	[16]
9	2.25	1,000	MS-AF	concept	unmanned aircraft propulsion	[17]
10	4	1,380	2R-1S-AF	prototype	multiple applications	[18]
11	4.2	300	2R-1S-RF	down-scale prototype	targeting small wind turbine	[19]
12	6.2	6,000	2R-1S-AF	commercial product	servo control	[12]
13	11.1	150	1R-1S-RF	down-scale prototype	targeting multi-MW wind turbine	[2]
14	20	100	2R-1S-RF	down-scale prototype	targeting MW wind turbine	[4]
15	25	1,100	MS-AF	prototype	wheel motor for city car	[20]
16	25	100	MS-AF	down-scale prototype	targeting multi-MW wind turbine	[21]
17	45	50,000	MS-AF	concept	high-speed generator	[22]
18	72	3,000	2R-1S-AF	prototype	multiple applications	[23]
19	154	1,950	2R-1S-AF	prototype	internal combustion engines	[24]
20	6,500	13	MS-AF	concept	MW wind turbine	[5]

Even though they are not as popular as iron-cored machines, iPMMs have several obvious advantages that make iPMMs attractive in some specific applications.

- High efficiency and low cost for high-speed application. If there is no iron used in the stator teeth and yoke, the stator iron loss is eliminated. Iron loss depends on the machine operating frequency, and grows faster than frequency (eddy current loss is the dominant loss at high frequency, and its magnitude is proportional to the square of the frequency). Therefore, high efficiency can be expected from iPMMs operating at high speed. In addition, high-speed iPMG is compact and lightweight, and the simplicity of manufacture and assembly can further bring down the cost. This is attractive for the applications like home appliance [11], portable power source [13], special vehicle [14], special aircraft [17], and other high efficiency applications [18], [22]-[24].

- No cogging torque. Cogging torque is caused by the magnetic reluctance variation in the air gap. If a machine has significant cogging torque, the machine will be difficult to start, and torque ripples will be produced, which can further lead to problems like noise and low efficiency. iPMM does not have the cogging torque, which is important for applications like small wind turbines [15], [19].

- No normal stress. When there is iron in the stator yoke and teeth, the normal (attraction) stress exists between rotor and stator. This stress requires a rigid supporting structure to maintain structural balance. iPMM eliminates this stress and the corresponding adverse effect in the system like hard disc drive [9].

- Compactness and mechanical flexibility. Without iron in the stator, iPMM is simple to construct, this meets the need of small-scale wind turbines [10], [15]. Some iPMMs, such as the AF machines, are flexible to be integrated to system structures like vehicle wheels [12], [14], [20], which can further reduce the weight and cost of the whole system.

- Low total weight. The negligible normal stress in iPMM does not demand a heavy supporting structures, this is important for applications where lightweight is of concern, e.g. high-power wind turbines [2], [4], [5], [21].

Because of the ironless structure, iPMMs have the following disadvantages:

- High consumption of PM material. An ironless machine requires more excitation source to overcome the low permeability flux path. In the case of iPMM, this excitation comes from permanent magnet material. In high performance iPMMs, one of the most used permanent magnet materials is neodymium magnet, which is brilliant for its strong magnetic properties, and widely used in high-precision applications, such as video devices, medical instruments, and military weapons. However, mining rare earth contaminates soil and water. Amid the increasing global demand, a tougher regulation from the perspective of environmental protection can easily

17

boost up the price of rare earth. Therefore, iPMM may be not a cost-effective so-
lution if its cost can not be brought down by increasing the operational speed or
integration design.

- Low inductance. iPMM has low inductance, which prevents it from being used in
the application where flux weakening is required, such as automobile [16].

1.2.1 Topologies

Different names are used to describe iPMM or its parts, e.g. ironless [2], [25], air-cored
[4], [19], [26], and coreless [27]. In open publication, the use of the above terminologies
is not in a clear way. Different names may be given to one machine topology, or one name
may refer to different machine topologies.

In this thesis, the classification of iPMMs is based on whether or not iron is used in
one of three parts: stator teeth, stator yoke, and rotor. This method tries to include all the
topology variants under one name **iPMM**. Following this method, iPMMs are classified
into three types:

Machines without iron in stator yoke and teeth

Most iPMMs in open publications are of this type, which have iron in neither stator teeth
nor yoke. This topology is normally presented as a 2R-1S structure (Figure 1.3 and 1.1b).
The machine pole consists of PMs in a conventional array. Both AFPMGs and RFPMGs
have been used. The AF version that has PMs on both rotors, as shown in Figure 1.3(a), is
also referred as ironless Torus [28], [29]. In some applications, it is sufficient to have PM
on one rotor, and there is only rotor yoke on the other rotor. Then this topology becomes
like that shown in Figure 1.3(b).

Though not common, it is possible to design an iPMM with 1R-1S structure (Figure
1.1a). Because there is only one rotor, there will be no rotor-to-rotor force. The supporting
structure can be further reduced.

Machines without iron in stator and rotor

The machine pole of this type is normally made of PMs in the so-called Halbach array,
and no iron is used in stator teeth, stator yoke, and rotor. By completely eliminating iron
in the machine active parts, this topology is used in the applications where high-power-
density high-efficiency machine is expected, such as servo control [12] and solar-powered
vehicle [14].
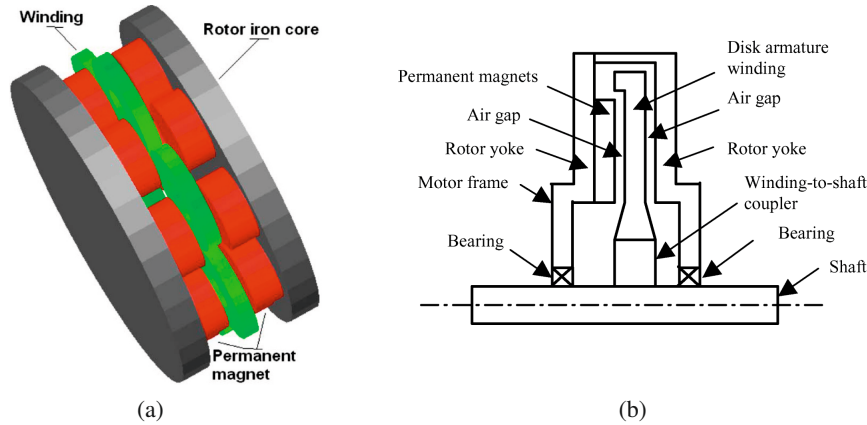
Figure 1.3: 2R-1S-AFPM machines [10], [30]: (a) PMs on both rotors; (b) PMs only on one rotor.

Other types

There are some other machines that do not have iron in part of the active parts. These machines are normally known under other names, such as

- Halbach machine. This machine has conventional AC stator and the rotor pole in Halbach array, as shown in Figure 1.4(a).

- Yokeless machine (no stator yoke), shown in Figure 1.4(b).

- Slotless machine (no stator teeth), shown in Figure 1.4(c).

An ironless AFPM machine has a disk-like shape, which makes it flexible to be integrated to the system structure. Therefore, ironless AFPM machine gains more popularity than the ironless RFPM machine in the applications like vehicle wheel motor and wind turbine. The outer diameter of ironless AFPM machines is often constrained in practical engineering. To produce more torque, MS solutions may be used, as shown in Figure 1.2b. Each stage of such a machine consists of a topology depicted in Figure 1.3 or the AF version of Figure 1.1a.

1.2.2 Modelling methods

Direct-driven iPMM is normally designed with a large diameter. The machine torque is roughly proportional to the machine volume. Therefore, a large-diameter iPMM will have short length along the axial direction, i.e., have the ring shape, which means the

(a)

(b)

(c)
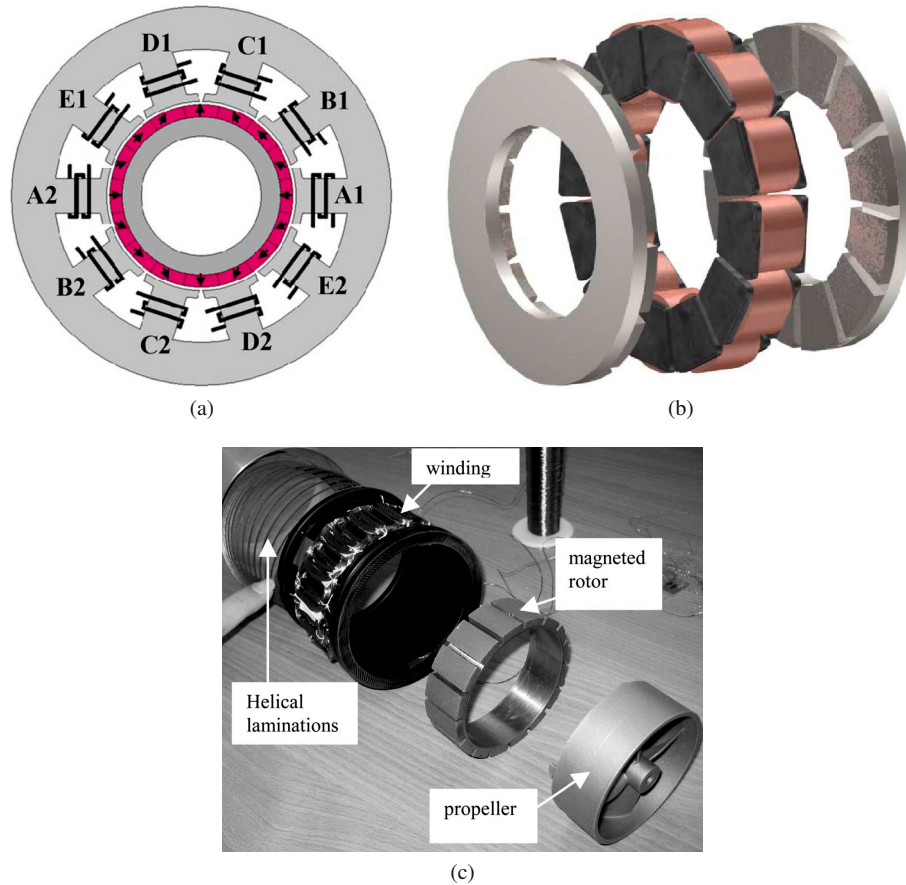
Figure 1.4: Other iPMM topologies: (a) Halbach machine [31]; (b)yokeless machine [32]; (c) slotless machine [33].

strong 3D feature of the magnetic and thermal field. In industry, large-diameter machines are normally integrated to the wind turbines (Figure 1.5). Under this integration design, the machine electromagnetic and thermal design will be affected by the structural design. These design features of iPMMs should be dealt with proper and capable design tools.

Various methods have been developed for the design of electrical machines. These methods are important references for the electromagnetic and thermal design of generators for offshore wind turbines.

20
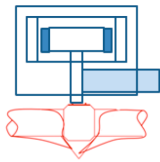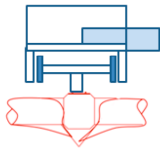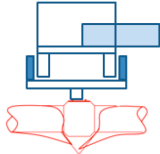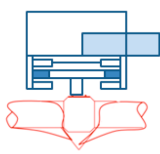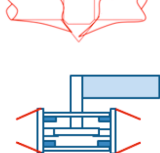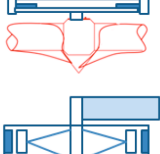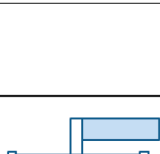
	Behind tower	Between blades&tower				No nacelle	
	Radial flux with iron cores			Axial-flux with iron cores		Ironless (air core)	
	Inner rotor, "stand-alone"	Integrated machine		"stand-alone"	Integrated with blades	1 rotor, 1 stator	2 rotors, 1 stator
		Inner rotor	Outer rotor				
Companies →	GE, TheSwitch	Leitner, Vensys, Harakosan	TheSwitch, Siemens	Jeumont		NGenTech	
Cooling → **Stator**							
Liquid cooling	x	x	x	x	x	x	x
Slits for air flow & air pumped through	x						
Heat to carrying structure then to the wind	x	x				x	x
External air flow		x				x	
Rotor							
Internal air circulation	x	x		x	x		
External air flow	x	x	x	x	x	x	x

Figure 1.5: Different concepts of integration design [34].

21

Analytical methods

Three analytical methods in literature are used for the machine electromagnetic design, namely the equivalent magnetic circuit method, the magnetic potential method, and the permeance network method. In the equivalent magnetic circuit method, the air gap field is solved by applying Ampere's law in a closed flux path, in which the MMF drop, MMF source and reluctance are derived. Axial length may be compensated to take into account 3D effect. This method is normally used for rough estimations. Design procedures of certain type machines can be found in many textbooks, such as [35]. In the magnetic potential method, the magnetic field is calculated by directly solving Maxwell equations with scalar or vector magnetic potential. The choice of the magnetic potential depends on the coordinate system used, and how to treat the magnetization vector of PM and armature current sheets [36], [37]. By assuming infinite permeability in the core, no load field and armature reaction field are computed separately, and the resultant field is obtained with the superposition method. The challenge is to properly take into account the coil shape, slot effects, pole shape, and 3D geometry [38], [39]. The permeance network method has the same theory root as the magnetic equivalent circuit method, and also share a similar feature with numerical methods in forming elements and solving matrices. The key point of the permeance network method is to reasonably predict the flux paths and use proper permeance elements in each path (Figure 1.6). An explicit application of the permeance network method has the following features:

- Take into account iron saturation with iterations or a saturation factor.

- Versatile to capture leakage flux.

- Capable of handling motion by using high density permeance elements in the air gap [40].

The permeance network method can be regarded as a compromise between the analytical method and the numerical method in terms of accuracy and calculation time.

Similar to the permeance network method for magnetic field calculation, the lumped parameter network method is used for the thermal field calculation. A typical lumped parameter network consists of thermal resistances, thermal capacitances, and power losses. This method can be used to handle heat transfer of conduction, radiation, convection, and steady or time-dependent problems. Accurate thermal lumped parameter network is dependent on model complexity and heat transfer coefficients, which are affected by material property, cooling path, manufacturing process, and also smoothness [41].
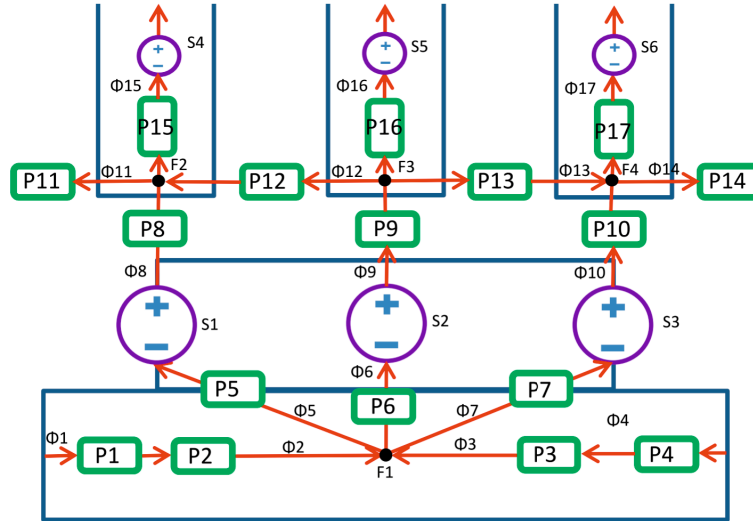
Figure 1.6: The permeance network of an iron-cored 2R-1S-AFPMG (half of a pole pair).

Numerical methods

For machine electromagnetic design, two numerical methods are normally used: boundary element method (BEM) and finite element method (FEM). BEM has not seen significant development in the last decade [42]-[44]. [43] investigated the use of BEM to handle 2D magneto static and 3D eddy current problems, and concluded that using BEM to solve 3D eddy current problem leads to inaccurate result. Comparisons of boundary-based and domain-based methods concludes that BEM is not ideal for machine design but can be the complement to domain-based method. [44] reviews the development of fast BEM solver codes, and presents a time-harmonic 3D vector BEM model which is expected to couple with fast solver codes and enable efficient machine design in the future. The commercial software company, Integrated Engineering Software Inc., uses BEM and Hybrid method in its solvers, and claims some advantages, such as more accurate results obtained when handling open boundary problems [45]. Compared to BEM, FEM is widely used in modern electrical machine design for its high accuracy and fast speed in solving symmetrical and sparse matrices [46]. Most of the commercial software use FEM in their solvers [47]. A typical special-purpose FEM software is capable of handling 2D/3D transient problems and taking motion into account. The trend of FEM includes developing fast solvers, shared memory processing, and distributed memory processing [48].

In conventional electrical machine design, thermal FEM is normally neglected due to the use of thermal analytical method or the designers experience on similar machines. High power PMGs and new machine topologies have pushed the need of thermal FEM, such as in [49], and highly commercialized FEM software now can supply a thermal FEM module in their machine design package, such as JMAG, ANSYS, MagNet, etc.

The difficulty of thermal analysis is to ensure the accuracy of heat transfer coefficients, normally CFD is required. The benefits of using CFD are [41], [50], [51]

- Investigate the influence of geometry variation on heat transfer.

- Obtain the local heat transfer coefficient and local mass flow rate.

Software

A well-established software is normally the first choice for fundamental analysis of electrical machines, though some machine designers make software themselves. According to the different level of commercialization, the software can be categorized into open source/free software, commercialized software, and highly commercialized software. A comparison of these three types is given in Table 1.2.

The development of commercial machine design tools shows the following trends.

- Rich interface with external environments: circuit simulator, optimization tools, scripting.

- Multiphysics, multidomain.

- Accurate and fast solver.

- High performance computing: shared memory processing (SMP) and distributed memory processing (DMP).

Table 1.2: Comparison of software.

Types	Advantages	Disadvantages	Examples
Open source / free software	Small program, use small RAM; fast, low/no cost; flexible to be driven by external environment.	Limited to a small group of users and specified types of motors; may be limited to certain operating system; limited capability.	Emant, FAT, FEMM, GetDP, iMOOSE, MagSolve, pdnmesh, Poisson Superfish, RillFEM, FEMG, IES.
Commercialized software	Small program, low-cost.	Relatively slow version-updating, insufficient tutorial; limited functionality.	EMSolution, FEHT, FlexPDE, QuickField, ElectorMagneticWorks, MagneForce, MEGA, Permas, PC-FEA.
Highly commercialized software	Fast version-updating, rich in supporting documentation and service; rich functionality.	Require advanced hardware to support; expensive.	Flux, ANSYS, Magnet, Opera, COMSOL, JMAG, Fluent, SPEED, MotorCAD.

1.3 Main contributions

Compared to other publications, this thesis has following contributions:

- Technology state of the art: there is no overview on the generator technologies for offshore wind turbines. This thesis presents a statistic analysis of wind turbines in all the global operational offshore wind farms. Generator technologies used in these wind turbines are reviewed and discussed. In addition, the efficiencies of different drive trains are modelled and compared. New technologies and concepts for offshore wind power application are also investigated. Therefore, the review work presented in this work is deep, comprehensive, and the first of this kind.

- Iron-cored PMGs: previous studies investigated the weight of iron-cored PMGs by mechanical design. This thesis presents another approach to understand the topic. The generator total weight is obtained with a tool developed to demonstrate the technology frontier of electrical machine design. The generator active weight is obtained in machine optimization with 2D FEM. Finally, the generator inactive weight is found by subtracting active weight from the total weight. This method is new and the derived conclusion explains the reason to develop iPMGs from a different perspective.

- iPMGs: iPMG is not a new concept, however it is mainly used in low-power (several kW) high-speed (several thousand rpm) applications. Open publications on applying low-speed (< 20 rpm) iPMGs at MW and Multi-MW level have only focused on conceptual demonstration. This thesis presents a systematic investigation on the concepts, design method, optimization and comparison of Multi-MW iPMG. The presented design considerations, the proposed design method, and optimization and comparison results are all new in this field.

- Modelling: it is not new to use FEM for the machine design and optimization, and it is also not rare to apply FEM directly in the preliminary design of electrical machines. However, it is though bold to discard analytical methods and advocate the use of numerical method in an unprecedented scale. The machine models presented cover from 1D, 2D, to 3D, from single physics to multiphysics, from PC-based to an attempt of using super computer. The calculation codes include open source codes and latest commercial codes. The practical challenges of applying FEM in machine design and optimization are detailed, and the corresponding solutions are proposed and implemented. Exploiting the FEM to its frontier, as presented in this thesis, is a topic that has never been addressed in such a serious manner.

- iPMG efficiency improvement: serial compensation and classical d-q theory have been tried by others to mitigate the current harmonics of PMGs controlled by the converter with diode rectifier, whereas in this thesis, the investigation focuses on the low reactance of iPMG and the use of active shunt filter under the control of instantaneous ABC theory. The presented calculation method and derived conclusion fill the blank of this research area.

1.4 Scope

In a single thesis, it is not possible to solve every technical aspects related to generators for offshore wind turbines. The research scope of this thesis is given below:

- Direct-driven variable-speed PMGs for horizontal-axis non-floating wind turbines.

- The non-conventional iPMG concepts, depicted in Figure 1.4, are not included.

- Generator power from 6 MW to 10 MW.

- Direct air cooling.

- Magnetic and thermal field analyses. Structural design is not included.

1.5 Outline of the thesis

In this thesis, each chapter corresponds to a paper. Besides the elimination of unnecessary overlapping, some modelling details are supplied additionally to make it more understandable. Major changes (compared to publications) are mentioned in the corresponding chapters.

The outline of this thesis is as below.

Chapter 2 presents an overview of the generator technologies for the offshore wind turbines. Statistical analysis is conducted on all the global operational wind turbines. Different drive trains are evaluated by modelling and comparing their efficiencies. Finally, new generator technologies are reviewed and discussed.

Chapter 3 investigates the weight variation of iron-cored high-power PMG. The generator total weight is obtained by the investigation of over 90 industrial products and academic designs. The generator active weight is calculated from machine design and optimization. Finally, the variation of the iron-cored PMG weight as the power grows is obtained.

Chapter 4 presents a systematic investigation of the iPMG concepts and a comparison of 10 MW iron-cored PMG and iPMG. First, the practical aspects on design and application of iPMG technology is discussed, then a design and optimization approach is developed. This approach is used to design and compare eight different types of iPMGs. Afterwards, optimal machines in terms of torque density and efficiency are obtained. Finally, 10 MW iron-cored PMG and iPMG are compared with respect to inactive/total weight/cost.

Chapter 5 presents the investigation on the design of MS-AFPMGs. First, the design approach developed in Chapter 4 is further improved to shorten the calculation time. The upgraded design approach is used to investigate the optimal MS-AFPMGs in terms of torque density, efficiency and multiple objectives.

Chapter 6 focuses on the machine optimization with large-scale computing sources. A design strategy is developed to enable this possibility. 3D multiphysics approach, including both electromagnetic and thermal analyses, is presented and all the calculations are done with open source codes. A design example is given to demonstrate the details and feasibility of this approach. The practical challenges of optimizing electrical machines with supercomputers are discussed.

Chapter 7 presents an investigation on the machine efficiency improvement with the help of compensation technique borrowed from power system theory. The ABC compensation theory is used to minimize the current harmonics in a wind energy conversion system where a diode rectifier is used.

Chapter 8 concludes the thesis and highlights the findings. The future works are discussed.

Chapter 2

Generators for Offshore Wind Turbines

In this chapter, the state of the art generator technology is reviewed. Section 2.1 presents an overview of the global offshore wind turbines; the generators used in global operational offshore wind farms are reviewed in Section 2.2; Section 2.3 makes an efficiency comparison of various drive trains; new generator technologies and concepts are reviewed in Section 2.4.

2.1 Overview of offshore wind turbines

Based on the numerous public resources, a statistical analysis of the global offshore wind farms is conducted to get a whole picture of the technologies. It is found that 1886 wind turbines were installed in 57 offshore wind farms globally by the end of 2012, and the total operational capacity was 5.45 GW. According to the installed capacity and the turbine average rating, the development of offshore wind power can be divided into three stages. In the first stage (1991-1999), the total installed capacity was 31.7 MW, and the average turbine rating was no more than 600 kW. During 2000-2010, offshore wind power industry experienced fast development; the geared solution, pitch-regulated variable speed energy conversion system with induction generators, became mature, and got widely adopted in offshore wind turbines. During 2011-2012, the turbine average rating was increased to 3.87 MW, which was a big step from previous 2.56 MW for 2000-2010 [52], [53].

This section presents this statistical investigation from three aspects: turbine average rating, drive train technology, and generator type.

2.1.1 Average rating

Figure 2.1(a) clearly shows the three-stage development of the offshore wind power industry, and fast development was seen from the first decade of this century. This is in accordance with the increasing awareness of the climate change, the need for diversifying the power supply, and the technology advance. It is also natural to expect more development as 5 MW (and above) turbines are now becoming popular in European offshore wind farms.
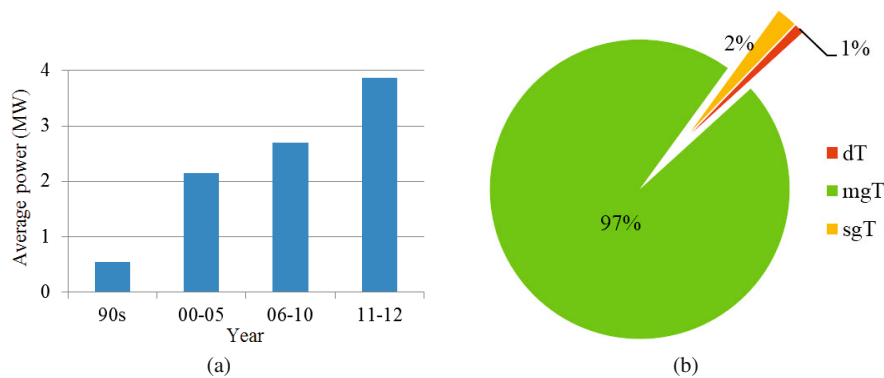
Figure 2.1: (a) Development of turbine average rating; (b) Market share of drive trains in term of installed capacity (ddT: direct-driven drive Train; mgT: multi-stage geared drive Train; sgT: single-stage geared drive Train).

2.1.2 Drive trains

Three drive trains are employed in the offshore wind farms: multi-stage geared drive Train (mgT), single-stage geared drive Train (sgT), and direct-driven drive Train (ddT). As shown in Figure 2.1(b), mgT is the dominant drive train. This is because at the power level of 3 MW and below, mgT is a mature technology, and there are well-developed products in the market. Therefore offshore wind industry can directly benefit from these expertises. However, as the turbine rating goes high, the need for high performance and high reliability turbines has pushed new technologies to emerge, such as sgT and ddT.

2.1.3 Generators

Totally five types of generators are used in offshore wind farms, and they are: Doubly-Fed induction Generator (DFG), Squirrel-Cage induction Generator (SCG), Wound-Rotor in-

duction Generator (WRG), Permanent Magnet synchronous Generator (PMG), and Electrically-Excited synchronous Generator (EEG). As shown in Figure 2.2(a), the dominant generators are DFG and SCG. This dominance can be explained with the maturity of the technologies. High speed induction machine around 3 MW is widely available in commercial market, whereas PMG is relatively new. EEG is not a new technology; however, it has a complicated rotor construction and low efficiency. WRG does not support full variable speed operation.

Figure 2.2(b) shows the average power of each machine type for the period 2008-2012. SCG has higher rating than DFG and PMG. This is due to the popular Siemens turbine SWT 3.6-107 (SCG). PMG has the lowest average power, though slightly above 3 MW.
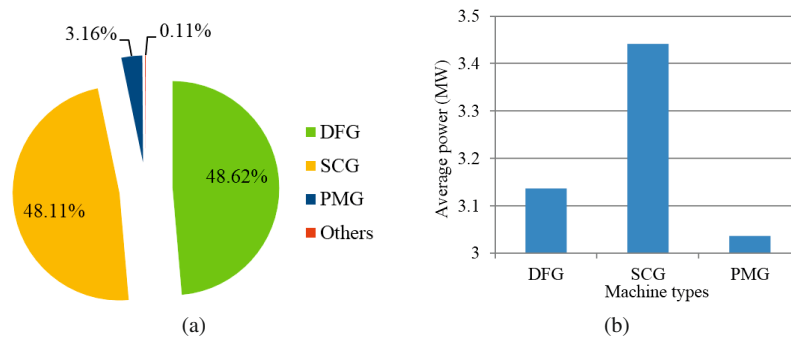
Figure 2.2: (a) Market share of different machine types (DFG: Doubly-Fed induction Generator; SCG: Squirrel-Cage induction Generator; PMG: Permanent Magnet synchronous Generator); (b) Average power vs. machine types for 2008-2012.

2.2 Generators in operational offshore wind turbines

Two types of WECS are now being used in operational offshore wind farms: fixed-speed WECS and variable-speed WECS. During wind fluctuation, the grid-connected generator for fixed-speed WECS cannot vary its speed very much to damp the fluctuating power, and is therefore subject to mechanical stress. High flicker may appear in the generated power. For variable-speed WECS, the generator speed can be controlled by converter, then the fluctuating power can be stored in the turbine rotor, and a smooth output can be obtained. The converter output voltage has harmonics and high voltage components which require special concern in the design of generator insulation, cooling, and bearing. Fixed-speed WECS uses induction machines because of the simple structure and low cost, but for variable-speed WECS, both induction generators and synchronous generators have been used.

2.2.1 Induction generators

Fixed-speed squirrel cage induction generator

SCG was used in fixed-speed WECS (Figure 2.3a) in offshore wind farms before 2004. The wind turbine speed is held constant with stall/pitch/active stall control [54]. The driving force is transferred to SCG via a multi-stage gear box, it is therefore operated at high speed. The stator is directly connected to the grid. A soft starter is used to limit the inrush and voltage drop during grid connection [55], [56]. The SCG is also named self-excited induction generator, because the required reactive power is supplied from the grid or capacitor banks. The speed range of SCG is within 100% to 105% of the synchronous speed [57], and dependent on the generator parameters and capacitance.

The speed of SCG is not controllable, thus the mechanical constructure should be stiff enough to resist the high mechanical stress during wind gusts. A way to change the operational speed is to use pole-changing SCG [56]. A pole-changing SCG has two sets of stator windings (e.g. 4/6 poles) with which the machine can be operated at two different speeds. In such a way, the total energy yield can be increased.

SCG has the advantages of small dimensions, light weight, rugged construction, low price, low operation and maintenance cost, and no need of synchronizing circuit for grid connection. The disadvantage is low aerodynamic efficiency because of limited speed variation. Wind fluctuation may cause mechanical stress in the generator shaft and high flicker in the output power. Fixed-speed SCG is not capable of supporting the grid during fault.

Variable-speed squirrel cage induction generator

In this system (Figure 2.3b), a full-scale converter is used for generator speed control and grid-side power control. The generator has a wide speed range so that high aerodynamic efficiency is traced for capturing maximal power. The converter can regulate the reactive power required, control the voltage and frequency, so it is capable of meeting grid code.

The advantages of variable-speed SCG are simple construction, no slip rings, low cost, and high reliability, therefore the maintenance is easy and cost-efficient. The disadvantage is its relative low efficiency at light load. SCG is not used for direct-driven system because of low efficiency and low power factor in case of large numbers of poles [58].
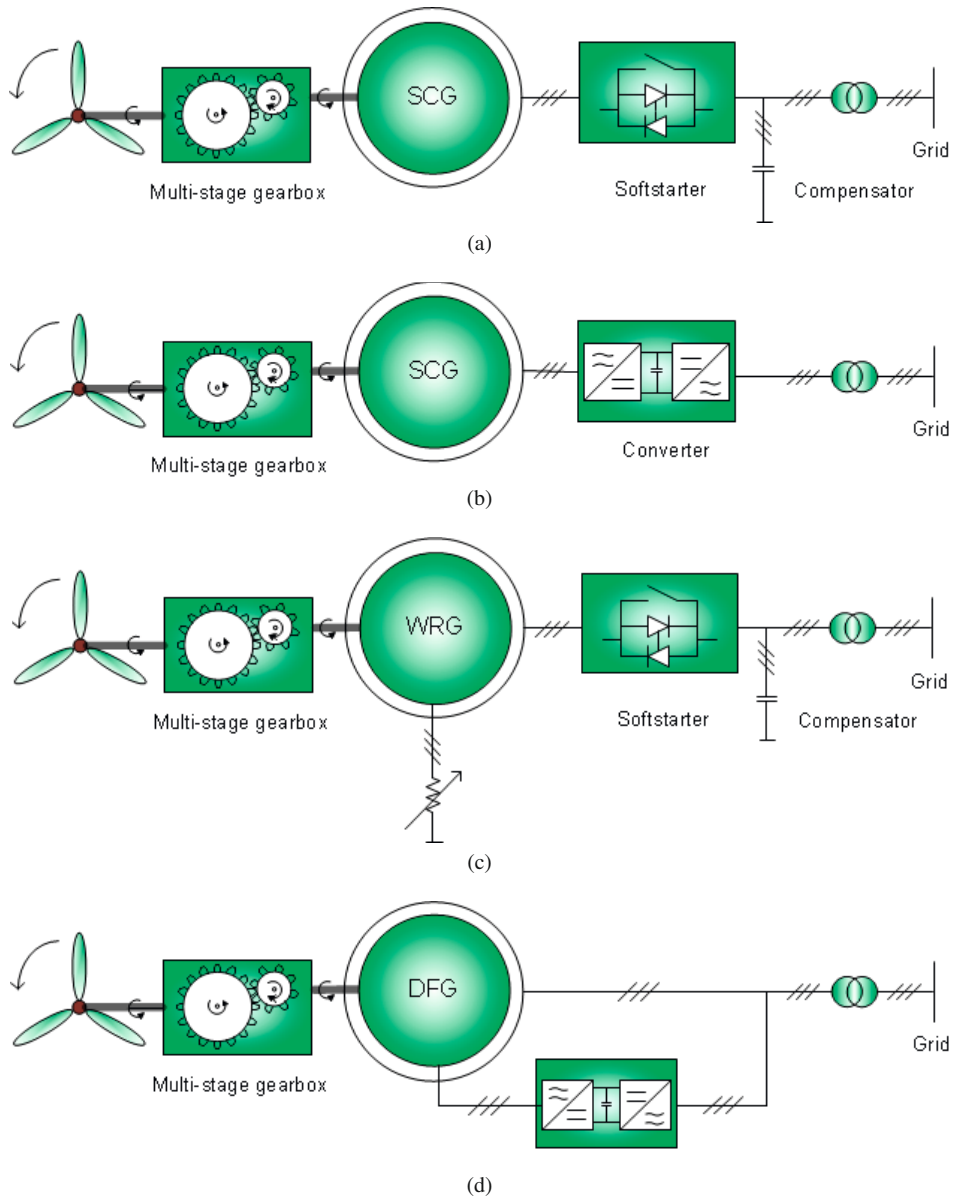
Figure 2.3: Wind energy conversion systems with induction generators: (a) SCG in fixed-speed WECS; (b) SCG in variable-speed WECS; (c) WRG in semi-variable speed WECS; (d) DFG in variable-speed WECS.

Semi-variable wound rotor induction generator

WRG has the rotor winding connected to an external resistor via slip rings for variable slip control (Figure 2.3c). The slip rings can be eliminated by installing resistors and control circuits into the rotor, and then optical control signals are sent to the rotating circuits [56]. By controlling the rotor resistance, the slip varies as wind speed changes. WRG has a little wider speed range than fixed-speed SCG; normally 110% [59] of synchronous speed operation can be achieved. Thus the WECS with WRG is named semi-variable system. WRG share the same system configuration as fixed-speed SCG: multi-stage gearbox to step up speed, reactive power compensator to supply magnetizing power and soft starter to smooth grid connection. By varying speed, WRG has certain effect to damp the mechanical stress during wind gusts. The disadvantage of WRG is low efficiency because of the power loss in the external resistors.

Doubly fed induction generator

DFG is driven by the turbine rotor through a multi-stage gearbox, with which the gear ratio depends on the generator stator pole number (4 poles or 6 poles) and grid frequency (50 Hz or 60 Hz). The stator is directly connected to grid. The rotor is connected to a partial scale converter via slip rings (Figure 2.3d). The rotor power, P_R, can be expressed by

$$P_R = -sP_N, \tag{2.1}$$

where s is slip and P_N is the generator rated power. In sup-synchronous mode, the rotor speed is higher than synchronous speed, slip is negative, and both rotor and stator supply power to grid. In sub-synchronous mode, slip is positive, and the rotor absorbs power from grid. The range of slip is around $\pm 25\%$, so the power that the DFG rotor needs to handle is small, compared to the stator power, thereby a low-cost converter can be used.

With the modulation of rotor current frequency by converter, the operation speed range of the generator is extended. Variable speed operation can damp the mechanical stress caused by the wind gusts and reduce flicker, and generate more power than fixed-speed WECS. Reactive power control and smooth grid connection can also be achieved. DFG is lightweight and low cost, the WECS with DFG is capable of supporting grid during fault, thus many wind turbine suppliers have products based on DFG , and it is the most used generator type in offshore wind farms.

The disadvantage of DFG is the slip rings, which need regular maintenance for being reliable. Some studies have been conducted on the Brushless DFG (BDFG) [60]-[62], which eliminates the slip rings and brush. BDFG has two sets of stator windings and a special designed rotor to couple with stator fields. The two stator windings are connected to grid and converter respectively. BDFG is preferred for offshore wind application where reliability and cost-reduction are of special concern. However, the feature of complex

structure and complicated control scheme, especially low power density [62], puts BDFG still under research.

2.2.2 Synchronous generators

Electrically excited synchronous generator

EEG uses DC power to produce the excitation field in its salient rotor, and requires a full-scale converter for power and speed control. With the rotor excitation regulation, the reactive power and voltage control are achieved (Figure 2.4a). EEG can be used in geared WECS or direct-driven WECS. In offshore, only the solution with direct-driven EEG (dd-EEG) is used. For direct-driven application, high torque is required because of the low speed operation, which makes dd-EEG large and heavy [56].

The advantages of dd-EEG are the elimination of the unreliable gearbox and thus the simple drive train. dd-EEG has relatively low efficiency because of the excitation losses in rotor. Compared to geared solution and permanent magnet generator, large dimensions and heavy weight make it expensive and less attractive [55].

Direct-driven permanent magnet generator (dd-PMG)

By incorporating the permanent magnet material, a PM machine has the advantages of high power density, high efficiency, lightweight, and simple rotor structure. In the past two decades, the sharp decrease in PM material price stimulated the PM machine technology and its adoption in wind turbine. WECS with PM machine has high annual energy production, and it is regarded promising in the future offshore wind farms, but the high machine cost and unclear PM material price trend in the future may offset the development of PM machine in wind industry.

According to the different magnet field path, PM machines can be classified into three types: RF machine, AF machine, and transverse flux (TF) machine. A lot of research has been done to investigate and compare the characteristics of each type [63]-[68]. RFPMG has the simple structure and good performance, and it is the most used PMG. A significant feature of the AFPMG is its larger diameter and short length, which makes it suitable to be integrated with the wind turbine [69]. High power can be achieved just by putting multiple stages in the axial direction. The drawback is the difficulty to maintain the air gap and the structural stability. TFPMG has high power density and low copper losses, but complicated structure and high synchronous reactance, which makes the converter expensive. TFPMG has not been used in large-power wind application.

PM machines have been used (or proposed) in different drive trains: direct drive,

(a)

(b)

(c)
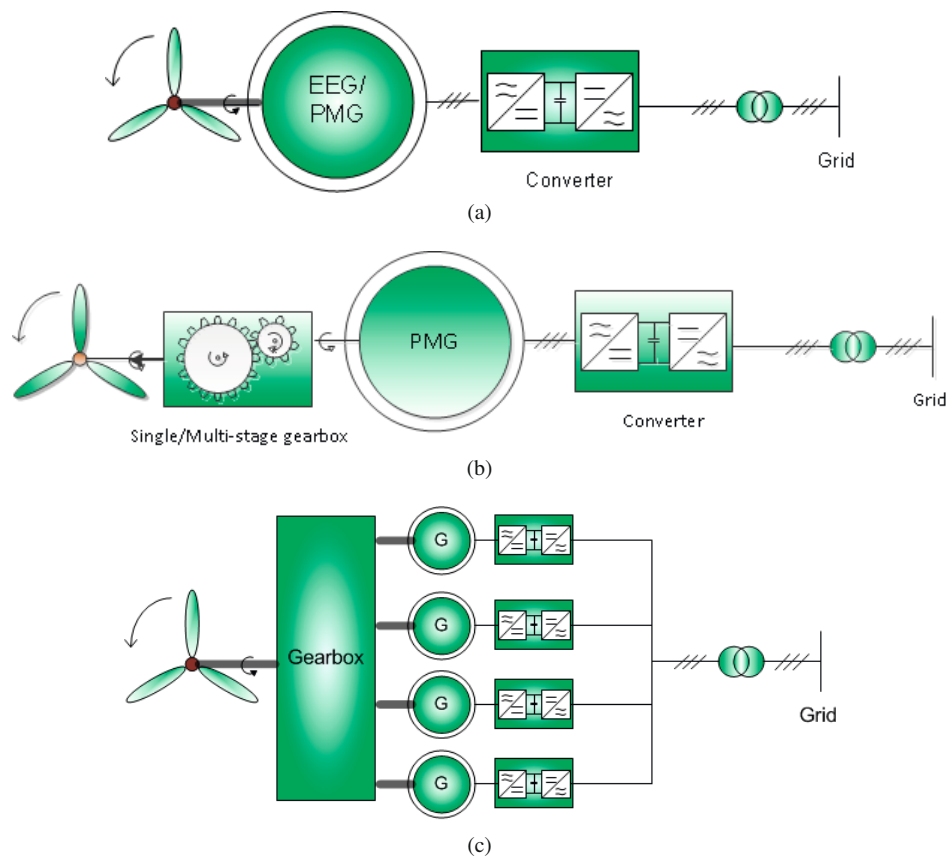
Figure 2.4: Wind energy conversion systems with synchronous generators: (a) dd-EEG/dd-PMG in variable-speed WECS; (b) sg-PMG/mg-PMG in variable-speed WECS; (c) Distributed drive train with synchronous generators.

geared drive train with single-stage/multi-stage gear box (Figure 2.4b), and distributed drive train with multiple PM machines (Figure 2.4c). So far, distributed drive train has not yet been used offshore.

The solution with dd-PMG combines the advantages of direct-driven scheme and permanent magnet machines. dd-PMG is coupled to the turbine rotor through the main shaft. The stator is connected to a full-scale converter for power and speed control (Figure 2.4a). PM material is incorporated in the rotor, which makes dd-PMG superior to dd-EEG for low-loss excitation. dd-PMG has large number of PM poles to facilitate the low speed operation; thereby a rotor with a large diameter is required to accommodate the PM poles. Because no excitation windings are needed, compared to dd-EEG, dd-PMG has smaller dimensions, lighter weight, improved reliability, and reduced maintenance cost.

From the system point of view, WECS with dd-PMG has a high energy yield, high efficiency, and high reliability. But the disadvantages of dd-PMG are obvious. dd-PMG is normally designed with large dimensions, and because of the large normal stress between the stator and the rotor, heavy structure mass is required to maintain the stiffness of the whole machine, especially for high torque rating application [3]. It is a key concern to reduce the weight and cost of the system with dd-PMG [3], [74].

Permanent magnet generator with single-stage gearbox (sg-PMG)

The sg-PMG, often referred as Multibrid, was first proposed in [75], and lately exploited in [76], [77]. A medium speed PM (100-120 rpm) machine is mechanically coupled to a single stage gearbox with the gear ratio of 1:6 to 1:7, and also a full-scale converter is used for power and frequency control (Figure 2.4b).

sg-PMG is a technology specially developed for offshore application, and can be regarded as a compromise between DFG and dd-PMG. Compared to DFG, the high speed stage of the gear box, the unreliable part, is eliminated. Compared to dd-PMG, the speed is higher and dimension is smaller, thus the cost is reduced.

Permanent magnet generator with multi-stage gear box (mg-PMG)

The system with mg-PMG is similar to variable-speed WECS with SCG, but PMG used (Figure 2.4b). In addition to the advantages of PM machine, mg-PMG has the advantage of low weight because of operating at high operation speed. The use of full-scale converter makes WECS with mg-PMG easily meet the requirement of grid codes.

2.3 Comparison

To a certain extent, drive train efficiency determines whether or not to invest in the wind power plant in focus. However, equipment datasheets normally provide rated efficiency only, and not all manufacturers are willing to share the efficiency curve at partial loads in public. This makes it necessary to model the efficiency in a proper way so that the performance of different drive trains can be compared. The efficiency of a drive train can be given by

$$\eta_{dt} = \eta_{gea}\eta_{gen}\eta_{con}, \tag{2.2}$$

where η_{gea}, η_{gen}, and η_{con} are the efficiencies of gearbox, generator, and converter, respectively.

2.3.1 Calculation approach

Gearbox efficiency

Four types of losses can be found in a gearbox: losses during the meshing, losses due to dipping, losses in bearings and losses in sealings. An explicit analytical method to calculate these losses is addressed in [79]. Generally, gearbox losses vary with the type of gear employed, and the loss in a certain type of gear has its own pattern. According to [80], planetary gears can be assumed to have 1% power loss per stage. Half of this loss is nearly constant, whereas the other half varies linearly with the transmitted power. Helical gears can be assumed to have 2% power loss per stage. To develop a general approach for calculating the gearbox losses, the following assumptions are made

- A three-stage gearbox has a planetary gear in the first and second stage, and has a helical gear in the third stage.

- A one-stage gearbox has a planetary gear only.

Then the losses in these two gearboxes are given by

$$P_{Lgear} = \begin{cases} p_{gear}(0.5 + 0.5\frac{P}{P_N}) & \text{for one-stage gear} \\ p_{gear}(3 + \frac{P}{P_N}) & \text{for three-stage gear} \end{cases} \tag{2.3}$$

where p_{gear} is 1% of the rated power, P is the working power and P_N is the rated power.

Generator efficiency

The generator efficiency model from ABB presented as curves in Figure 2.5 is used.
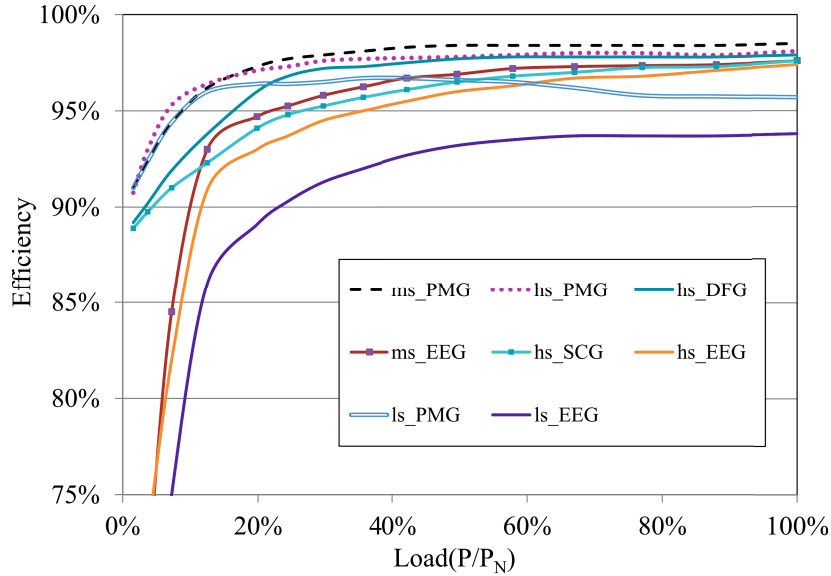
Figure 2.5: Efficiency vs. load for different generators [81] (hs, ms and ls are high speed, medium speed and low speed generators, and correspond to drive trains with three-stage gear, one-stage gear and direct drive, respectively).

Converter efficiency

A voltage source back to back converter is used. A simplified expression for the loss of a full-scale converter [82] is:

$$P_{Lconv} = \frac{p_{conv}}{31}(1 + 20\frac{T}{T_N} + 10\frac{T}{T_N}^2), \qquad (2.4)$$

where p_{conv} is the converter rated loss, T is the working torque and T_N is the rated torque. The loss of the converter for DFG is assumed to be one third of the loss of the full-scale converter.

2.3.2   Total drive train efficiency

The efficiencies of different drive trains for 3 MW WECS with rated wind speed of 12 m/s are presented in Figure 2.6. The following conclusions can be drawn:

- Systems with medium-speed (ms) and low-speed (ls) PMG have higher efficiency than other drive trains in the wind speed below 10 m/s. For wind speed above 10
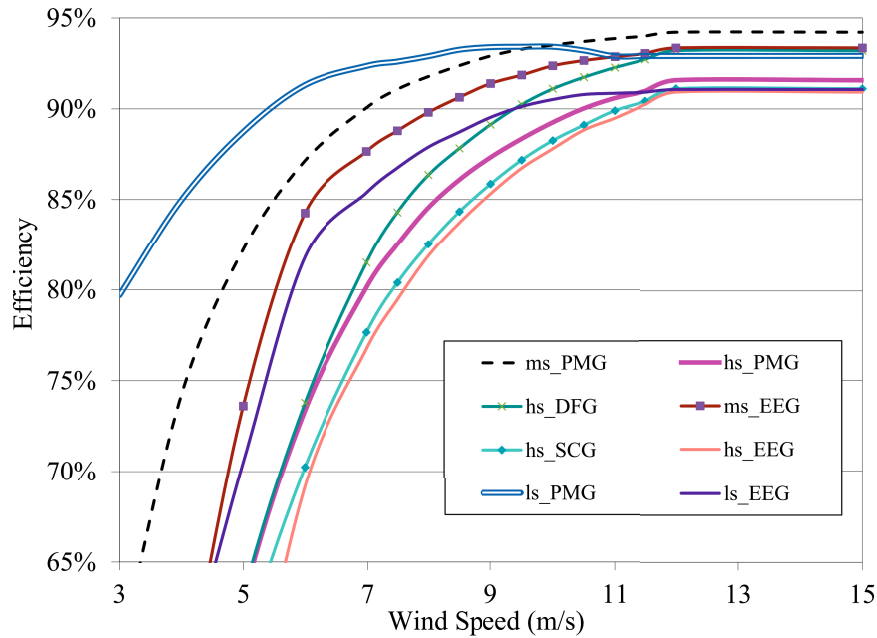
Figure 2.6: Efficiency of the different drive trains.

m/s, the system with ms_PMG has higher efficiency than the others. But a system with PMG does not always bring higher efficiency. For instance, system with hs_PMG has lower efficiency than systems with hs_DFG, ms_EEG, ls_EEG, but of course, the reliability and cost are not taken into account.

- System with EEG normally has lower efficiency, especially at low wind speeds. System with ms_EEG shows high efficiency, but this solution does not exist in the market, which is probably because of the reliability problems.

- System with hs_DFG offers low efficiency at low wind speed, but comparable efficiency around rated operation point to system with ls_PMG. This is due to the fact that low loss in the converter compensates the three-stage gearbox loss.

- Systems with hs_PMG, hs_SCG, and hs_EEG, offer low efficiency in the whole wind speed range.

- As aforementioned, hs_DFG and hs_SCG are the two dominant generators in the global operational offshore wind farm. However, DFG shows competitive efficiency, whereas hs_SCG does not.

40

2.4 New technologies and concepts

The conventional induction-machine-dominant solution for offshore industry has the problem to meet the need of high reliability and high efficiency at high rating per unit turbine. The turbines with the conventional direct-driven PMG technology are expensive when scaling up the torque. Therefore, new technologies and concepts are required and being developed in both industry and academia. These new solutions can be classified into three groups: upscale the current design, modify the current design, and develop new solutions. Fewer system components, lower generator mass, and higher efficiency are of the concerns.

2.4.1 Direct-driven DFG

It is attractive to investigate the direct-driven DFG. Because the converter has low rating, and there is no gearbox and expensive PM, the system cost is expected to be low, and the system reliability and efficiency are expected to be high. However, direct-driven generators are normally heavy and large, and a big air gap is required for the large-diameter structure. This is the challenge for the efficiency of the DFG. [83]-[85] propose an elastic structure, and the deformations in both the rotor and the stator are expected to be equalized. Fractional winding is used in the stator to allow the low leakage inductance. In rotor, the slot per pole per phase is kept as high as possible to decrease the no-load current. However, a detail analysis of torque ripples is necessary to make this design convincing.

2.4.2 Conventional direct-driven RFPMG

It is now common to find iron-cored RFPMG in wind turbines. Therefore, it is straightforward to upscale this mature technology. [86] shows an air-cooled 10 MW PM machine based on the conventional iron-cored technology. In this machine, most of the mass goes to the constructure that accounts for 80% of the total mass, though this machine is not optimized.

One approach to minimize the machine dimension is to use more efficient cooling methods. Direct water-cooling PM generator is considered in [49], [87]. Tooth coil is used with the slots per pole per phase at 0.4 for a six phase machine. The stator has 12slots - 10poles segments. With the electric load of 150 kA/m, the volume of this 8 MW machine is only 34% of that for the 10 MW machine from [86].

2.4.3 Direct-driven iPMG

iPMG has negligible normal force between stator and rotor. Therefore, the requirement to the strength of the supporting structure is relatively low, and the total weight and cost can be reduced dramatically [2], [25]. In ironless machines, the iron loss in rotor can be neglected, and has no cogging torque. The synchronous inductance is also low, which allows a cheaper full-scale converter. However, in ironless machines, normally more magnetic material is required to produce sufficient torque, and because of directly facing the rotor field, considerable eddy current loss is expected in the stator winding if conventional rectangular wires are used. Furthermore, the design of a large-diameter support structure is also a challenge.

2.4.4 Superconducting generator

Using superconductive material in electrical machines can reduce the synchronous reactance and the excitation losses, increase the magnetic flux density in the air gap, and eliminate ferromagnetic cores, therefore, high efficiency and compact design can be achieved [88]-[90]. When compared to PM, up to 50% of the generator mass can be saved with High Temperature Superconducting (HTS) generator, which also means that the cost of construction and installation can be significantly reduced. Furthermore, because of the low driving voltage (around 100 mV), the rotor of the HTS generator is subject to low thermal ageing of the insulation, thus without risk of insulation breakdown.

Because of the high loss at AC condition (in stator) and the challenge to remove it, the super conducting winding is currently limited to DC condition, i.e., in rotor for producing excitation field, and the stator winding still employs copper winding. The main challenge of the super conducting generator is the cryocooler used to cool down the rotor, which adds extra cost, and the reliability of the cooling technology has not been proven yet for offshore operations. Nonetheless, HTS generator is a promising candidate for future large offshore wind turbines.

2.4.5 High-voltage variable-capacitance DC generator

A high-voltage variable-capacitance DC generator is investigated in [91], [92]. Contrary to conventional magnetic machines where the power flows through magnetic field, this machine performs the energy conversion by varying capacitance in electric field as the rotor rotates. The power is proportional to the square of the terminal voltage that relies on the air gap thickness. A 7.3 MW generator is reported to have 200 kV output with 4 mm air gap. Because of the high terminal voltage and vacuum gap employed, high efficiency can be expected. Furthermore, there will be no need for a transformer and a AC-DC converter station like in conventional HVDC offshore wind farms. However, this concept

is still far from practical application. One key factor is the low power density, which makes this machine bigger than conventional machines. If the reliable high voltage insulation across the gap can be realized, the generator dimension and mass can be reduced. Nonetheless, the early stage estimation shows that the total system mass is comparable to conventional systems.

2.5   Summary

It is found that the current dominant solution for offshore wind energy conversion systems is mgT, and most of the generators in the operational offshore wind farms are induction machines (DFG and SCG). This is due to the technological maturity at the power level of 3 MW.

Induction machines normally have low efficiency at partial load, but the comparative study shows that the system with DFG can have the comparable efficiency as the system with low-speed PMG at rated load. The systems with PMGs normally have high efficiency at both partial load and full load.

Reducing the number of system components, low total mass, and high efficiency are of the concerns in the development of high-power generator technologies. Among the new concepts, the iPMG seems promising. It is lighter than the conventional iron-cored PMG and the dd-DFG; the rotor of the iPMG is simpler than that of the super conducting generator, therefore, the rotor reliability is less of a concern; the PMG technology has been applied to MW wind turbines for more than a decade, whereas the high-voltage variable-capacitance DC generators are normally used in microscale or nanoscale level.

Chapter 3

Iron-cored PMGs

This chapter investigates the weight of iron-cored PMGs. In Section 3.1, the technology frontier of wind power generators is investigated and obtained by a statistical analysis of over 90 generators. Following this statistics, a method is developed for estimating the total weight of iron-cored PMGs. In Section 3.2, the weight of the active parts (windings, stator iron, PMs, and rotor iron) for the generators ranging from 6 MW to 10 MW is calculated by optimizing machines with GA and finite element analysis (FEA). In Section 3.3, the optimization results are further treated to obtain the variations of the generator active weight, inactive weight (supporting structures) and total weight as the generator power grows. Some general conclusions are drawn in Section 3.4.

3.1 Introduction

The reason to develop iPMG technology is attribute to its feature of being lightweight, compared to iron-cored PMG technology. A complete elaboration of this argument was presented in [3], which used an analytical method to do the mechanical design of iron-cored PMG with power up to 5 MW. It further concluded that, the percentage of the structural weight in the total weight increases faster than the increase of the machine torque.

For a PMG with certain power, its weight depends on PM magnetic property, cooling method, and speed. Using high energy-density PM can reduce machine size, but also easily boost up the machine cost, and make the machine expensive to afford in the market, so it may be pragmatic to use low-cost PM for offering matching performance. As has been shown in Chapter 2, the volume of water-cooling 8 MW machine can be only 34% of that for a air-cooling 10 MW machine, therefore, a PMG cooled more effectively will be lighter than those less effectively cooled. If the PM magnetic property and cooling method are fixed, doubling a machine's speed, will reduce the machine size to half. Unfortunately,

in [3], the cooling method is unknown. Compared to a 10 MW direct-driven PMG rated at 12 rpm [93], the speed for a 5 MW direct-driven wind turbine was set to 12.5 rpm, which is obviously too low in offshore application. Therefore, the corresponding conclusion should be examined, better with other modelling method.

3.2 Total weight

The first task of an electrical machine design is to determine the machine dimension for a given machine specification and material electromagnetic properties. Take a RFPMG as example, the machine dimensioning is governed by

$$T_N = k_T V B_q E_L, \tag{3.1}$$

where k_T is torque constant, V is machine volume, B_q is magnetic load and E_L is electric load. Even though electrical machines vary in dimension and weight, the maximal magnetic load and electric load depend on the material electromagnetic properties, thermal and mechanical designs, and do not change so much.

Generator weight affects not only the cost of the generator itself, but also the cost of transportation, lifting etc. The total weight of a RFPMG can be expressed with

$$M_t = V \rho_{av}, \tag{3.2}$$

where ρ_{av} is machine average density. To compare different designs, two criteria are widely accepted: torque density T_d and power density P_d, which are given by

$$T_d = \frac{k_T B_q E_L}{\rho_{av}}, \tag{3.3}$$

$$P_d = \frac{k_P B_q E_L n_N}{\rho_{av}}, \tag{3.4}$$

where k_P is power constant, n_N is the machine rated speed.

To compare different generator technologies, the T_d and P_d of over 90 generators for WECS are investigated. Most of these generators are commercial iron-cored PMGs, some are academic designs, and the drive trains include multi-stage and direct-driven solution. The results are plotted in Figure 3.1.

Note that this map shows only the best available designs from each power range. The generator speed is not indicated in the map, but it is possible to find the corresponding speed of the plotted generators on the map, and it is easy to conclude that low-speed machines will tend to lie on the lower right, and high-speed machines on upper left. An area, which clearly demonstrates the technology limitations, is marked out to represent today's technology frontier. Some declared coming designs (e.g. superconducting generators) on

the lower right corner of the map (i.e. in the low speed region) look very promising. This map can be used to evaluate the goodness of any generator design. The designs located to the right and up relative to the area will stretch the technology limits, whereas the designs to the left and down relative to the area will be worse than the state of the art.
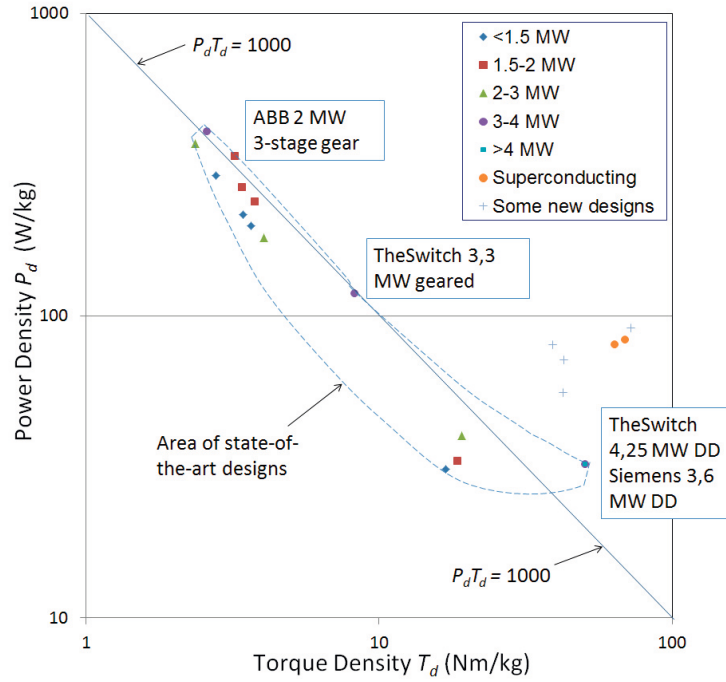
Figure 3.1: Power density vs. torque density in logarithmic scale (joint work with Smart-Motor AS).

It is found that the upper edge of the technology frontier approximately follows the line corresponding to the expression

$$P_d T_d = 1000 W Nm/kg^2. \tag{3.5}$$

Using (3.5), the generator weight for any power rating and speed can be predicted as

$$M_t = \frac{97.7 P_N}{\sqrt{n_N}}, \tag{3.6}$$

where the units for M_t, P_N and n_N are ton, MW, and rpm respectively.

The weights of direct-driven wind power generator up to 10 MWs are estimated in Figure 3.2 by using (3.6) while taking into account the rotation speed reduction due to blade strength capability. It shows the weight of high-power machines grows faster than the power rating. For instance, the weight of 10 MW machine is almost three times the weight of 4 MW machine. It is worth to mention that the weight estimation based on technology frontier shows higher accuracy compared to the estimation in [94] in predicting the weight of commercial design [95] and academic design of 10 MW [86].

In academy and industry, researchers are trying to break the current limitations and design direct-driven generators with torque density in 50-80 Nm/kg, power density in 50-100 W/kg and $P_d T_d$ from 2000 to 6000 WNm/kg^2, by using PM generators with new topologies, or superconducting generators.
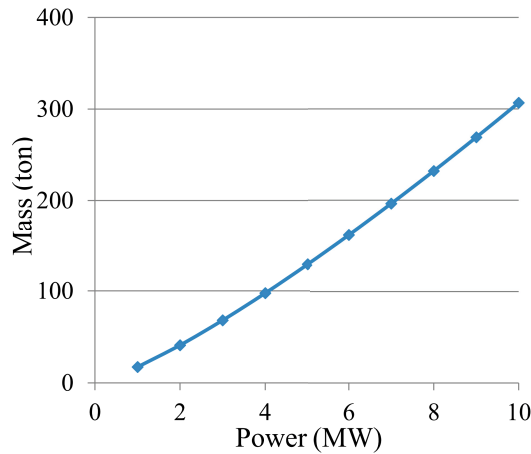
Figure 3.2: Estimated weight of direct-driven generators up to 10 MW.

3.3 Active weight

The estimation of generator's active weight has to be conducted with electromagnetic design. To obtain the optimal design, an optimization approach based on GA is used. A FEM code driven by the GA is used to do the field calculation. The weight of inactive parts (supporting structures) is therefore obtained by taking away the active weight (obtained from the machine optimization) from the total weight (calculated with Equa. 3.6). The specification of the studied generators is shown in Table 3.1. Free variables and constraints used in optimization are given in Table 3.2 and Table 3.3.

The studied generators range from 6 MW to 10 MW. All the machines are rated at 3.3 kV. Note the speeds of these machines are determined according to the speeds for

Table 3.1: Generator specification.

Parameters	Value				
Power (P_N), MW	6	7	8	9	10
Speed (n_N), rpm	16	15	14	13	12
Stator voltage (U_N), kV			3.3		
Phase number (m)			3		
Air gap (g), mm			$0.1\%D_o$		
Fill factor (k_f)			0.65		
1st AC resistance ratio (k_{r1})			1.1		
Staking factor (k_s)			0.95		
PM B_r at working temperature, T			1.2		
PM relative permeability			1.05		
Slot per pole per phase (q)			1		
Number of parallel branch (a)			1		
Slot wedge thickness (h_W), mm			5		
PM specific cost, €/kg			80		
Copper specific cost, €/kg			27		
Iron specific cost, €/kg			16		

Table 3.2: Free variables.

Parameters	Range
Pole number (p)	108-540
Outer diameter (D_o), m	6-10
PM thickness (h_M), mm	5-100
Thickness of rotor back iron (h_{ry}), mm	5-100
Thickness of stator back iron (h_{sy}), mm	5-100
Ratio of slot height over slot width (k_{ts})	4-10
Ratio of PM width over pole pitch (k_M)	0.5-0.9
Ratio of tooth width over slot pitch (k_t)	0.3-0.7
Current density (J), A/mm^2	2-5

commercial 5-MW [96] and 10-MW [97] direct-driven PMGs, given that turbines with lower power rating tend to have smaller rotor diameter and thus higher rotation speed. The air gap thickness is set to 0.1% of the air gap diameter, according to the proposal in [63]. The AC resistance ratio reflects the proximity effect and skin effect, and depends on the frequency, temperature, winding types, winding size, and machine geometry. In this case, according to the test results in [98] (rectangular wires), the 1st AC resistance ratio is set to 1.1 for the full-pitch winding used. Note that the material specific costs depend on many factors, and in particular the cost of permanent magnet fluctuates dramatically in the past few years. The specific costs given in Table 3.1 (and also in following chapters) are based on the information provided by the industrial parter of this research. The electrical steel is DW460-50 (Appendix B).

Table 3.3: Constraints.

Parameters	Range
Frequency (f), Hz	10-60
Slot pitch (τ_s), mm	≥ 20
Cross section of one turn coil (S_T), mm^2	≥ 5
Aspect ratio	≤ 0.3
Flux density in yokes of stator and rotor, T	≤ 5
Electric load (E_L), kA/m	≤ 50
Population size	1000
Number of generation	50

There are 9 free variables in this optimization (Table 3.2). By free variables, it means they are the direct input for the machine design and optimization, and not dependent on any other variables. The outer diameter is constrained to be greater than 6 m, which is a challenge to the ordinary transportation. However, it is assumed this is out of question by modularising the generator and using offshore-dedicated logistics. The ratio of slot height over slot width is constrained to avoid over stressing the teeth mechanically, the upper and lower boundaries are set according to the suggestions in [99]. The current density is constrained according to the recommendations for air-cooling PMGs [100].

The constraints given in Table 3.3 are set from the perspectives of construction limitations, thermal and mechanical reliability. Aspect ratio (the machine axial length divided by its outer diameter) is limited according to the recommendation in [101]. The settings of the flux density in the yokes of stator and rotor eliminate the unrealistic calculations on one hand, on the other hand, they leave the loss calculation (efficiency optimization) to determine the proper level of the field in the yokes of the stator and the rotor. The electric load is set according to [100]. This optimization is a multi-variable integer-mixed problem. Handling integer-mixed problem is a challenge to many optimization tools. It requires the variable is still integer after treated by the creation, crossover, and mutation functions. For such a mixed-integer optimization problem, the GA of the Matlab optimization toolbox suggests a population size of 90. However, in the practical calculation, it is found that this suggestion does not work well. So the practical population size is increased to 1000. To grasp the global minimum, the maximal generation is set to 50, which is a large generation size but necessary to make all the optimization converged. It is possible to get a better result by running more populations; however, it is found that the result does not get much improved.

The machine type is the RFPMG with the topology of outer rotor, surface-mounted magnets (Figure 3.3).

In the design of these machines, 2D static FEA (SFEA) is conducted for field calculation, and GA is employed to search the optimal designs. The FEA tool is FEMM 4.2 [102], an open-source code which supports scripting; Matlab script is used for calculating the basic parameters and driving FEMM (creating geometry, generating mesh,

solving, and postprocessing). The optimization method is the GA of the Matlab optimization toolbox. The optimization is parallelly executed with the Matlab tool *matlabpool*, which enables the parallel process in a shared-memory platform. However, the maximal number of parallel processes depends on the CPU core number (a limitation due to the Matlab license used). All the calculations were run on four workstations and a computing server (see Appendix C for computing lab configuration and layout).

FEMM does not have the feature of adaptive mesh, therefore, a special attention is taken in the preprocessing script so that a sufficiently fine mesh is generated. Figure 3.4 plots the air-gap fields (for a random-selected model, shown in Figure 3.5) calculated with FEMM and the commercial code, Maxwell [103]. The agreement confirms that the developed script can create a fine mesh, and FEMM can solve it correctly.
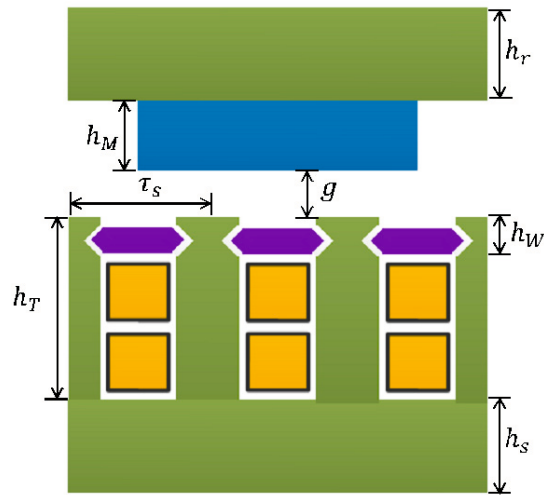
Figure 3.3: Generator topology.
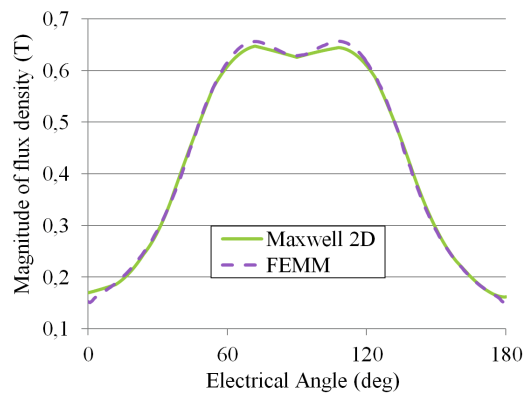
Figure 3.4: Maxwell 2D vs. FEMM.

50
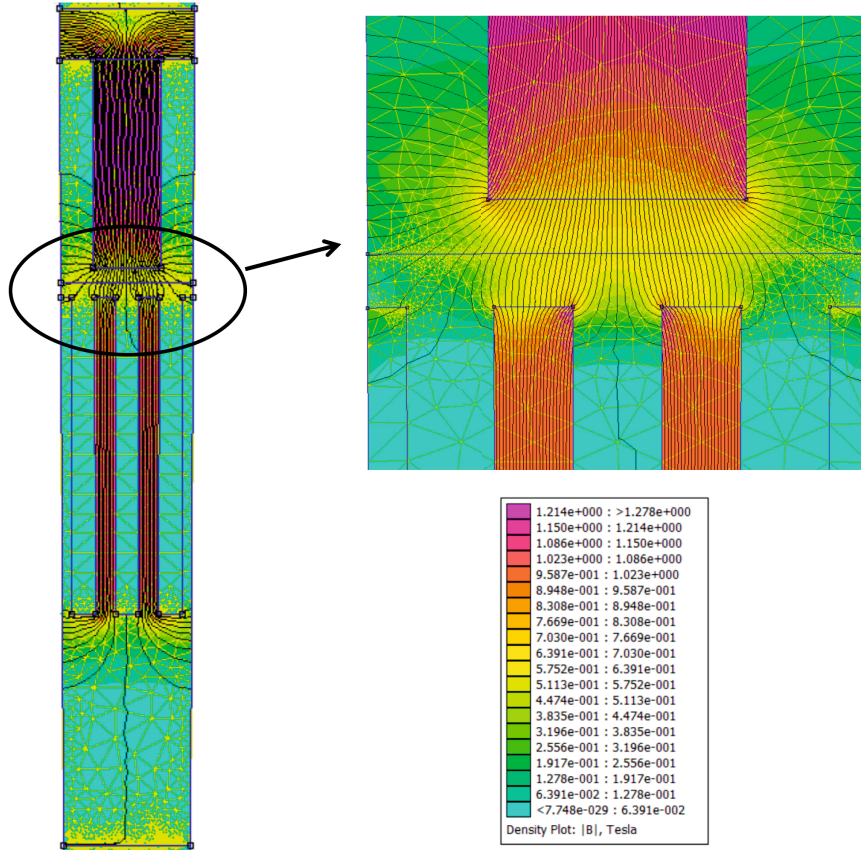
Figure 3.5: FEMM model: mesh and the distributions of the flux density.

3.3.1 Design procedure

The design procedure is illustrated in Figure 3.6. For each design case, the field and inductance are calculated with 2D SFEA. The iron loss is calculated with 2D transient FEA (TFEA), which is actually a series of SFEAs acounting for the change of the rotor position with sliding mesh. κ is the voltage drop ratio (the magnitude difference of rated back-EMF and rated voltage). This design method is embedded into an optimization procedure. The GA initialization involves several basic configurations such as the boundaries of the free variables, number of free variables, the index of the integer, the fitness function, the constrain function, initial population, number of populations, and number of generations. Because there is an integer in the free variables, there is no much freedom to select the functions of creation, crossover, and mutation. The default Matlab functions are used to generate new population.
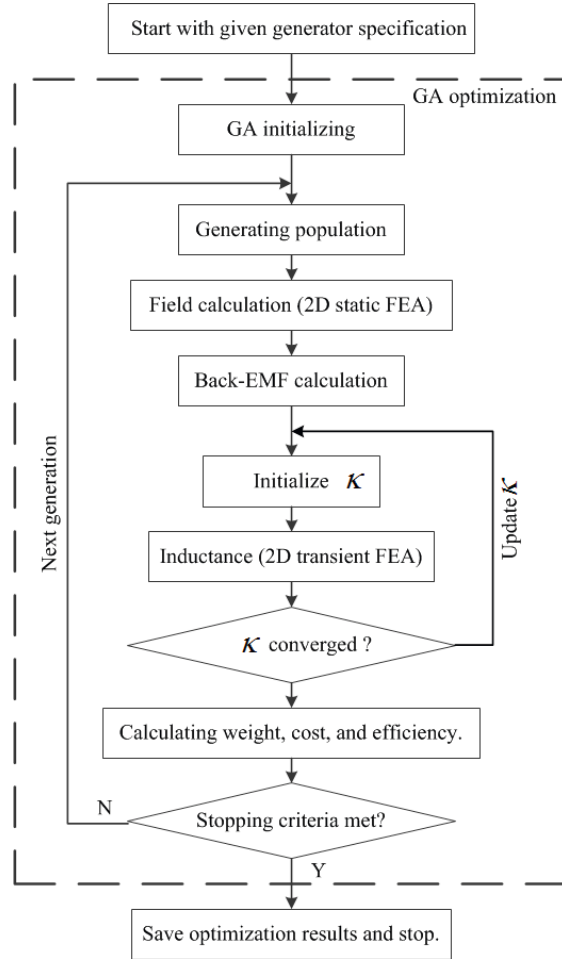
Figure 3.6: Design procedure (κ: voltage drop ratio).

3.3.2 Modelling method

The first task of this design method is to determine the number of turns (N_s).

The maximal N_s determined by different considerations, are given by (3.7), where $N_{s-s}, N_{s-J}, N_{s-E_L}$ are the number of turns per slot determined by the slot area, current density, and electric load, respectively. Note that the first equation calculates that, with the given slot dimension, if use the wires with the minimal cross section, how many number of turns are required in the whole slot for a double-layer winding; the second equation calculates that, with the given slot dimension and current density, how many number of turns are required in the whole slot so that a single turn can carry rated current; the third equation calculates that, if the maximal electric load is allowed at the air-gap diameter,

52

how many number of turns are required in the whole slot.

$$\begin{cases} N_{s-s} = \frac{(h_t - h_w)(1 - k_t)\tau_s}{5} \\ N_{s-J} = \frac{\sqrt{3}(h_t - h_w)\tau_s(1 - k_t)k_f JaU_N}{P_N} \\ N_{s-E_L} = \frac{(D_a - g)E_L\pi}{qpm} \end{cases} \tag{3.7}$$

The practical N_s is determined by the minimum of N_{s-s}, N_{s-J}, and N_{s-E_L} (3.8).

$$N_s = min(0.5N_{s-s}, 0.5N_{s-J}, 0.5N_{s-E_L}). \tag{3.8}$$

Once N_s is determined, the coil size, the current density and electric load are also determined, according to (3.7).

Another key parameter to be calculated is the machine length. This is done by adjusting the back-EMF so that the rated voltage is obtained at the terminal. The back-EMF per unit length (E) is calculated with (3.9), then the generator effective length (l_{ef}) is calculated according to the rated voltage and the voltage drop ratio at rated load (3.10).

$$E = \frac{\pi n_N k_{w1} k_{le} B_{p1} N_s Q D_a}{30\sqrt{2}ma}, \tag{3.9}$$

$$l_{ef} = \frac{(1 + \kappa)U_N}{E}, \tag{3.10}$$

where k_{w1} is the winding coefficient, k_{le} is flux leakage, B_{p1} is the magnitude of the fundamental flux density, and Q is the total number of coils.

The synchronous inductance (L_s) consists of three parts: self-inductance with slot leakage (L), mutual inductance (M), and end-connection leakage inductance (L_e). L and M are calculated in the postprocessing of 2D SFEA. First, do the 2D SFEA with only one phase coil excited (rated current), obtain the stored magnetic energy (W_M) in the SFEA postprocessing, L is then obtained with $L = 2W_M/I_N^2$. Second, calculate the mutual flux (Φ_M) linking to one of the other two phases, then M is obtained with $M = \Phi_M/I_N$. In the above operations, to avoid the disturbance from the PM flux, the magnetization of PM is set to 0, this is the drawback of this method. Analytical method is used to calculate L_e (3.11) [12].

$$L_e = \frac{1.2\pi f \mu_0 l_e N_1^2}{p}, \tag{3.11}$$

where μ_0 is the vacuum permeability, l_e is total length of end connection in one side, N_1 is the total number of coils per phase.

The phase resistance is given by

$$R_{AC} = \frac{4k_{r1}qpN_s^2\rho_{cu\_t}l_{ef}}{a^2k_f(h_t - h_w)\tau_s(1 - k_t)(k_s + l_e)}, \tag{3.12}$$

where ρ_{cu_t} is the copper conductivity at operating temperature.

The calculated voltage drop ratio is given by

$$\kappa = \frac{\sqrt{(U_N + R_{AC}I_N)^2 + (2\pi f L_s I_N)^2}}{U_N} - 1,$$ (3.13)

where I_N is the rated current.

The total losses consist of four parts: bearing and rotational losses, copper loss in winding, iron loss in both the stator and rotor iron, and eddy current loss in PM. Bearing and rotational losses are assumed to be 0.5% of the rated power [63], [104]. The copper loss and iron loss are calculated with (3.14) and (3.15).

$$P_{cu} = mI_N^2 R_{AC},$$ (3.14)

$$P_{fe} = l_{ef} \iint \sum_{k=1}^{N_e} \sum_{f_k=1}^{N_f^k} P_k^f(f_k, B_k^f)dS,$$ (3.15)

where f_k is the harmonics order at k^{th} element, B_k^f is the magnitude of the fth flux density at k^{th} element. The iron loss P_k^f is obtained by looking up loss table of the steel sheet (Appendix B). N_k^f is the total number of harmonics at k^{th} element, and N_e is the total number of elements in the yokes of stator and rotor. The harmonic components of each element are obtained by doing FFT after the 2D TFEA. Note the flux density is a vector, there are two iron loss components in the iron, one in the x direction and another one in y direction. The total iron loss is obtained by summing up these two loss components (each is calculated with Equa. 3.15).

The eddy current loss in PM depends on the current loading and the slot type. In this design, a simple loss model is used [63], and this loss is calculated with

$$P_e = k_e p \tau_p k_M l_{ef},$$ (3.16)

where k_e is the PM surface loss density (300 W/m^2), τ_p is the pole pitch.

3.3.3 Optimization

The determination of the fitness function is subject to the designer's research interest and preference. Normally, several objectives are within the research interest, and the designer has to do a trade-off among these objectives. The optimization results are directly influenced by how the fitness function is formulated and the setting of the weighting ratio to different objectives. Generally, it is not wise to pursuit always the high efficiency machine while ignoring the penalty on cost. In this research, it is interesting to know the weight of the optimal machines for each power rating. Here, the optimal machine is defined by

Table 3.4: Optimization results.

Parameters	Value				
Power (P_N), MW	6	7	8	9	10
Pole number (p)	382	352	336	318	418
Outer diameter (D_o), mm	7558	7920	8894	9591	9903
PM thickness (h_M), mm	16.6	10.4	18.9	17.4	17.6
Thickness of rotor yoke (h_{ry}), mm	11.5	14.3	21.4	23.5	23.6
Thickness of stator yoke (h_{sy}), mm	12.1	9.9	15.3	17.4	29.9
k_{ts}	6.86	5.74	5.41	6.10	5.39
k_M	0.75	0.769	0.83	0.68	0.73
k_t	0.66	0.60	0.65	0.68	0.61
Current density (J), A/mm^2	2.65	2.94	2.90	2.70	2.68
Machine length, mm	1801	2166	1754	2111	2198
Frequency (f), Hz	50.9	44.0	39.2	34.5	41.8
Aspect ratio	0.240	0.276	0.199	0.222	0.224
B_{p1}, T	0.84	0.72	0.89	0.78	0.77
Stator loss, kW	225	248	265	300	375
Rotor loss, kW	51	55	47	81	79
Other loss, kW	30	35	40	45	50
Efficiency, %	95.01	95.23	95.65	95.35	95.06
PM weight, ton	3.974	3.217	5.753	5.608	6.559
Copper weight, ton	7.688	13.223	10.027	14.979	15.783
Total iron weight, ton	16.781	21.696	24.507	37.466	41.459
Total active weight, ton	31.975	43.696	47.838	68.833	75.434
Total active cost, M€	0.794	0.962	1.123	1.453	1.614
Calculation (clock) time, hours	255.83	188.61	258.06	158.89	215.28

- The efficiency is greater than 95%.

- The active cost is minimal.

3.3.4 Calculation results

The calculated parameters of the optimal machines at each power are given in Table 3.4.

As it shows, the pole numbers for all the five designs lie in the region 318-418. Considering the different speeds, the corresponding frequency ranges is 51-34 Hz. The diameters of the optimal machines increases as the power grows, and only the optimal 10 MW machine has the diameter close to 10 m (the upper boundary of outer diameter). The PM thickness lies in 10-19 mm. The optimal 7 MW machine has the smallest PM thickness, and therefore the lowest air gap flux density, furthermore, its stator back iron does not need to be thick. The optimal machines have the k_{ts} 5-7, indicating the deep-slot config-

uration. k_M and k_t lie in 0.68-0.83 and 0.60-0.68 respectively, which is quite normal for this type of machines. The current density is less than 3 A/mm^2, which is not high but still reasonable for air-cooling machines. Air gap flux density is low, which contributes to low-cost machines. The dominant loss is the copper loss. All the optimal machines have the efficiency less than 96%. Most of the active weight goes to the iron, and the copper weight is roughly two times the PM weight. All the calculations ran more than a week, and some more than ten days.

3.4 Variation of generator weight

Equa.(3.6) calculates the total generator weight; the weight and cost the optimal machines for 6 MW - 10 MW are given in Table 3.4; therefore, the corresponding weight and cost of the inactive parts can be also obtained. These calculation results are summarised in Figure 3.7. Following conclusions are drawn:

- For the investigated power range, the dominant part of the total generator weight/cost is the weight/cost of the inactive parts, which accounts for more than 70%/60% of the total weight/cost. As the power grows, this percentage changes slightly, this is different to the observation reported in [53] because of the different generator speeds. Note that as the machine power (also torque) increases, the percentage of the structural weight in the total weight decreases slightly. This is different with the finding reported in [3] (*at higher torque ratings, the structural mass is a greater proportion of the total machine mass*).

- Torque density increases with 0.95 Nm/kg per MW, and power density decreases with 1.35 W/kg per MW.

- The averaged specific cost (total cost divided by total weight) is around 17.6 €/kg, however, the cost of power (total cost divide by power) slightly increases with 0.014 €/W per MW. Note that the averaged specific cost for 8 MW generator is higher than that for generators at 7 MW and 9 MW. This is because the 8 MW generator obtained from the optimization (Table 3.4) has a higher air gap field density, thus a higher total active cost. The same reason also applies to 6 MW generator.

- For high-power generators, it is desired to have the generator with lightweight inactive parts to reduce the total weight and cost.

- Higher-power generator has higher cost of power, therefore this additional cost should be paid back by the rest parts of the turbine, otherwise it is not economic to have high-rating turbine.
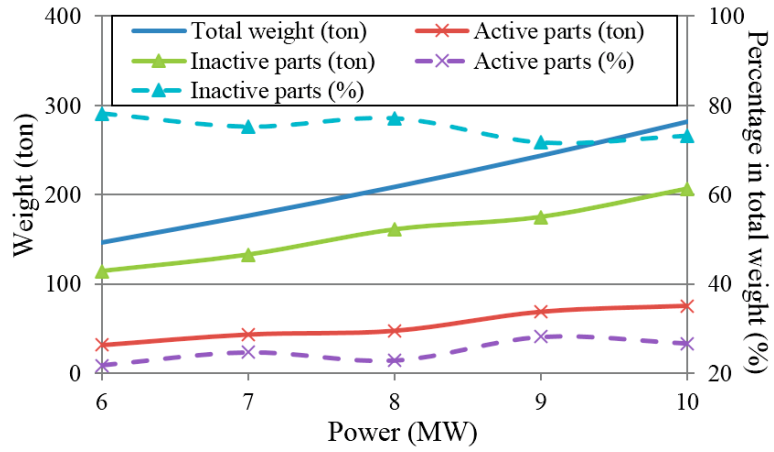
(a)
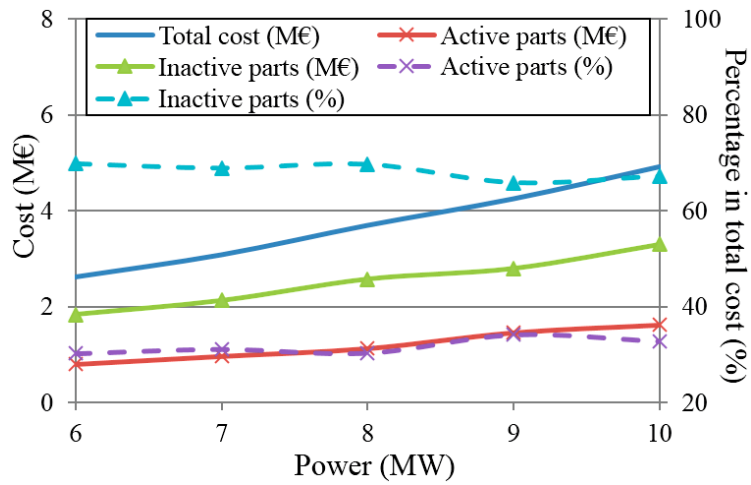
(b)

Figure 3.7: (a) Weight vs. power; (b) Cost vs. power. (*Continued.*)
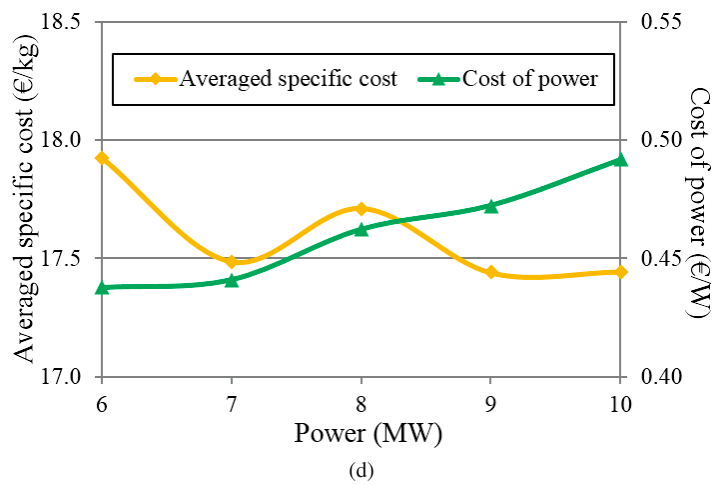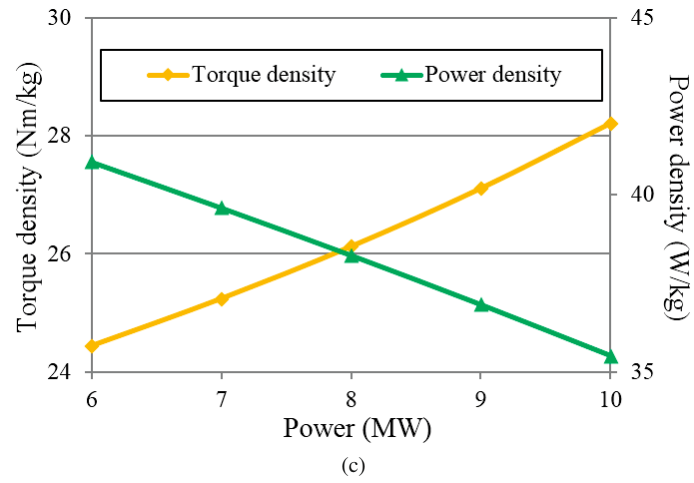
Figure 3.7: (c) Torque density and power density vs. power; (d) Averaged specific cost and cost of power vs. power.

3.5 Summary

This chapter presents an in-depth investigation of the iron-cored PMG technology. A tool is developed to present the technology frontier and evaluate other technologies by comparing their torque density and power density. The generator total weight is estimated with a simple but accurate equation. The weight of the generator active parts is obtained by optimizing machines with 2D FEA and GA.

It is found that most weight and cost of the iron-cored PMGs go to their inactive parts, which implies that using iron-cored PMGs is not a weight-/cost-effective solution for high-power wind turbines. Therefore, it is necessary to develop the technology for lightweight generators.

Chapter 4

iPMGs

This chapter investigates and compares the performances of possible iPMG topologies with the help of FEM and GA. Section 4.1 introduces the features of iPMGs; Section 4.2 discusses the practical aspects on designing the iPMG and implementing this technology in offshore wind turbines; Section 4.3 presents the modelling and optimization methods used in the comparative study; calculation results are presented and discussed in Section 4.4 and 4.5; the validations of the modelling and optimization methods are given in Section 4.6; Section 4.7 compares the total weight and cost of an iPMG and an iron-cored PMG both rated at 10 MW 12 rpm.

4.1 Introduction

Compared to iron-cored machines, ironless machines are characterized with lower tangential stress and negligible normal stress between rotor and stator [2], [4], [25], [26]. Lower tangential stress means the lower torque-producing capability, and therefore a large-diameter structure should be used. Typically, having a large diameter will pose a challenge to the design of the carrying structures. However, because the attraction force between the stator and the rotor is negligible, the mechanical carrying structures of ironless machines can be made light and reliable at much larger diameter than that of iron-cored PMGs. Therefore, the designers have the freedom to increase the diameter and achieve an extreme torque.

The advantages of extreme torque and lower weight are though obtained at the cost of a stronger magneto-motive force (MMF) to overcome the high magnetic reluctance of the ironless stator. Normally, this requires a larger amount of permanent magnet material, thus increases the iPMG cost, which can be a major challenge for the implementation of this technology in the cost-sensitive markets.
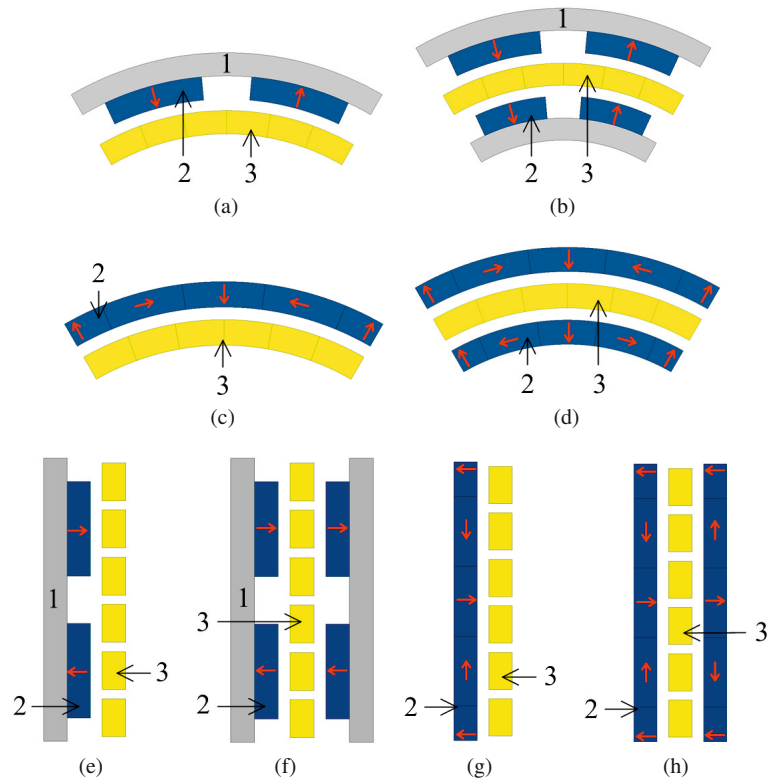
Figure 4.1: Studied machines (1: rotor core, 2: PM, 3: stator winding): (a) one-rotor conventional-array RFPMG (1R-CA-RFPMG); (b) two-rotor conventional-array RFPMG (2R-CA-RFPMG); (c) one-rotor Halbach-array RFPMG (1R-HA-RFPMG); (d) two-rotor Halbach-array RFPMG (2R-HA-RFPMG); (e) one-rotor conventional-array AFPMG (1R-CA-AFPMG); (f) two-rotor conventional-array AFPMG (2R-CA-AFPMG); (g) one-rotor Halbach-array AFPMG (1R-HA-AFPMG); (h) two-rotor Halbach-array AF-PMG (2R-HA-AFPMG).

Several ironless concepts are being considered in the wind power industry [25], [34], e.g. one-rotor conventional-array RFPMG (1R-CA-RFPMG) as shown in Figure 4.1a, two-rotor conventional-array AFPMG (2R-CA-AFPMG) as shown in Figure 4.1f, and MS-AFPMG. Unfortunately, there is no comparative study of these concepts and systematic investigation on other possible concepts.

4.2 Practical aspects on application and design

4.2.1 Turbines and energy conversion systems

For their large dimensions, iPMGs demand the dedicated wind turbines. In [25], [34], installation variants were investigated. Here, the main idea is to have the active parts of the generator integrated to the turbine structures, i.e., sharing the supporting structures with blades/hub/nacelle, so that the total mass can be minimized. In such a circumstance, the generator will not have independent inactive parts.

Modularized iPMG can be used in the conventional direct-driven drive train [2], [4], [25], [86], and also in the redundant system [105] for fault tolerance.

4.2.2 Structural reliability

Maintaining the clearance of the air gap is crucial for the reliability of large-diameter structure like iPMG. In this research, the thickness of the air gap is set to 0.15% of the machine outer diameter. This is different from the widely accepted proposal (0.1% of the air gap diameter) for the design of the iron-cored PMG [63], [86].

Even though iPMGs have negligible rotor-to-stator force, the machines will have to bear the driving torque, the force caused by electrical faults, and significant rotor-to-rotor forces if there are multiple rotors. This demands the proper design of the supporting structures to maintain machine reliability while still having low total mass [4], [26].

4.2.3 Generator types

Eight types of iPMGs (Figure 4.1) are modelled and studied to find out the optimal machines. All these machines have segmented stators, and the windings in adjacent stator segments are physically-separated.

4.2.4 Winding and stator segmentation

A two-set concentrated winding is used because of its high equivalent coil fill factor. An example on the development of this winding is shown in Figure 4.2. The stator is segmented into several parts for easing transportation and enabling the possibility of fault tolerance as well. This segmentation is achieved by removing certain number of coils
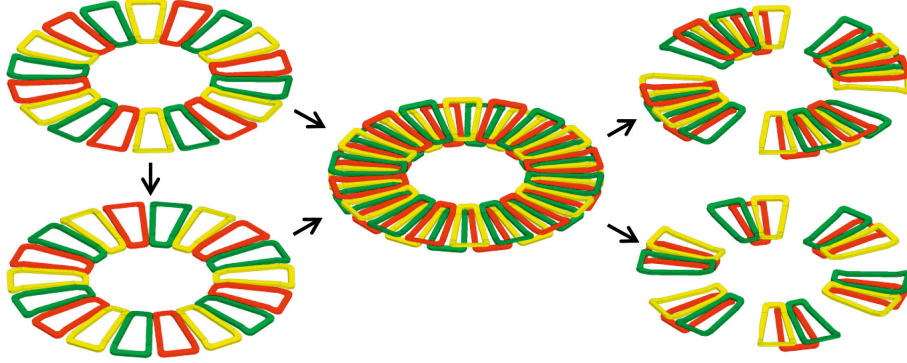
Figure 4.2: Development of a segmented two-set concentrated winding for a 24-pole ironless AFPMG (start with a bended concentrated winding, the top set; mirror it, and turn it counter-clockwise with 1.5 coil pitch, get the lower set; overlap the two sets, get the unsegmented winding with all the active conductors lying in one plane; segment the winding according to the number of segments).

regularly from the whole stator. The number of coils to be removed influences the number of coils per phase per segment and whether all the segments are identical. In this research, m coils are removed per segments for a m-phase machine, so that all the phases in one segment have the same number of coils. Note if there are too many segments, this segmentation theme will lead to low equivalent coil fill factor because of the space unused.

This segmentation theme demands that the total number of coils before segmentation (Q_0), number of phases (m), and number of segments (n_s) should satisfy

$$Q_0 = kmn_s, \tag{4.1}$$

where k is integer. This implies

- The total number of coils should be divisible by the number of phases and the number of segments.

- If k is an even number, all the segments are identical after segmentation (example at lower right of Figure 4.2).

- If k is an odd number, two types of segments are generated after segmentation (example at upper right of Figure 4.2).

The total number of coils after segmentation (Q_1) is

$$Q_1 = (k-1)mn_s. \tag{4.2}$$

63

4.2.5 Coordinate system and field calculation

The cylindrical coordinate system is used in the analysis of iPMG. For AF machines, the windings are placed in $r\theta$ plane, whereas for RF machines, the windings are placed perpendicular to $r\theta$ plane, i.e., parallel to z-axis (Figure 4.3).
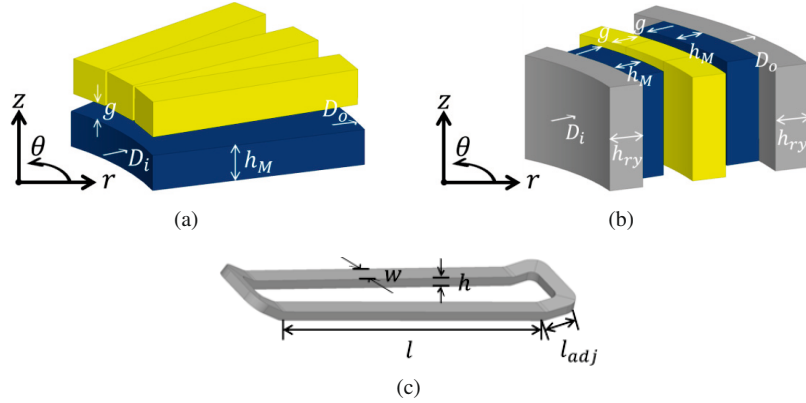
Figure 4.3: Coordinate system and machine geometry variables: (a) AF machines (1R-HA-AFPMG for example); (b) RF machines (2R-CA-RFPMG for example); (c) coil dimension.

A key parameter for the design of electrical machines is the fundamental flux density in the air gap (B_{p1}). For iPMGs, the winding region occupies a significant area, and it is desired to obtain the average B_{p1} of the winding region for calculating the back-EMF accurately. In the 2D approach, there are two factors affecting the accurate calculation of the average B_{p1}, namely the field-calculation plane and the field-calculation layer.

In this research, B_{p1} is calculated in the 2D FEA (Figure 4.4). For RFPMG, it is assumed that there is no field variation along the shaft; therefore, any plane perpendicular to the shaft can be the field-calculation plane. For AFPMG (Figure 4.5), if the ratio of inner radius to outer radius, σ, is large, the field distribution does not vary much along the winding active length except the small parts close to the two ends of the winding; in case of small σ, the field presents non-linearity along the winding active length, and the average flux density is smaller than that at the average diameter $(D_i + D_o)/2$. To take into account this non-linearity, we select the field-calculation plane at the diameter D_a, which is given by

$$D_a = \sqrt{D_i D_o} \qquad \text{for AFPMG.} \tag{4.3}$$

In the field-calculation plane of iPMG, the field is unevenly distributed in the winding region (Figure 4.6). In 1R machine, B_{p1} is obtained by the Fourier analysis of the field in
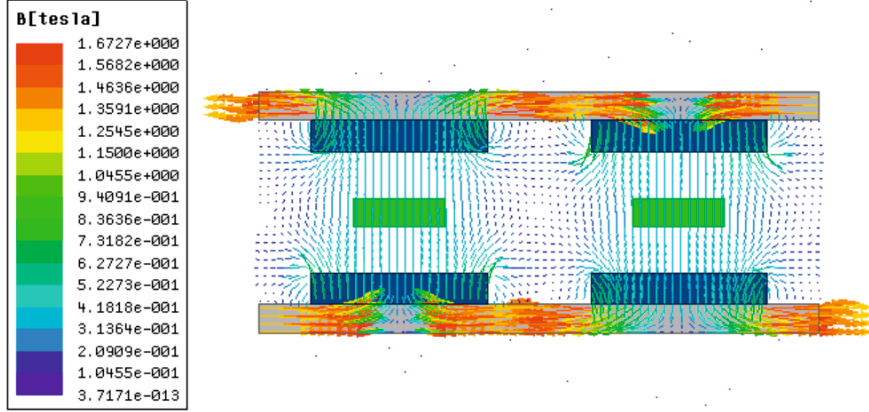
Figure 4.4: A 2D model of a iPMG and its field distribution.
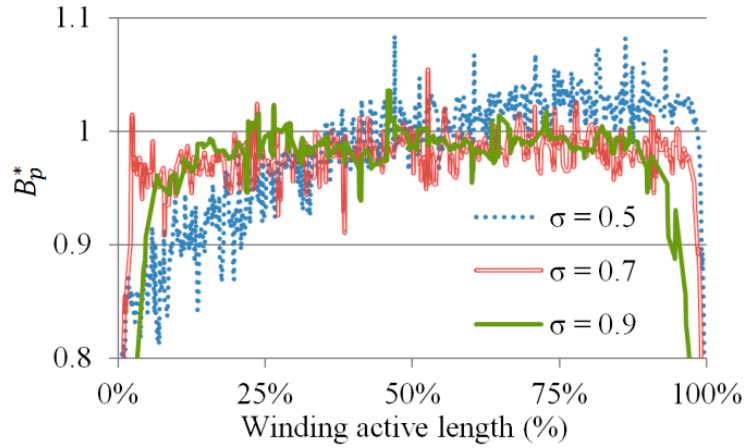
Figure 4.5: Field distribution along the active length of an AFPMG winding (B_p^* is the peak flux density in the air gap normalized to B_{p1}).

the middle layer of the winding region, *layer 1*, whereas in 2R machine, the average B_{p1} of the winding region will be underestimated if *layer 1* is still used, thus instead, *layer c* is selected as the field-calculation layer, and k_c is used to represent its position. In this research, *layer c* is selected at the middle of the winding surface and *layer 1*, therefore, k_c equals 0.25. In AF machine, *layer 1* is the middle line of the winding region; in RF machine, *layer 1* lies at the air gap diameter D_a, which is given by

$$D_a = (D_i + D_o)/2 \qquad \text{for RFPMG.} \tag{4.4}$$

65
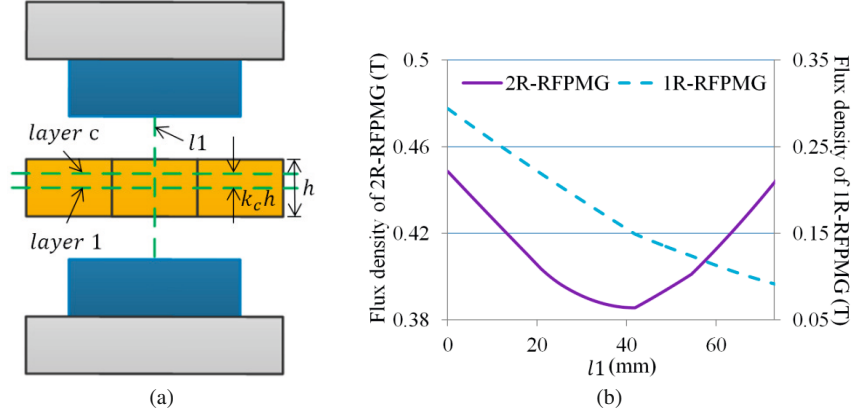
Figure 4.6: Selection of field-calculation layer: (a) Machine topology; (b) Example of the field distribution along line $l1$ for 1R/2R machine.

4.2.6 Flux leakage coefficient

In RFPMG, the air-gap field decreases dramatically when approaching the winding ends. This is due to the pole-to-pole leakage and pole to rotor yoke leakage. In AFPMG, same phenomenon happens in the inner end part; however, in the outer end part, the field may increase (Figure 4.5). Consider a one-turn full-pitch concentrated coil placed in an iron-less RFPMG, if the field does not vary along the coil active length, the ideal no-load peak voltage induced in this coil is

$$E_1 = \pi B_{p1} l w_M D_a. \tag{4.5}$$

Practically, the field varies along the coil active length, consequently, the practical induced voltage is

$$E_2 = \pi \int_0^l B_{p1}(z) w_M D_a dz. \tag{4.6}$$

The difference of E_1 and E_2 is expressed with a leakage coefficient k_{le} given by

$$k_{le} = \frac{E_2}{E_1} = \frac{\int_0^l B_{p1}(z) dz}{B_{p1} l}. \tag{4.7}$$

Similarly, k_{le} for AF machine is given by

$$k_{le} = \frac{2\pi \int_{r_i}^{r_o} B_{p1}(r) w_M r dr}{2\pi B_{p1} l w_M r_a} = \frac{\int_{r_i}^{r_o} B_{p1}(r) r dr}{B_{p1} l r_a}. \tag{4.8}$$

k_{le} is calculated in the postprocessing of the 3D SFEA, and used to correct the back-EMF obtained with 2D SFEA.

4.3 Modelling and optimization methods

The specification of the studied machine is shown in Table 4.1.

Table 4.1: Generator specification.

Parameters	Types	Value
Rated power, MW	*Constant*	10
Number of phases (m)	*Constant*	3
Rated speed (n_N), rpm	*Constant*	12
Rated voltage, kV	*Constant*	6.8
Number of stator segments (n_s)	*Constant*	9
Number of parallel branches (a)	*Constant*	1
Coil fill factor (k_f)	*Constant*	0.5
PM(N42SH) B_r at operating temperature, T	*Constant*	1.2
Permeability of PM	*Constant*	1.05
PM specific cost, €/kg	*Constant*	80
Iron (solid steel) specific cost, €/kg	*Constant*	16
Copper specific cost, €/kg	*Constant*	27
Outer diameter (D_o), m	*Free variable*	10-30
Pole number (p)	*Free variable*	90-720
Ratio of PM width to pole pitch (k_M)	*Free variable*	0.1-0.8
Fundamental flux density in air gap (B_{p1}), T	*Free variable*	0.1-0.8
Outer diameter (D_o), m	*Free variable*	10-30
Current density (J), A/mm^2	*Free variable*	2-5
Thickness of the air gap (g), mm	*Constraint*	0.15%D_o
Thickness of the PM (h_M), mm	*Constraint*	5-100
Thickness of the rotor yoke (h_{ry}), mm	*Constraint*	5-100
Max. flux density in rotor yoke (B_{ry}^{ref}), T	*Constraint*	1.7
Max. electric load (E_L), A/mm	*Constraint*	50

The following assumptions are made in modelling:

- The load power factor is one and load current is sinusoidal. Under such assumption, the load (full-scale converter) does not inject reactive power to the generator. This assumption provides a relatively fair base for comparing different designs because the generator reactance does not affect the converter cost.

- Because wind turbine shares the supporting structures with iPMG as aforementioned, without the knowledge of the whole turbine design, it is difficult to calculate the increased structure mass caused only by iPMG. Whereas the turbine design is out of the scope of this study, therefore, the inactive mass is not considered.

- Winding cooling is taken into account with constraints on the max. current density (J) and max. electric load (E_L); thermal analysis is out of the scope of this study, therefore, not considered.

The design procedure is illustrated in Figure 4.7. For individual design case, the stator coil dimension is determined first; then the PM thickness (h_M) and rotor yoke thickness (h_{ry}) are calculated in the 2D SFEA. After the machine dimension is determined, a 3D SFEA (Figure 4.8) is conducted to calculate the inductance, voltage drop ratio (κ, the loss of voltage magnitude from no load to rated load, normalized to rated voltage), and k_{le}. Afterwards, the initial values of κ and k_{le} are compared to their calculated values and updated. Finally, the machine weight, cost and efficiency are calculated. This design procedure is driven by a GA optimization program, which initializes GA, generates new populations based on the calculation results of the fitness function, and decides if the stopping criterion is met.

This design procedure is different with the one presented in the previous chapter. One key reason for making this change is to reduce the number of free variables and take advantage of the commercial code (Maxwell 2D and 3D). B_{p1} is used as the free variables rather than h_M, because it is relatively easier to estimate the range of the air gap flux density. h_{ry} is not used as the free variables, because an optimization algorithm provided by Maxwell is employed for calculating the minimal h_{ry} according to the max. rotor yoke flux density.

4.3.1 Stator sizing

The rated back-EMF (E_N, RMS) is determined by the rated voltage drop ratio and the rated phase voltage (U_{ph}, RMS).

$$E_N = (1 + \kappa)U_{ph}. \tag{4.9}$$

The active length of the coil is given by

$$l = \frac{E_N}{1.11 k_{w1} k_{le} w_M N_1 B_{p1} D_a}. \tag{4.10}$$

Here, the number of serial-connected turns per phase (N_1) is given by

$$N_1 = \frac{N_s Q_1}{ma}. \tag{4.11}$$

The segmentation reduces the loading capacity of iPMG with a factor given by

$$k_{cap} = 1 - \frac{1}{q p_s}. \tag{4.12}$$
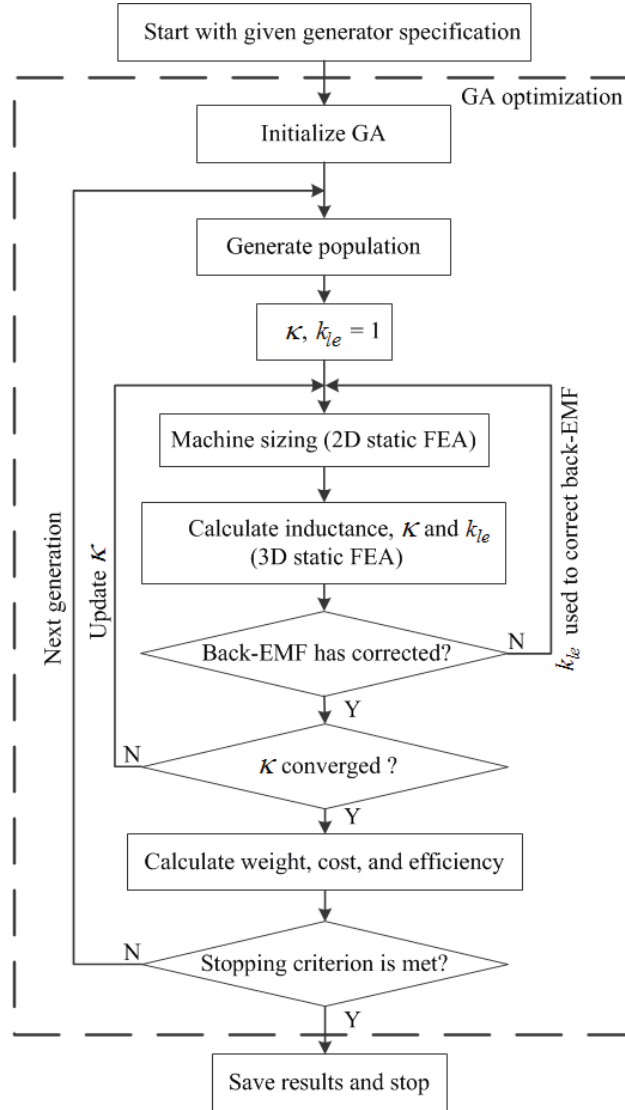
Figure 4.7: Design procedure.

The number of turns per coil (N_s) is calculated according to the allowed electric load in the machine with specified cooling. In the studied winding, the electric load is given by

$$E_L = \frac{2pqmN_sI_{ph_s}k_{cap}}{\pi aD_a}.$$ (4.13)

Winding factor is the product of the distribution factor and the pitch factor. Full-pitch
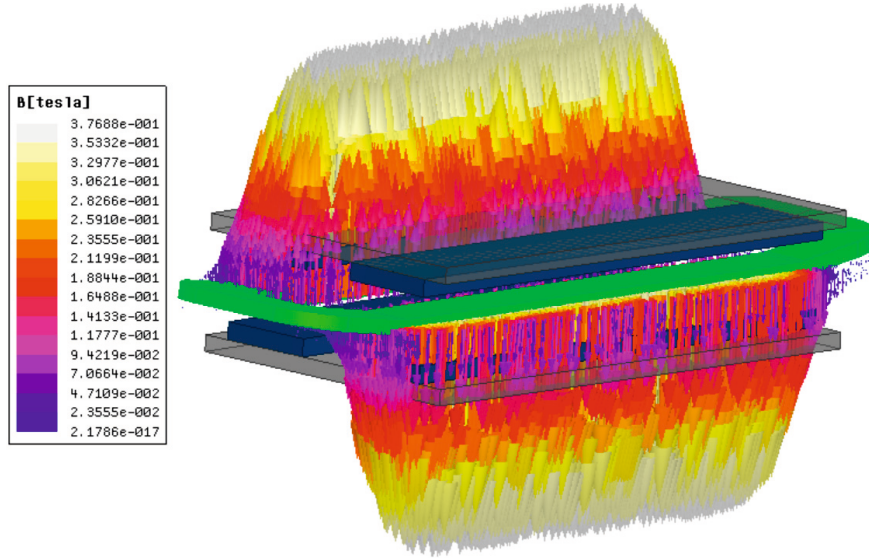
Figure 4.8: A 3D iPMG model and the plot of air gap B_z.

concentrated winding is used in the studied winding; therefore, the pitch factor is one. The distribution factor (k_{d1}) is calculated with the approach developed for single-set non-overlap winding [19]. In RF machines, each coil side spreads $60°$ phase belt, thus the distribution factor is constant ($3/\pi = 0.955$). In AF machines, because the winding cross section is fixed, the distribution factor varies radially. Neglect the coil bending ($l_{adj} \ll r_i$ in large-diameter machines) and consider a small part of the winding, the distribution factor of this small part is given by

$$k_{d1} = \frac{\sin \frac{\pi\sigma}{2m(\sigma - l_p\sigma + l_p)}}{\frac{\pi\sigma}{2m(\sigma - l_p\sigma + l_p)}}, \tag{4.14}$$

where l_p is the distance of this small part to the winding inner radius and normalized to the winding active length. The distribution factors of all these small parts along the winding are plotted in Figure 4.9. It shows that, in AF machines, the winding parts at different position along the winding have different contribution to the torque production, and the non-linearity of this radial dependency is dependent on σ. Generally, AF machines have higher equivalent distribution factor than RF machines if the same aforementioned winding is used.

In AF machines, the coil width (w) is limited by the machine inner radius and the winding bending, whereas in RF machines, w is limited by D_a (4.15).

$$w = \begin{cases} \frac{2\pi(r_i - ladj)}{pm} & \text{for AFPMG} \\ \frac{\pi D_a}{pm} & \text{for RFPMG} \end{cases} \tag{4.15}$$

70
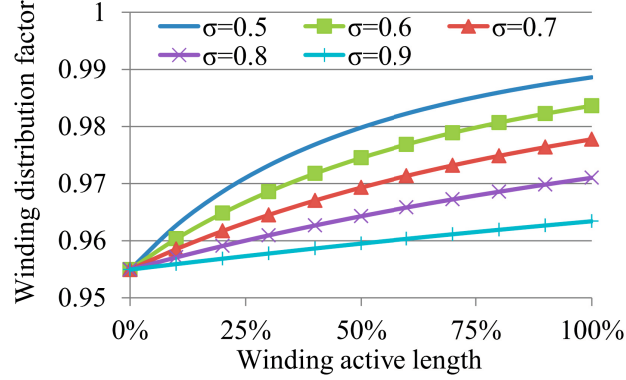
Figure 4.9: Winding distribution factor for AF machines.

Then the coil thickness (h) is given by

$$h = \frac{I_{ph\_s}N_s}{Jak_f w}. \tag{4.16}$$

The averaged half-length of total end coils (l_e) is given by

$$l_e = \frac{\pi D_a}{p} + 2l_{adj} - w. \tag{4.17}$$

4.3.2 Rotor sizing

For CA machines, the magnet pole is modelled with a radially magnetized PM block. For HA machines, four PM blocks are used to model one pole pair. HA machines are essentially self-shielding and do not require rotor back iron [106]. It is possible to enhance the air gap field with more blocks in one pole pair; however, this is not considered because of the more complicated rotor structure.

As shown in Figure 4.10, h_{ry} and h_M are calculated with no load 2D SFEA. For CA machines, h_{ry} is calculated according to the reference flux density (B_{ry}^{ref}) and h_M. An optimizer based on Quasi-Newton method is used to find the minimal h_{ry}. Once h_{ry} is obtained, the corresponding B_{p1} is compared to the reference air gap flux density (B_{p1}^{ref}). If B_{p1}^{ref} is reached, h_M is recorded. Otherwise, h_M is updated with (4.18), and the calculations of h_{ry} and h_M are iterated. For HA machines, only h_M is unknown, and the same method (4.18) is applied.

$$h_M^{j+1} = h_M^j(2 - \frac{B_{ry}^j}{B_{ry}^{ref}}). \tag{4.18}$$
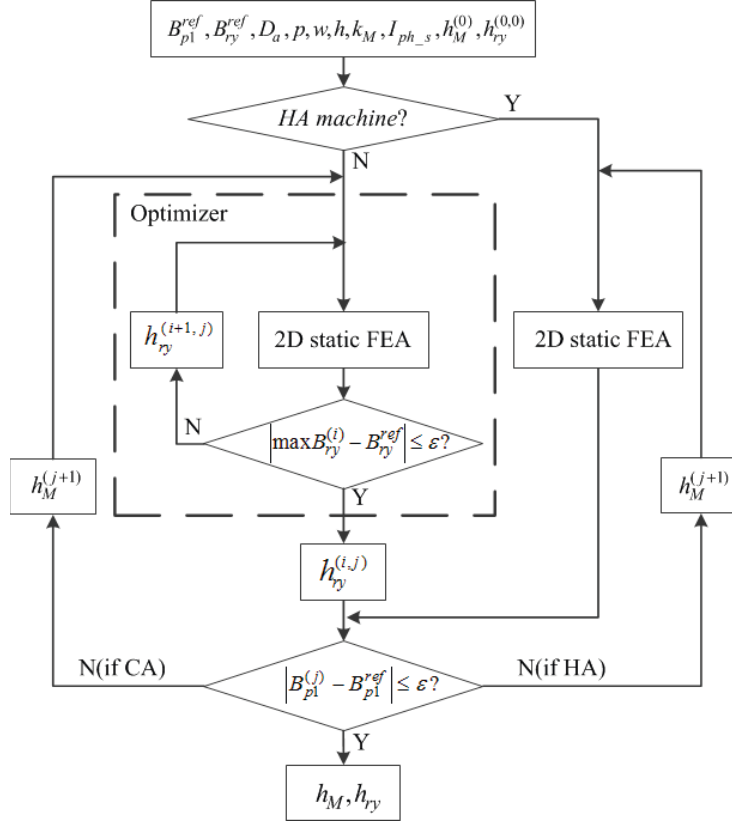
Figure 4.10: Rotor sizing.

4.3.3 Inductance and resistance

The phase synchronous inductance (L_s) is given by

$$L_s = L - M, \tag{4.19}$$

where the phase self-inductance (L) is calculated by assigning DC current (RMS value at rated load) to one phase winding and calculating the relevant flux linkage with 3D SFEA. The permeability of the mesh elements is frozen in the calculation to take into account the saturation. The influences of rotor position, proximity effect, and skin effect are neglected.

The mutual flux linkage is calculated simply by integrating the flux density over the winding overlapping region. This gives the mutual inductance (M) $-L/4$. Because of the stator segmentation, the winding layout is not exactly the same for all the phases within each segment. This makes the phase-to-phase mutual inductances different. Theoretically,

72

this difference becomes quite small as long as the number of coils in each segment is large. In this research, the phase-to-phase mutual inductances are assumed to be the same.

The winding resistance depends on the coil size, operating temperature, frequency, and the influences of skin effect and proximity effect. Heavily twisted Litz wires are used to minimize the eddy current loss at the downside of low coil fill factor. The winding conductivity is adjusted to the predefined operating temperature. AC resistance ratio is used to represent the influences of skin effect and proximity effect, and the AC resistance ratio for the fundamental harmonic (k_{r1}) is given by

$$k_{r1} = \frac{R_{AC}(t)}{R_{DC}(t)}. \tag{4.20}$$

In ironless machines, k_{r1} of Litz wires behaves less frequency-sensitive compared to the iron-cored machines (Figure 4.11). In practical calculation, k_{r1} is taken one.
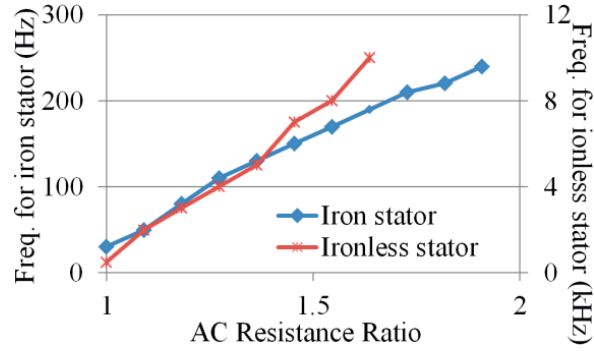
Figure 4.11: AC resistance ratio of Litz wires (20*Φ1 mm) placed in iron stator and ironless stator.

4.3.4 Losses

The total losses consist of winding loss, eddy current loss in PM, iron loss in rotor yoke, rotational loss, and bearing loss. There are two components in winding loss: copper loss and eddy current loss induced by the rotating magnetic field. Because Litz wires are used, the eddy current loss resulted from the rotor rotation is neglected. Copper loss (P_{cu}) at rated load is given by

$$P_{cu} = n_s I_{ph\_s}^2 R_{AC}. \tag{4.21}$$

Eddy current loss in PM (P_M) is given by

$$P_M = p_M n_r p V_M, \tag{4.22}$$

where the specific loss density (p_M) is taken 1 kW/m^3 at rated load, n_r is the number of rotors, and V_M is the PM volume per pole. 3D TFEA shows the iron loss in rotor yoke is very low thus ignored.

Rotational loss and bearing loss in large-diameter iPMGs vary with the structural designs; therefore it is hard to approximate these losses with general approaches. Intuitively, compared to conventional machines, rotational loss in large-diameter iPMGs will increase with the likely adoption of spoke wheel structures, whereas the bearing loss may decrease because of the low machine mass. In this research, the assumption for rotational loss and bearing loss in the conventional MW and multi-MW machines at rated load applies, i.e., these losses are 0.5% of the rated power [63], [104].

4.3.5 Optimization

Machine optimization requires handling multidimensional problems. GA is widely used [107] in electrical machine optimization and has the low possibility of trapping in local minima [108]. In this research, the design targets are the highest torque density (rated torque divided by the active mass) and the highest efficiency at rated load. Design constants, free variables, and constraints are given in Table 4.1. The material specific costs, in particular for the PM, fluctuate dramatically with the changes in the market; therefore, the power cost (cost of active mass divided by the rated power) is calculated only for information.

4.4 Optimal machines at D_o = 20 m

In this section, the performances of the optimal machines in terms of the highest torque density and the highest efficiency at fixed outer diameter (20 m) are investigated and compared.

4.4.1 Optimal machines (highest torque density at D_o = 20 m)

As shown in Table 4.2, 2R/HA/RF machines have higher torque density than the corresponding 1R/CA/AF machines. All the machines have the torque density no less than 108 Nm/kg. The torque density of the worst machine, one-rotor conventional-array AFPMG (1R-CA-AFPMG), is less than half of the torque density of the best machine, two-rotor halbach-array RFPMG (2R-HA-RFPMG), which emphasizes the importance of selecting the right machine type.

Table 4.2: Optimal designs (highest torque density at diameter 20 m).

Machines	k_M	B_{p1} (T)	p	Torque density (Nm/kg)	Efficiency	Power cost (€/W)
1R-CA-RFPMG	0.38	0.20	234	155	94.0%	0.22
1R-CA-AFPMG	0.60	0.26	252	108	94.0%	0.31
1R-HA-RFPMG	1.00	0.34	324	225	94.6%	0.24
1R-HA-AFPMG	1.00	0.30	288	169	94.5%	0.33
2R-CA-RFPMG	0.58	0.35	324	184	95.4%	0.16
2R-CA-AFPMG	0.62	0.37	306	175	95.3%	0.18
2R-HA-RFPMG	1.00	0.36	450	242	95.3%	0.22
2R-HA-AFPMG	1.00	0.43	396	221	95.7%	0.25

In addition, 2R machines have higher B_{p1}, more poles, and lower power cost than the corresponding 1R machines. The efficiency of 2R machines is generally 1% higher than that of 1R machines. HA machines have higher B_{p1}, more poles, higher power cost than the corresponding CA machines. RF machines are less expensive than AF machines. All the machines have the current density above 4.4 A/mm^2, the efficiency no more than 95.7%, and the power cost no more than 0.33 €/W.

4.4.2 Optimal machines (highest efficiency at D_o = 20 m)

As shown in Table 4.3, 2R machines normally have higher efficiency than 1R machines. However, it is hard to compare HA machines with CA machines and RF machines with AF machines in term of efficiency. All the machines have the efficiency no less than 96.7%. In addition, B_{p1} for 2R machines is at least 0.3 T higher than that for 1R machines. HA machines have higher B_{p1}, much higher torque density, and more power cost than CA machines. RF machines are cheaper than AF machines except 2R-CA machines. All the machines have the current density no more than 2.71 A/mm^2, the torque density no more than 133 Nm/kg, and the power cost no less than 0.34 €/W.

4.4.3 Summary of the calculation results

At outer diameter 20 m, following conclusions are drawn:

- 2R machines are better than 1R machines in the above two cases. This is due to the lower magnetic reluctance in the main flux path of the 2R machines and thus better utilization of the PM material.

- CA machines generally have lower torque density and lower power cost than HA

Table 4.3: Optimal designs (highest efficiency at diameter 20 m).

Machines	k_M	B_{p1} (T)	p	Torque density (Nm/kg)	Efficiency	Power cost (€/W)
1R-CA-RFPMG	0.72	0.32	252	98	97.1%	0.39
1R-CA-AFPMG	0.49	0.23	126	68	96.7%	0.47
1R-HA-RFPMG	1.00	0.36	324	133	96.8%	0.40
1R-HA-AFPMG	1.00	0.33	270	106	97.2%	0.49
2R-CA-RFPMG	0.78	0.62	270	80	97.6%	0.41
2R-CA-AFPMG	0.51	0.58	126	88	97.8%	0.34
2R-HA-RFPMG	1.00	0.75	198	130	97.8%	0.42
2R-HA-AFPMG	1.00	0.74	162	118	97.9%	0.47

machines. The high cost of HA machines is due to much consumption of PM material.

- RF machines are generally lighter (higher torque density) and cheaper (lower power cost) than AF machines.

- Lightweight PM machines are normally cheap, and do not offer high efficiency. High efficiency machines are normally heavy and expensive.

- 2R-CA-AFPMG and two-rotor conventional-array RFPMG (2R-CA-RFPMG) are recommended as the optimal machines because of high torque density, high efficiency, and low power cost.

4.5 Optimal machines at D_o between 10 m and 30 m

In this section, the performances of 2R-CA-AFPMG and 2R-CA-RFPMG at different outer diameters are investigated and compared. Note the first feasible AF machine that meets the design specification (Table 4.1) appears at 15 m when D_o grows with a step of 5 m.

4.5.1 Optimal machines (highest torque density)

As shown in Figure 4.12(a), both machines have higher torque density at larger outer diameter. When D_o is greater than 25 m, both machines start to follow the same curve of torque density, whereas at small D_o, the torque density of AF machine is more diameter-dependent than that of RF machine.

Figure 4.12: Performance of the optimal machines in term of highest torque density. (*Continued.*)

In addition, AF machine generally has higher efficiency and higher power cost than RF machine, as shown in Figure 4.12(b) and (c).

The other parameters are given in Figure 4.12(d)-(j). k_M for RF machine varies around 0.6, whereas k_M for AF machine decreases all the way. Note that the pole number for AF machine grows faster than that for RF machine. AF machine is sensitive to large pole number because of the pole-to-pole leakage at its inner radius, and consequently k_M for AF machine will have to decrease. At large D_o, both machines have low B_{p1} (around 0.3 T), though B_{p1} for AF machine is higher than that for RF machine. It seems that high

Figure 4.12: Performance of the optimal machines in term of highest torque density.

torque density design prioritizes a high current density rather than a high B_{p1}, because both machines have the current density above 4.3 A/mm^2.

The aspect ratio is defined as machine length in z-axis divided by the machine outer diameter in $r\theta$ plane, regardless of the machine types. For RF machine, the aspect ratio varies significantly as D_o grows. This is because at the same power rating, the RF machine with the smaller diameter has the longer length, thus larger aspect ratio. In case of AF machine, the aspect ratio keeps at low level and does not vary much. Furthermore, the aspect ratio of iPMGs at large diameter is much smaller than that of small machines [19], [109]. Voltage drop ratio (κ) reflects mainly the influence of voltage drop across the reactance. In CA machine where the saturation does not influence the reactance very much, the higher κ implies more consumption of copper and thus lower efficiency. κ for RF machine is more diameter-dependent than that for AF machine. σ for AF machine is higher than that for small machines [109] and keeps increasing as the diameter grows.

4.5.2 Optimal machines (highest efficiency)

As shown in Figure 4.13(a), the efficiencies of both machines do not vary much, though keep at high level. AF machine shows higher efficiency than RF machine, however, the

difference is not significant.

In addition, if the diameter is greater than approximate 18 m, AF machine has higher torque density and lower power cost than RF machine, as shown in Figure 4.13(b) and (c). The other parameters are given in Figure 4.13(d)-(j). Though having the similar curve of pole number as that for AF machine, RF machine has larger k_M and higher flux density, which makes it more expensive. RF machine has slightly higher current density and slightly lower voltage drop ratio than those for AF machine. This can explain why both machines have similar efficiency. The aspect ratio for AF machine keeps at low level, whereas for RF machine, the aspect ratio decreases dramatically as D_o grows. for AF machine shows the same trend as that in the previous case.

4.5.3 Summary of the calculation results

Following general conclusions are drawn:

- As the outer diameter grows, generator torque density increases; generator efficiency does not vary much.

- At small diameter (< 25 m), compared to optimal RF machine, optimal AF machine is heavier. The difference in efficiency is not significant.

- At large diameter (≥ 25 m), the differences of optimal AF machine and RF machine become insignificant. As the aspect ratios for both machines decrease, and σ for AF machine increases, the shapes of these two machines become like the rings.

- The comparison between the above two analyses shows that 100% more mass and cost are required roughly to gain additional 2% in efficiency. The main loss for ironless machines is the copper loss. With high air-gap flux density and low current density, the copper loss can be reduced significantly. However, more copper and PM material have to be used, and the power cost will have to increase. Therefore, high efficiency machines are normally heavy and expensive.

- For AF machine, the torque density, power cost, k_M, pole number, and are more sensitive to the variation of outer diameter; for RF machine, the efficiency, air-gap flux density, aspect ratio, and voltage drop ratio are more sensitive to the variation of the outer diameter. Because of this diameter-dependency, it may be not proper to apply the previous knowledge on the recommended values for key parameters, which is based on the optimization of small machines.

- Note that the optimizations presented in Section 4.4 and 4.5 have multiple free variables, and the optimization objective is either torque density or efficiency. However,
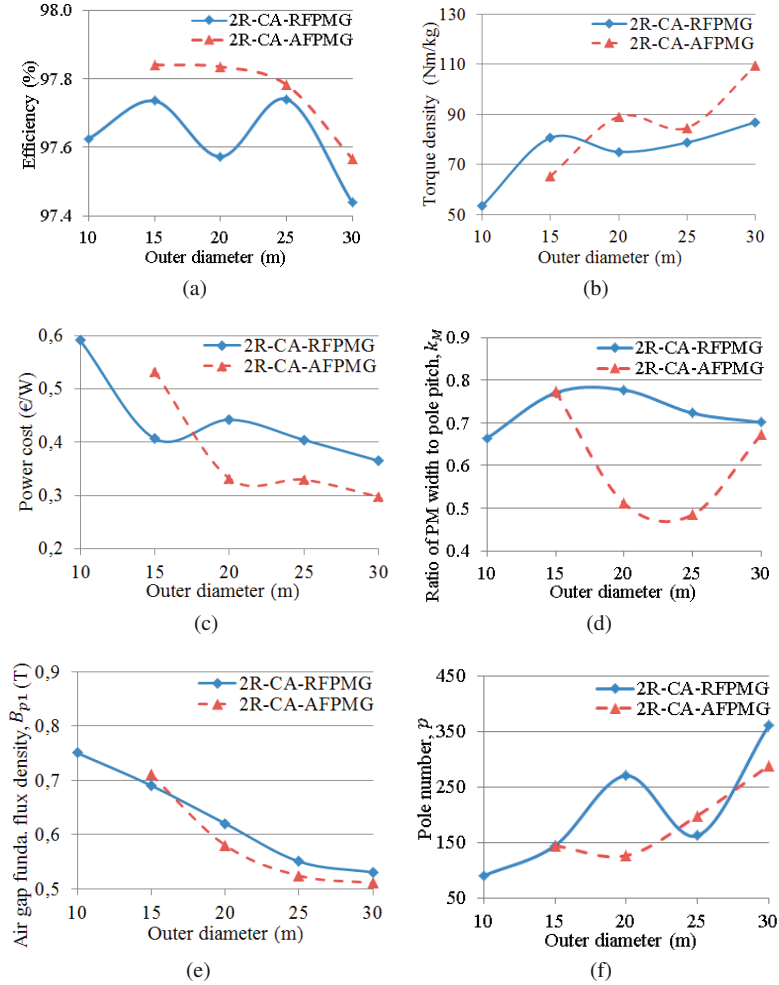
Figure 4.13: Performance of the optimal machines in term of highest efficiency. (*Continued.*)

in practical engineering, there will be multiple objectives and the weight of individual objective varies, therefore, the corresponding optimization result will be different.

- In these multi-dimensional optimization, there are many designs that fulfil the definition of "optimal designs", and the optimization algorithm only picks up one of them. This implies that, when the parameters of these optimal designs are plotted as functions of the outer diameter, the curve for one specific parameter does not need to have uniform upward/downward/straight trend, i.e., have a constant curve gradient. There can be variations, such as the k_M in Figure 4.12d and the pole number in
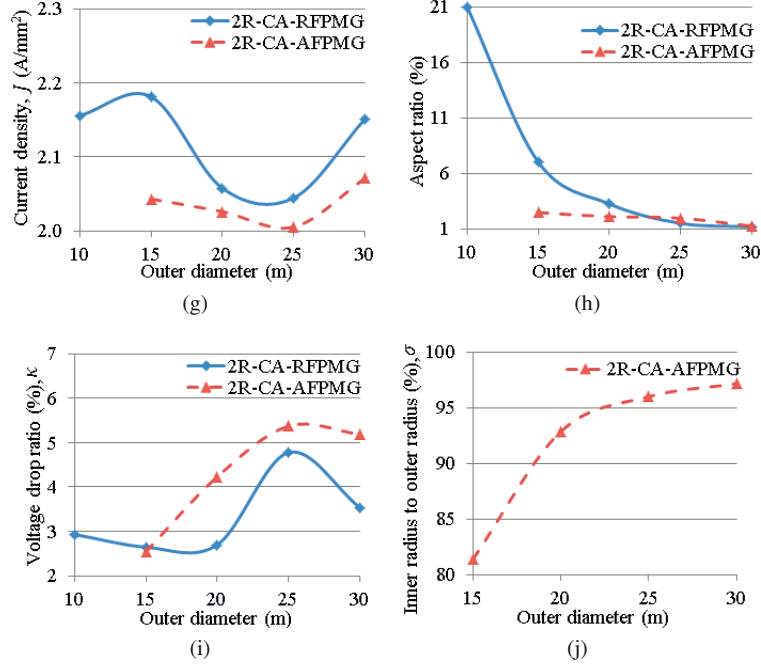
Figure 4.13: Performance of the optimal machines in term of highest efficiency.

Figure 4.13f.

- Note that some of the optimal designs in Section 4.4 and 4.5 have k_M less than 0.6 (even 0.5), which is never found in literature. This can be explained with the selection of the free variables. In this research, k_M and B_{p1} are selected as the free variables defining PM dimensions rather than k_M and h_M, and the boundaries for these two parameters are set to 0.1-0.8, rather than 0.6-0.9 for k_M and 0.4-1.0 B_{p1} (which are common in literature). These settings give the optimization algorithm a larger variable space to search for the optimal machine.

4.6 Method validation

It is expensive to build a downscale iPMG that can show the main design features. Therefore, limited tests were conducted on an existing prototype (Appendix D) to validate the key parts (proposals and methods for field and inductance calculations) of this design strategy. The GA effectiveness was validated by comparing GA results with the results of parametric study.

4.6.1 Validation of field and inductance calculations

The back-EMF (reflecting the calculation of B_{p1} and k_{le}) and the inductance were calculated. Calculation results agree well with the measurement as shown in Table 4.4. Note that rotor yokes of this prototype have negligible saturation (1.47 T); therefore, it makes sense to use RLC meter to measure the inductance.

The calculation of the efficiency is not validated because it is the cheaper rectangular wires rather than Litz wires used in this machine; this increases the copper loss and induces significant eddy current loss in the winding. Practically, in direct-driven iPMG, the calculation of the losses in Litz wires is not error-prone because of the nature of low frequency. Furthermore, bearing and rotational losses are dependent on bearing types and the machine structure as well; therefore, the measurement of these losses in small machines cannot be used to validate the calculation of machines with large diameter.

Table 4.4: Measured results vs. calculation results.

Parameters	Measured results	Calculated Results
Back-EMF at rated speed	82.3 V	81.9 V
Phase self-inductance	1.8 mH	1.76 mH

4.6.2 Validation of optimization method

Note that this previous-built prototype was designed mainly for demonstrating the iPMG concept, thus not fully optimized. Therefore, it is not suitable for validating the employed optimization method.

The validation of the optimization method is conducted by comparing optimization results to the results of parametric study. A small-scale problem is used for this test (Table 4.5 and 4.6). The objective is to find out the optimal 2R-CA-AFPMG that gives the highest torque density at fixed outer diameter and current density. The optimization case was run at a workstation (Appendix C). For parametric study, four such workstations were used. Note the calculation time for the parametric study in Table 4.6 is obtained by summing the calculation time of the four workstations.

Compared to parametric study, the optimization method employed can significantly reduce the calculation time while grasping the global optimum, though this is a reduced problem.

Table 4.5: Optimization results.

Parameters	Settings	Results
Outer diameter (D_o), m	30	-
Current density (J), A/mm^2	5	-
Pole number (p)	90-720	522
Ratio of PM width to pole pitch (k_M)	0.1-0.8	0.54
1st order flux density in air gap (B_{p1}), T	0.1-0.8	0.31
Torque density, Nm/kg	-	209
Populations per generation	40	-
Total generation	5	-
Calculation (clock) time, hours	-	28.7

Table 4.6: Parametric study results.

Parameters	Settings	Results
Outer diameter (D_o), m	30	-
Current density (J), A/mm^2	5	-
Pole number (p)	step: 90; range: 90-720	540
Ratio of PM width to pole pitch (k_M)	step: 0.05; range: 0.1-0.8	0.55
1st order flux density in air gap (B_{p1}), T	step: 0.1; range: 0.1-0.8	0.30
Torque density, Nm/kg	-	203
Total calculation cases	960	-
Total calculation (clock) time, hours	-	92.5

4.7   Inactive and total weights of iPMG

Conventionally, the inactive part of a generator includes the main frame, supporting structures of the stator and the rotor, shaft, bearing, and cooling systems. However, when it comes to iPMGs, the number of inactive parts can be less.

For instance, if an iPMG is integrated into the wind turbine with a solution like in Figure 4.14, then the iPMG will share the main shaft and bearing with the whole turbine, and the material for the generator main frame will be reduced, the inactive weight of this iPMG will be therefore less than that of the conventional case.

Ref. [3] reported a method for estimating the inactive weight of iPMG for the 2,3, and 5 MW. Unfortunately, the developed method is only for low-power (max. 5 MW) and small-diameter (max. 10.4 m) machines, thus not applicable for the discussion here. To estimate the inactive mass of iPMG, the design data for a 6 MW large-diameter iPMG [111] are used and scaled to 10 MW. The scaling is conducted by fixing the power density (68.97 W/kg, total power divided by the total weight).

Table 4.7 summarises the data of the scaled 10 MW iPMG and a 10 MW iron-cored PMG. The data for the active part of the iPMG correspond to the optimal 2R-CA-AFPMG

Figure 4.14: An example of integration design [110].

Table 4.7: iPMG vs. iron-cored PMG.

Parameters	Scaled iPMG	Iron-cored PMG
Power (MW)	10	10
Speed (rpm)	12	12
Diameter (m)	20	9.9
PM weight (ton)	15.30	6.56
Copper weight (ton)	7.54	15.78
Total iron weight (ton)	22.96	41.46
Total active weight (ton)	45.8	75.4
Total active cost (M€)	1.81	1.61
Total inactive weight (ton)	99.2	206.6
Total inactive cost (M€)	1.59	3.31
Total weight (ton)	145	282
Total cost (M€)	3.40	4.92

in term of highest torque density at 20 m (Table 4.2). The data for the iron-cored PMG
are taken from Figure 3.2 and Table 3.4.

The comparison indicates that

- The iPMG active part is lighter and more expensive than that for iron-cored PMG.

- The weight and cost of the iPMG inactive part are approximately half of that for
  iron-cored PMG.

- The total weight of iPMG is approximately half of that for iron-cored PMG, and the total cost is only 69% of the iron-cored PMG cost.

- Using large-diameter iPMG brings significant weight and cost reduction for off-shore wind turbines.

4.8 Summary

In literature, iPMG has been reported as a promising solution to enable the lightweight offshore wind turbines. This study contributes presenting a systematic investigation on the possible iPMG designs. The findings provide useful guidelines for practical engineering as well as further academic research on the technology with respect to ironless machines.

At the investigated outer diameter (20 m), the comparative studies show that optimal solutions can be obtained with 2R-CA-PMGs. The investigation on the diameter-dependency indicates that at large diameter ($\geq$ 25 m), 2R-CA-AFPMG and 2R-CA-RFPMG start to follow the same torque density curve and similar efficiency curve. Whereas at small diameter ($<$ 25 m), RF machine has higher torque density than (and similar efficiency as) AF machine.

The optimization results show that the key parameters of large-diameter iPMG are sensitive to the variation of the outer diameter; therefore, previous knowledge from small machine optimization may not work.

The developed design approach employs FEA and GA to ensure the calculation accuracy and shorten the calculation time. Lab tests on a 23-kW ironless 2R-CA-AFPMG validate the proposals and methods of the field and inductance calculations, which are the key parts of this design approach. The comparison with the results of parametric study demonstrates the excellent performance of the GA used.

The comparison between the iPMG and the iron-cored PMG shows that using the large-diameter iPMG can bring significant weight and cost reduction to offshore wind turbine. Therefore, the iPMG technology is promising and attractive for the offshore wind power application.

Chapter 5

Multi-stage iPMGs

This chapter presents the design and performance investigation of the ironless MS-AFPMGs. Section 5.1 discusses the two possible topologies of ironless MS-AFPMGs; Section 5.2 presents the three types of ironless MS-AFPMGs investigated; an upgraded modelling and optimization method is given in Section 5.3, and the optimial designs are presented in Section 5.4; Section 5.5 concludes this chapter.

5.1   Introduction

It is known from the previous chapter that large-diameter iPMGs are characterized by the lightweight supporting structures. However, as the outer diameter goes large, the challenges in structural design arise, and the machine reliability may be reduced. In addition, the installation, operation, and maintenances for large-diameter structures are of the concerns. An alternative solution to the axial-flux version of the iPMGs is to reduce the outer diameter but have multiple stages in the axial direction, namely ironless MS-AFPMG.

Known with different names (multi-disc, multi-stack, multi-layered, etc.), MS-AFPMGs (mainly iron-cored machines) have been used in small-power applications where the machine radial dimension is constrained and high torque density is expected, e.g., unmanned aircraft drive [17], high-speed generating set [22], automobile [30], ship propulsion [112], plan landing gear [113], and small wind turbine [114]. Interests in MW and multi-MW ironless MS-AFPMGs for wind power application have emerged in the past half-decade [5], [115], because of low supporting structure weight, modularity, and fault tolerance.

Depending on the stator type (ironless or iron-cored) and the flux direction, MS-AFPMGs are designed with several different topologies [28]. For ironless MS-AFPMG, two typical topologies are normally used. The first type, shown in Figure 5.1(a), has

no rotor yokes inside the stack, and the permanent magnets are held in position by non-magnetic material. The main flux goes along PM-stator-...-stator-PM inside the stack, and turns into the adjacent poles through the rotor yokes lying at the two ends of the stack. Due to the absence of rotor yokes inside the stack, machine with this topology is expected to be lightweight. However, any failure in one of the rotors will deteriorate the performance of the whole machine and may stop the operation. In the second type, as depicted in Figure 5.1(b), all the stages have the same topology, and the flux is locked inside each stage. This topology has the advantage of fault tolerance and thus high availability, and the maintenance is also relatively easier. However, compared to the first type, the second type will be heavier and more expensive.

(a)

(b)
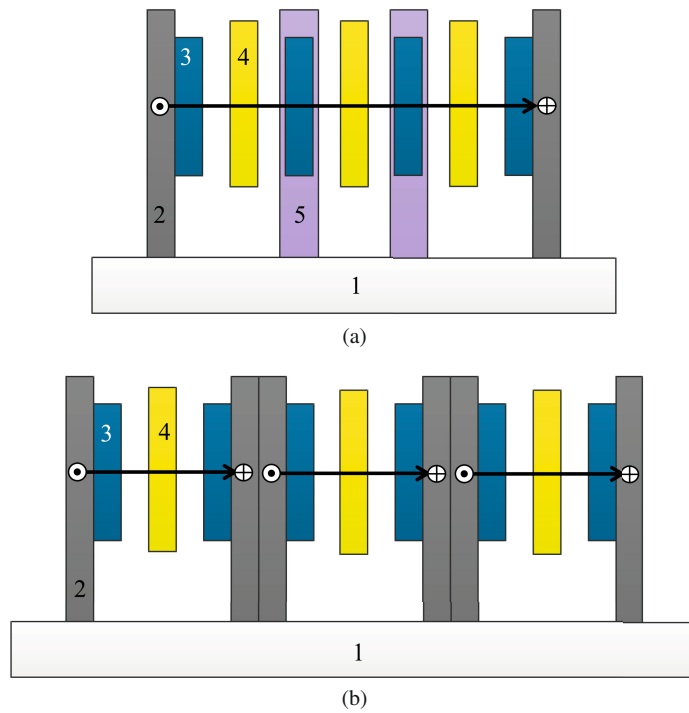
Figure 5.1: Two typical ironless MS-AFPMG topologies (1: shaft, 2: rotor yoke, 3: PM, 4: stator, 5: non-magnetic support).

So far, the papers on the high-power ironless MS-AFPMGs have mainly focused on presenting and validating the concept [5], [21], though there are a significant amount of papers discussing the design and optimization of ironless single-stage (1S) AFPMGs such as [25], [116], [117]. These previous findings and developed methods are important references but not enough for the research of high-power ironless MS-AFPMG. As it has been reported in [30], [94], the number of stages affects the choice of optimal iron-cored MS-AFPMG; furthermore, the output power of axial-flux machines is roughly proportional to the third power of the machine outer diameter [29]. Ironless MS-AFPMG will have more stages but smaller diameter than ironless 1S-AFPMG for the same rated power; therefore,

the outer diameter and the number of stages are two important parameters to determine the optimal ironless MS-AFPMG. Unfortunately, there are no complete papers on this topic so far, though [115] presents some investigations with incomplete description of the modelling and calculation results.

The design strategy presented in the previous chapter was successfully used in the optimization of 1S machines [116], and the lab tests confirmed its accuracy. However, it has the drawback of long calculation time. In this study, a form factor is introduced to improve the calculation efficiency, and this upgraded design strategy is used to investigate the effects of outer diameter and number of stages on the ironless MS-AFPMG performance.

5.2 Machine specification and types

The topology in Figure 5.1(b) is fault-tolerant and simple to assemble, thus selected as the machine type to be further investigated. It consists of several identical stages. Each stage (Figure 5.2) has two rotors and one ironless stator comprising coils casted in epoxy resin.
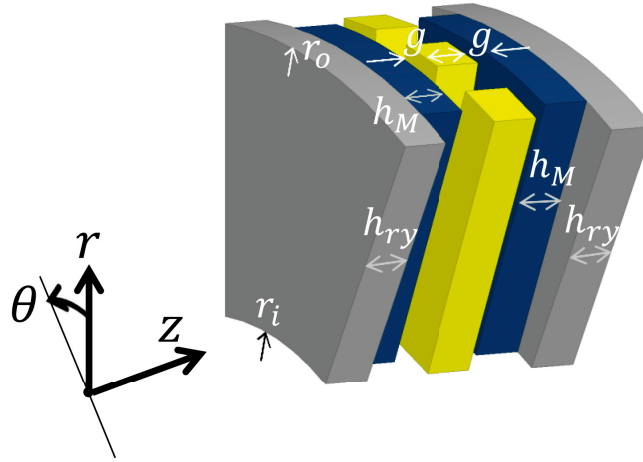
Figure 5.2: Machine dimension in cylindrical coordinate system (g is the air gap thickness, h_M is PM thickness, h_{ry} is rotor yoke thickness, r_i is inner radius, and r_o is outer radius. r, θ, and z are the axes of the cylindrical coordinate system).

The stator for each stage is segmented into physically separated parts, and each part carries the same power. Depending on the requirement to the degree of the fault tolerance, these segments can be connected to several generator-side converters. The total number of stator segments should be divisible by the number of generator-side converters. For

example, a three-stage generator can have three segments per stage; the total nine segments can be connected to 1/3/9 generator-side converters; in such a way, the generator is equivalent to 1/3/9 sub-machines.

The studied machine is a direct-driven three-phase 10 MW generator (Table 4.1). It has nine segments. The coil fill factor is low due to the use of heavily twisted Litz wires for minimizing the eddy current loss in the winding. The rotor iron loss is low in this low-speed machine; solid steel is therefore used in the rotor yoke.

Three types of generators are considered, namely

- One-stage AFPMG, nine segments.

- Two-stage (2S) AFPMG, nine segments per stage, nine segments from adjacent stages are connected parallelly to the same load, and therefore, the total number of segments is equivalent to nine.

- Three-stage (3S) AFPMG, three segments per stage.

5.3   Modelling method

This section presents the improvement of the design strategy given in the previous chapter, with the aim of reducing the calculation load and shortening calculation time.

Practically, it is impossible to perform the integration in (4.8) in the postprocessing of an SFEA, which does not contain the information about the harmonic components of the air gap field. A feasible way is to pick up evenly distributed lines in the air gap along the coil active length, then apply FFT to the field of each line, and finally sum up all the results. To ensure an accurate k_{le}, a large amount of FFTs are required in postprocessing, which is cumbersome and time-consuming. In addition, the calculation of k_{le} requires multiple iterations (mainly 3D SFEAs) for obtaining a converged k_{le}. The number of iterations affects the total calculation time, and depends on how close the initial guess of k_{le} is to its practical value. However, in a multidimensional optimization, it is not easy to give a good estimation of the initial value so that the number of iterations is as small as possible.

89

5.3.1 Form factor

To improve the calculation efficiency, it is necessary to investigate other methods. According to Faraday's law, the transient back-EMF is given by

$$e = N_1 \frac{d\phi}{dt} = N_1 \sum_{k=1}^{n} \Phi_{pk} \omega_k cos(\omega_k t + \varphi_k), \tag{5.1}$$

where ϕ is the transient flux penetrating a full-pitch coil, n is the total harmonics considered, Φ_{pk} is the peak value of the kth flux harmonic, ω_k is electrical angular velocity, and φ_k is phase angle.

To calculate the fundamental back-EMF, the corresponding Φ_{p1} is needed. Normally this requires multiple SFEAs or a TFEA to obtain the $\phi - t$ curve, then a FFT is conducted to extract Φ_{p1}. However, this process is also time-consuming.

In this study, a method is proposed to calculate Φ_{p1} with reduced calculation load and calculation time. Three calculation steps are needed.

Step 1: calculate the form factor k_{ff} at the field-calculation plan. k_{ff} is defined in (5.2). Its numerator calculates the flux (for an unit radial length) corresponding to the fundamental harmonic, and the denominator calculates the total flux (for an unit radial length). Therefore, the form factor, actually represents the percentage of fundamental flux in the total flux in the field-calculation plan. To get B_{p1}, one FFT operation is required to the field distribution along the field-calculation layer (Figure 4.6a).

$$k_{ff} = \frac{\int_{-\frac{\theta_p}{2}}^{\frac{\theta_p}{2}} B_{p1} cos(\frac{\pi}{\theta_p}\theta) r_a d\theta}{\int_{-\frac{\theta_p}{2}}^{\frac{\theta_p}{2}} B_z r_a d\theta} = \frac{\frac{2}{\pi} B_{p1} \theta_p}{\int_{-\frac{\theta_p}{2}}^{\frac{\theta_p}{2}} B_z d\theta}, \tag{5.2}$$

where θ_p is the pole pitch in radian.

Step 2: in a 3D SFEA, do a 2D field integration under one pole over the conductor plane cut by the field-calculation layer, which gives the maximal flux (Φ_p) penetrating the coil. The mathematical expression of this integration is

$$\Phi_p|_{(z=0.25h)} = \int_{r_i}^{r_o} \int_{-\frac{\theta_p}{2}}^{\frac{\theta_p}{2}} B_z r d\theta dr. \tag{5.3}$$

Step 3: assume all the planes (parallel to the field-calculation plane) along the coil active length have the same form factor in the air gap field, then the fundamental flux can be given by

$$\Phi_{p1} = k_{ff} \Phi_p|_{(z=0.25h)}. \tag{5.4}$$

5.3.2 Performance of the proposed method

The design procedure is illustrated in Figure 5.3. The machine sizing and parameter calculation are directly conducted in 2D and 3D SFEAs. Two iteration loops are used, one for voltage drop ratio κ (the magnitude difference of rated back-EMF and rated voltage), and another for k_{ff}. This method is driven by the GA of the Matlab optimization toolbox.
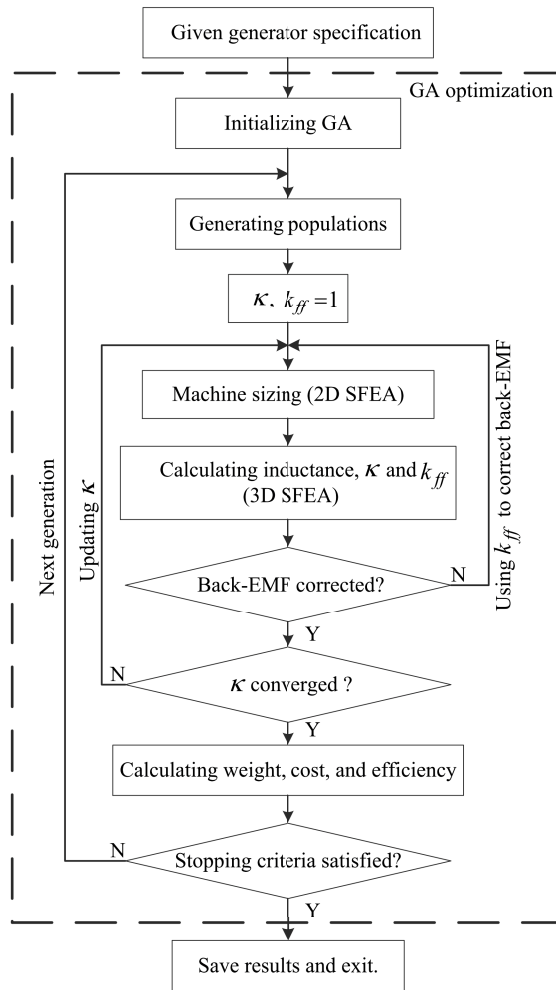
Figure 5.3: Design procedure (k_{ff} is form factor).

To investigate the performance of the upgraded method, a random design case is used. Its task is to dimension a generator that meets the specifications in Table 4.1, with the given input in the upper part of the Table 5.1.

The calculation results (lower part of the Table 5.1) show that both methods can dimension the generator properly, and their design results are close to each other. However, with the upgraded method, the numbers of 2D and 3D SFEAs conducted as well as the total calculation time are reduced.

Table 5.1: Method comparison.

	Parameters	**Upgraded method**	**Method in [116]**
Calculation input	Number of stages	3	
	D_o, m	10	
	k_M	0.73	
	B_{p1}, T	0.73	
	p	138	
	J, A/mm^2	2	
	Initial k_{ff} and k_{le}	k_{ff}=1	k_{le}=1
Calculation result	Aspect ratio	0.127	0.124
	σ	0.796	0.777
	Torque density, Nm/kg	37.06	35.60
	Efficiency (%)	96.9	96.9
	Power cost, €/W	0.89	0.93
	Calculated k_{ff} and k_{le}	k_{ff}=0.983	k_{le}=0.954
	Number of 2D SFEAs	271	378
	Number of 3D SFEAs	6	8
	Total calculation time, minutes	16.19	20.83

5.3.3   Population size

Table 4.1 and 5.1 show that one integer (pole number) is used as the free variable. For this mixed integer optimization problem with 5 free variables (except D_o), Matlab suggests the population size to be 50. This suggestion works fine, and normally after several generations, the fitness function will try to converge. However, at this moment, one may notice that, even though there is not much change in the value of the fitness function, the position (values of free variables) where the fitness function is obtained does vary a lot.

In this study, the interest is not just to investigate the optimal designs, but also the positions corresponding to the optimal designs. Therefore, having enough population is important for capturing the position correctly. In practical optimization, the population size is set to 100.

5.4 Optimization results

The proposed method is used to find the optimal designs in terms of highest torque density, highest efficiency, and multiple objectives. Note the first point on the left side of each curve (Figure 5.4 and Figure 5.5) shows the first feasible design as the outer diameter grows with a step of 2 m, and for each machine type, the optimal designs at five different diameters are investigated. Four workstations (Appendix C) were used, and it took at least two weeks to do all the calculations for one time.

5.4.1 Optimal machines (highest torque density)

As depicted in Figure 5.4(a), the torque density increases as the diameter grows, this meets the expectation that large-diameter machines normally produce more torque. At small diameters (lower than 16 m), the more number of stages, the higher torque density the machines have.

The other parameters are given in Figure 5.4(b)-(j). Machines with fewer number of stages present higher efficiency. As the diameter grows, the machine power cost decreases, and machines with fewer number of stages have higher power cost at low diameters. Above observations suggest that, in term of optimizing the torque density, it is better to build 1S machine at large diameter; if the outer diameter is constrained to a small value, MS solutions outperform the 1S solution while having lower efficiency and lower post cost.

k_M and B_{p1} decrease as the diameter grows, however, machines with fewer number of stages tend to have higher k_M and B_{p1}. Note that k_M is very low (e.g. lower than that in [118]). It is because this is a single-objective optimization and the GA tries to search the designs that use more copper than PM and have high current loading. Prioritizing the reduction of the stator mass seems an effective way to improve torque density in this optimization case. Pole number increases as the diameter grows. Current density for 1S machine increases to its upper boundary (5 A/mm^2), whereas it stays close to the upper boundary for MS machines. This can partly explain why 1S machine has higher efficiency than MS machines. As the diameter grows, the aspect ratio decreases and σ increases, indicating that machines become more like rings. Also note that as an important indication of the torque density, σ varies with the application (e.g. 0.7-0.8 recommended for ship propulsion [112]). Figure 5.4(j) reveals the diameter-dependency of σ, which can be greater than 0.9 in this design case. The increase in the voltage drop ratio implies the increase in the reactance, and thus the decrease in the power factor.

5.4.2 Optimal machines (highest efficiency)

As shown in Figure 5.5(a), the efficiency does not vary much with the increase in the diameter, whereas the more number of stages, the lower efficiency the machine has. This is mainly due to the higher copper loss in the MS machines.

The other parameters are given in Figure 5.5(b)-(j). As the diameter increases, the torque density increases and the power cost decreases. Above observations suggest that, in term of optimizing the efficiency, it is better to build a 1S machine at a large diameter. Even if the diameter is constrained to a small value, machines with fewer number of stages still outperform those with more number of stages.

As the diameter grows, B_{p1} decreases, whereas k_M almost stays constant around 0.77, which is close to the result (0.78) in [24] where the machine efficiency was optimized with Powell's method. Pole number increases in all three machines. Current density for all three machines remains close to its lowest boundary (2 A/mm^2), which helps to reduce copper loss. The aspect ratio and σ present the same trend as the previous case. Voltage drop ratio for 1S machine keeps almost stable, whereas it increases for MS machines.

5.4.3 Optimal machines (multiple objectives at D_o = 18 m)

Practically, the determination of the optimal machines involves the trade-off of multiple objectives. The formulation of a multi-objective fitness function normally depends on the specific application and the optimization algorithm [119]. In this study, the optimal machines that satisfy the following objectives at outer diameter 18 m are investigated:

- The active weight is lower than 60 ton.

- The efficiency is greater than 95%.

- The power cost is the lowest.

The best designs from all three machines are given in Table 5.2, which shows that the optimal design is a 2S machine because of the lowest power cost. This optimal design also has the highest torque density, but its efficiency is lower than that for the best 1S machine. This optimization case implies that there is no general rule to follow, i.e., prioritizing 1S solution or MS solutions, if multiple objectives come into the consideration.
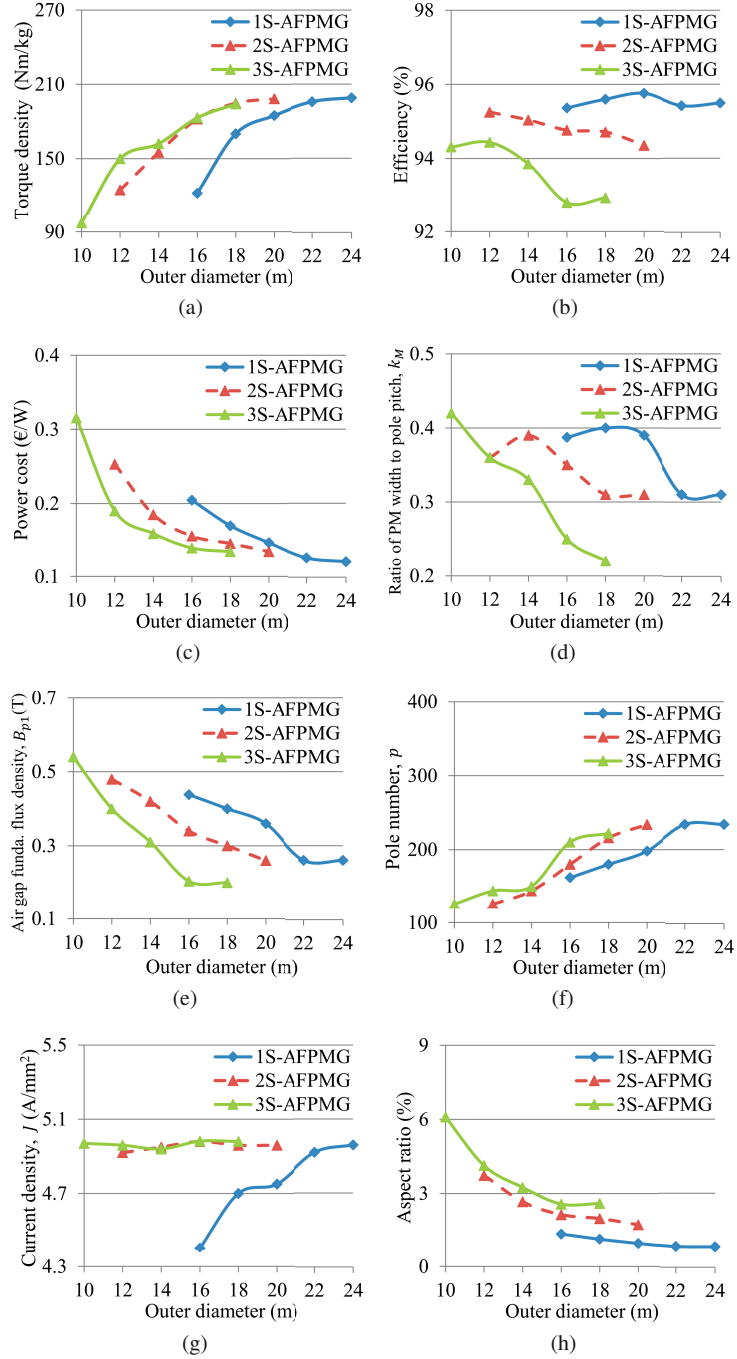
Figure 5.4: Performance of the optimal designs in term of highest torque density. (*Continued.*)

(i)   (j)

Figure 5.4: Performance of the optimal designs in term of highest torque density.

(a)   (b)
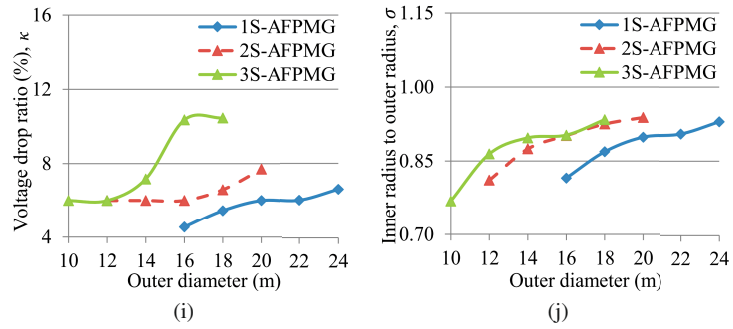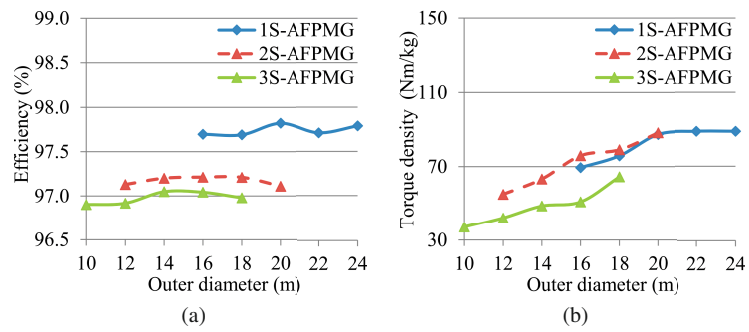
Figure 5.5: Performance of the optimal designs in term of highest efficiency. (*Continued.*)
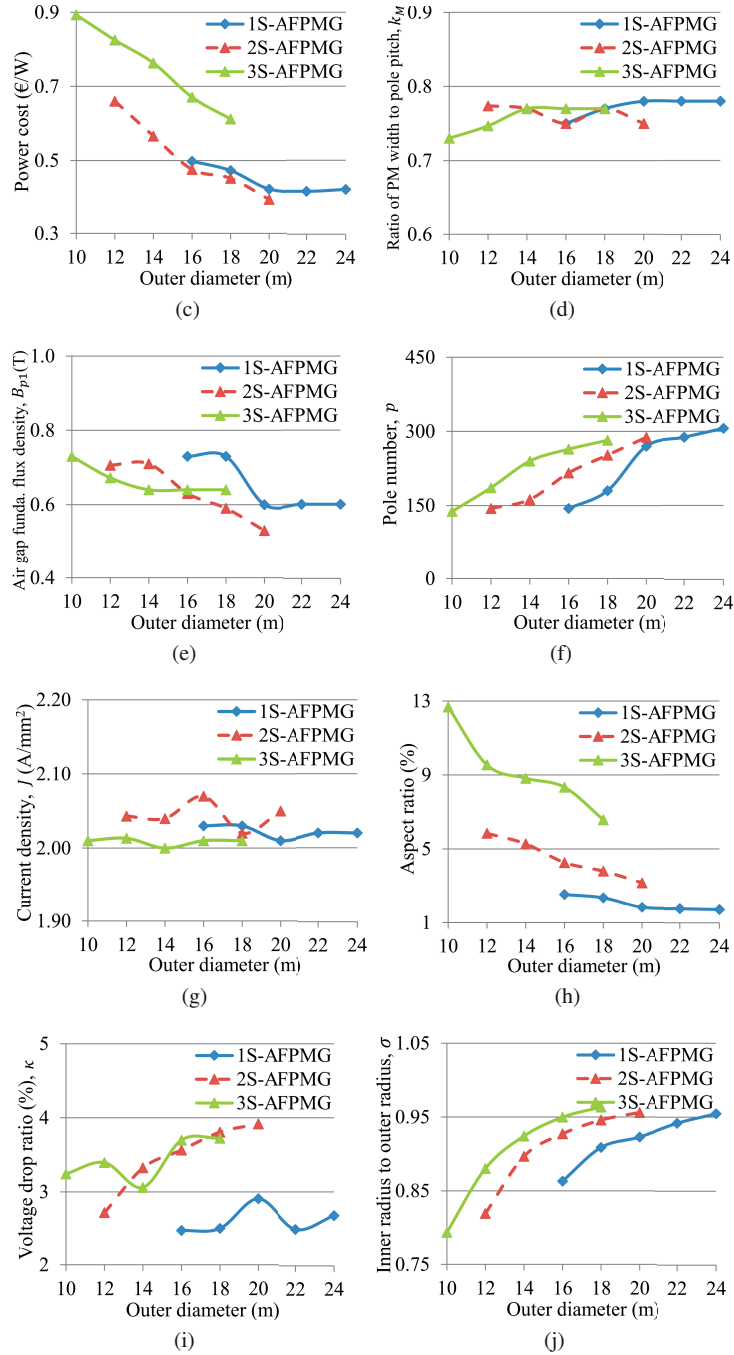
Figure 5.5: Performance of the optimal designs in term of highest efficiency.

Table 5.2: Optimal designs in term of multiple objectives.

Machines	k_M	B_{p1} (T)	p	J (A/mm^2)	Aspect ratio (%)	κ (%)	σ	Torque density (Nm/kg)	Efficiency (%)	Power cost (€/W)
1S-AFPMG	0.40	0.40	180	4.70	1.15	5.45	0.87	170.08	95.6	0.17
2S-AFPMG	0.42	0.37	180	4.65	2.08	7.28	0.93	171.69	95.1	0.16
3S-RFPMG	0.39	0.29	204	3.38	2.82	8.85	0.94	148.94	95.1	0.18

5.4.4 Summary of the calculation results

Following general conclusions can be drawn from the above three investigations:

- The diameter and number of stages significantly affect the performance of ironless MS-AFPMG.

- If there is no dimensional constraint, it is always better to design a machine at a larger diameter for higher torque density and lower power cost. But of course, the weight of the inactive parts (supporting structures) is not taken into account.

- If there are dimensional constraints, the number of stages will affect the determination of the optimal machines at a fixed diameter. Generally, machines with more number of stages tend to have lower efficiency because of more copper losses.

- In some cases, e.g., there is only one design objective for a small diameter, or there are multiple objectives, MS machines will outperform 1S machine.

- Machines with high torque density tend to have high current density, small k_M, and low air gap field, whereas machines with high efficiency tend to have low current density, large k_M, and high air gap field.

- Note that similar optimization results for 1S-AFPMG are reported in [116], however, compared to the results in this study, the positions (values of free variables) where the optimization results are obtained are different. This implies the importance of having enough population and generations in this kind of integer-mixed GA-based optimizations.

5.5 Summary

This chapter presents an investigation into the effects of outer diameter and the number of stages on the performance of ironless MS-AFPMG.

To assist this investigation, a form factor is introduced and used to upgrade the previously developed design strategy, with the aim to reduce the calculation load and shorten the calculation time.

This upgraded design strategy, which employs 2D and 3D SFEAs and GA for machine optimization, is used to investigate the optimal ironless MS-AFPMGs in terms of highest torque density, highest efficiency, and multiple objectives.

It has been shown that, direct-driven ironless MS-AFPMG normally has low B_{p1}, low aspect ratio, large pole number, and high σ, whereas k_M and current density vary with the

99

fitness function. Without considering the inactive weight, it is always preferred to build an ironless 1S-AFPMG. However, if there are dimensional constraints, the MS solutions may outperform 1S solution. When the design has to deal with multiple objectives, the optimization becomes complicated, and the case-by-case investigation is needed.

Structural and thermal analyses are out of the scope of this study. Nonetheless, it should be pointed out that, maintaining the structural reliability and providing proper cooling arrangement are two crucial aspects in offshore wind turbines, which should be taken into account in the system design, and consequently, the above investigation results may be affected.

Chapter 6

Multiphysics 3D Modelling Approach

This chapter presents a multiphysics modelling strategy for the design and optimization of an iPMG. Section 6.1 discusses the needs of reducing the computational cost and calculation time. Section 6.2 presents the design specialities of iPMGs, the modelling method and calculation results are given in Section 6.3 and 6.4. Section 6.5 discusses the challenges of using large-scale computing resources (LCR), and Section 6.6 concludes this chapter.

6.1 Introduction

LCR, e.g. clusters and super computers, are used to handle computation-demanding problems, such as the models for fluid dynamics and structural mechanics. This is due to the significant speedup ratio achieved with high performance computing techniques. However, it is not common to design electrical machines with LCR.

There are two main reasons. First, machine designers normally prefer to design and optimize machines with an analytical approach, and FEA is conducted later to verify the optimization result. Such a design process can be executed with ordinary PCs, desktops, or workstations. However, the prerequisite for making this design procedure feasible is the accuracy of the analytical method used. Machine designers therefore have to put a lot of effort into developing suitable analytical methods in terms of high accuracy and short calculation time. Unfortunately, depending on the specific analytical method used, significant errors may be produced [120]. Consequently, corresponding optimization results can be questioned. Even though many analytical methods are claimed to have high accuracy, e.g. in [121], developing such a method can be understandably time-consuming.

Second, the computational cost of FEA is considered to be high. This computational cost includes the cost of FEA codes and the corresponding hardware, which should be

powerful enough to support the running of FEA codes. The cost of commercial FEA codes is normally charged according to the number of separate calculations (note: not all the FEA codes); whereas machine designers prefer parallelized optimization and hope to have as many simultaneous separate calculations as possible, so as to reduce the total calculation time. Therefore, the computational cost of using commercial FEA codes for parallelized machine optimization is normally unaffordable for many academic users. On the other hand, there are open-source codes that are free to use. Generally, these codes demand a certain level of knowledge into the software (e.g., knowledge about numerical calculation or specified scripting languages), or have limited capabilities (e.g., no preprocessing or postprocessing interfaces, no adaptive mesh, incapable of handling 3D/multiphysics problem). According to the author's knowledge, in the field of electrical machine design, there is no single 3D open-source (or free) FEA package that can cover all the three steps of a FEA (preprocessing, solving, and postprocessing) for both electromagnetic and thermal problems.

As shown in the previous chapters, it is time-consuming to optimize iPMGs with FEM if the optimization is not parallelized, and the computational cost is high if commercial codes are used for parallelized calculations.

6.2 Design specialities

An iPMG is normally adopted into the wind turbine with the so-called *integration design* approach. Under this design philosophy, the generator shares the supporting structures with the other parts of the wind turbine, such as blades, hub, and nacelle [34]. Figure 6.1 shows an industrial design example following this concept. This turbine does not have the conventional hub, and the iPMG is supported with spoked structures integrated with blades and main shaft. In such a way, the whole system weight can be significantly reduced.

A notable feature of iPMG is its large-diameter structure, which contributes to torque production, but also poses challenges. First, the ring-shape iPMG normally has a small aspect ratio, which demands the 3D approach to investigate the magnetic and thermal field. Second, it is through the air gap that the kinetic power is transformed into electricity, therefore, maintaining a reliable air gap is crucial, considering the external force due to strong wind (even gusts) and internal force due to the generator operation. A small air gap requires a stiff supporting structures, whereas a larger and safer air gap demands more consumption of the expensive PM. Third, the spokes and bearings that support the generator should be capable of withstanding the generator gravity, operating torque, rotor to rotor normal stress (if there are multiple rotors), and extreme forces caused by faults. Forth, contrary to conventional generators where the active parts (windings, iron, and PM) are enclosed within a frame to exclude harsh external environment or maintain an enclosed cooling system, large-diameter iPMG may be not enclosed in a frame to take advantage of the cooling effect of nature air. However, because of the height difference (can be
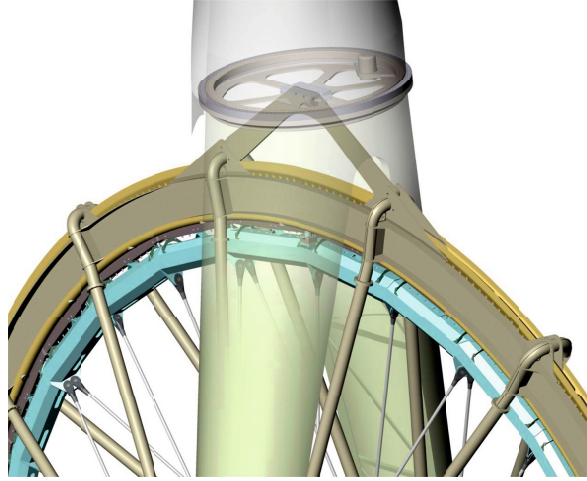
Figure 6.1: The concept of integration design [122].

greater than 20 m) from the generator top to its bottom, there can be different local air flow attacking the generator, in addition, the blades rotation makes the local air flow more complex. Therefore, it can be difficult to estimate the winding temperature. Considering the aforementioned points, the design approach should be capable of addressing these specialities.

6.3 Modelling method

Design strategies were developed for the design and optimization of iPMGs in Chapter 4 and Chapter 5. To limit the calculation load, only the magnetic field was considered in these design strategies. It was assumed that machine thermal reliability can be guaranteed by the settings of the maximal current density and electric load. However, these settings are based on the design experience of low-power iron-cored PMG. Furthermore, commercial codes were used in this design strategy.

In this research, this design strategy is improved to account for the thermal aspect with 3D thermal FEA, and all the calculation tools are open-source codes. The upgraded design procedure is illustrated in Figure 6.2. The calculation starts with the stator sizing, then the flux density in the air gap is calculated in 3D SFEA with the given dimension. Afterwards, the maximal winding temperature at rated load is obtained in 3D thermal FEA. Finally, the value of the fitness function is calculated. This design approach is driven by a genetic algorithm (GA) optimization code, which manages the GA routine including initialisation, producing new populations and generations, and the evaluation of the stopping criteria.
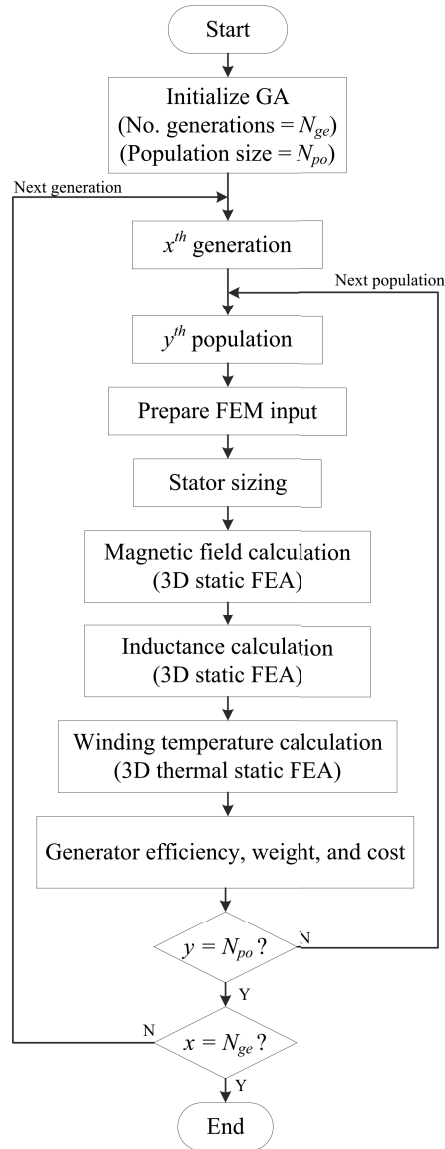
Figure 6.2: Design procedure.

Whether the FEA should be 2D/3D and static/transient depends on the type of the problem and the computational cost. iPMGs have small aspect ratio, the magnetic field therefore presents a significant 3D feature. For a machine with Litz wires, the thermal conductivity of the stator is anisotropic, and therefore the thermal analysis has to be conducted in 3D FEA, otherwise significant error will be produced. Calculating the inductance in 3D FEA is straight forward, because inductances are obtained directly for both

104

Create mesh (Salome 6.6.0, python)	→	Solve (Elmer 7.0, .sif script)	→	Postprocessing (Paraview 3.14.1, python)

Figure 6.3: Flow chart of the 3D FEAs.

winding active length and the end parts. The benefit of TFEA is to get some additional time-dependent output besides the basic field parameters (potential, flux density, field strength), such as losses and back-EMF. Because 3D TFEA is equivalent to multiple static analyses and is more time-consuming, and the losses and back-EMF for the rated load can be obtained with analytical approach with the basic field information. Therefore, no 3D TFEA is used in this research.

In this research, the three steps for a FEA (preprocessing, solving, and postprocessing) are handled by different codes (Figure 6.3): Salome 6.6.0 [123] (for creating mesh), Elmer 7.0 [124] (for solving multiphysics problems) and Paraview 3.14.1 [125] (for extracting the calculation results). Python is the main scripting language for pre- and postprocessing, whereas the solving routine is written in an Elmer-specified .sif script. Note that the calculations of magnetic field, inductance, and thermal field demand different geometries, and therefore there is no universal mesh for all cases. Unlike commercial codes that have reliable adaptive mesh feature, the user has to make sure that fine mesh is created while using the open-source code. This can be done by increasing the mesh in the air gap.

The optimization tool is the GA of Octave [126]. The optimization process is written in .m script of the Octave. All the calculations are executed sequentially. The population size is determined by the number of free variables, and the number of generations is determined by the convergence of the fitness function.
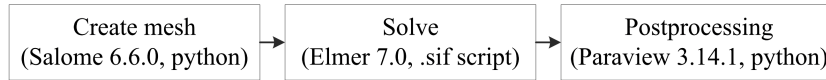
6.4 A design example

This section presents a design example that uses the aforementioned design approach.

6.4.1 Machine type

The topology of this generator is the same as that in Figure 5.2, except the use of Cartesian coordinate system. It is a single-stage 2R-CA-AFPMG. The two rotors always have opposite poles facing each other, in such a way, the main flux goes across the air gap. The stator is sandwiched between the two rotors. Non-magnetic material is used to hold the stator, which is segmented into several physically separated parts to facilitate the transportation. Heavily twisted Litz wires are used to minimize the eddy current loss.

6.4.2 Design specification and assumptions

The specification of the studied machine is given in Table 6.1. The main parameters of this specification are the same as that in Table 4.1. To facilitate the readers, these overlapping parts are represented. The reason why h_M and h_{ry} are used as the free variables instead of B_{p1} is because there is no internal optimization method inside Elmer from which h_M and h_{ry} can be determined according to the required B_{p1} and constraints on B_{ry}, and these two variables are more straightforward. Selecting σ as the free variable makes the active length directly obtained, in such a way, the back-EMF can be easily calculated for the given dimension after the magnetic field calculation. The thermal reliability is maintained by setting a constraint on the maximal winding temperature rise.

In this study, for a F-class insulation, the maximal winding temperature rise is set to 90°C for a 40°C ambient with direct air cooling. The winding thermal conductivity is anisotropic because of the insulation. The radial component of the winding conductivity is close to that of the pure copper; the components of the z and θ axes are dependent on wire type and the detail layout of the coil cross section. In this research, they are assumed to be same, and the equivalent thermal conductivities of these two axes are specified according to [127] (randomly distributed round wires, fill factor is 0.5). In large PM machines, the PM pole normally consists of several small PM blocks. This formation may influence the thermal conductivity along the segmentation direction. In this research, the main cooling path is in the z direction, and the segmentation will not happen in this direction. Therefore, the impact of segmentation is ignored. The rotor yoke is made of solid iron, the thermal property of rotor yoke is therefore isotropic.

6.4.3 FEA models

To serve the magnetic field analysis, inductance calculation and thermal analysis, different models are used (Figure 6.4 - 6.6).

In the magnetic field analysis, it is of interest to get the field distribution in the air gap and rotor yoke. To calculate the back-EMF, it is enough to model rotors only. A dummy object is placed between the two rotors for generating a fine mesh in the air gap. Only one pole pitch is modelled to take advantage of the machine symmetry. Elmer has special constraints for using the periodic boundary, therefore, it is not a single pole modelled, but two half poles. In such a way, the normal component of the field is set to zero on the symmetry boundaries, which is a boundary type supported in Elmer. The remaining four boundaries are Dirichlet boundaries.

In the inductance calculation, the method used is to calculate the rated flux linkage, and by dividing this flux linkage with the rated current, the self-inductance will be obtained. In such a process, the magnetization of the PM poles is set to 0, i.e., the saturation
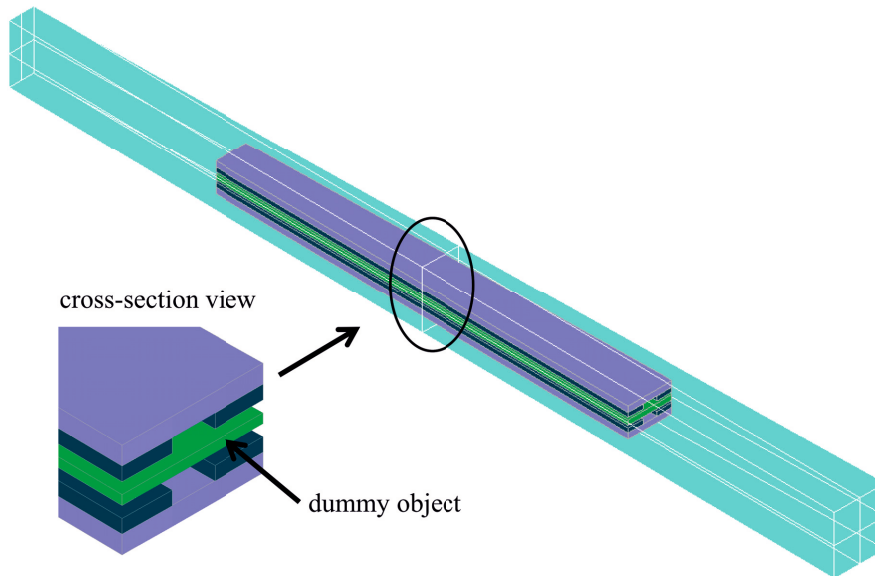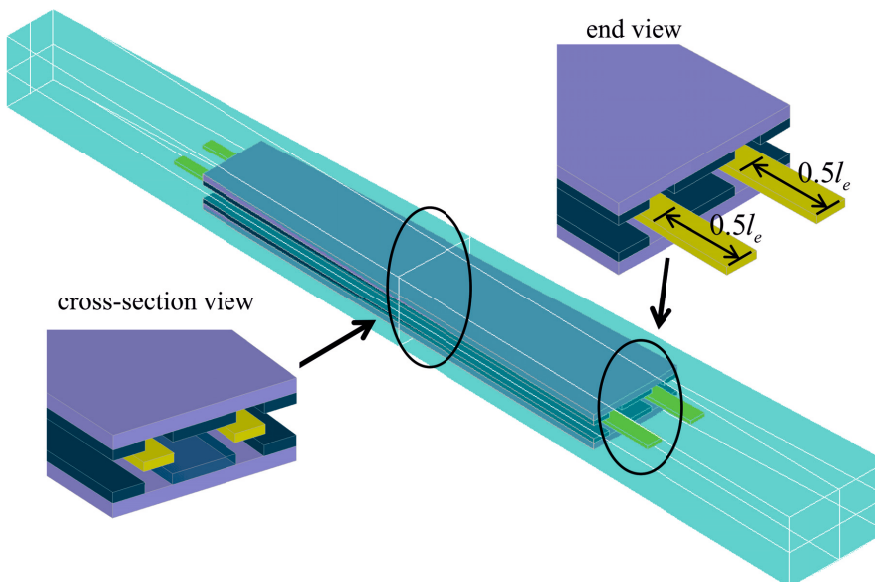
Figure 6.4: Field-calculation model.

Figure 6.5: Inductance-calculation model.

Table 6.1: Generator specification.

Parameters	Types	Value
Rated power (P_N), MW	*Constant*	10
Number of phases (m)	*Constant*	3
Rated speed (n_N), rpm	*Constant*	12
Rated voltage (U_N), kV	*Constant*	6.8
Number of stator segments (n_s)	*Constant*	9
Number of parallel branches (a)	*Constant*	1
Coil fill factor (k_f)	*Constant*	0.5
PM(N42SH) B_r at operating temperature, T	*Constant*	1.2
Permeability of PM	*Constant*	1.05
PM specific cost, €/kg	*Constant*	80
Iron (solid steel) specific cost, €/kg	*Constant*	16
Copper specific cost, €/kg	*Constant*	27
Outer diameter (D_o), m	*Constant*	20
Thickness of the air gap (g), mm	*Constant*	$0.15\%D_o$
Winding thermal conductivity (radial direction), W/(mK)	*Constant*	395
Winding thermal conductivity (perpendicular to radial direction), W/(mK)	*Constraint*	0.8
PM pole thermal conductivity, W/(mK)	*Constant*	6
Rotor yoke thermal conductivity, W/(mK)	*Constant*	50
Rated frequency (f), Hz	*Free variable*	10-70
Ratio of inner diameter to outer diameter (σ)	*Free variable*	0.5-0.95
Ratio of PM width to pole pitch (k_M)	*Free variable*	0.1-0.8
Current density (J), A/mm^2	*Free variable*	2-5
Thickness of the PM (h_M), mm	*Free variable*	5-100
Thickness of the rotor yoke (h_{ry}), mm	*Free variable*	5-100
Number of turns per coil (N_s)	*Free variable*	1-10
Max. flux density in air gap (B_{p1}^{ref}), T	*Constraint*	0.8
Max. flux density in rotor yoke (B_{ry}^{ref}), T	*Constraint*	1.7
Max. winding temperature rise (t),°C	*Constraint*	90
Number of population	-	100
Max. number of generation	-	30

in the rotor yoke is less than that it is supposed to be. Because less saturation is considered, the calculated inductance will be greater than its real value. Two pole pitches are modelled to accommodate one winding, and only the two straight sides of the winding are modelled to simplify the excitation setting. To take into account the end inductance, the total length of the two straight conductors equals the total length of a complete coil.

The main heat source is the stator copper loss, which is removed by the convection in the air gap. Accurately taking into account the convection requires the knowledge of the heat transfer coefficient, which is dependent on the machine geometry and local air
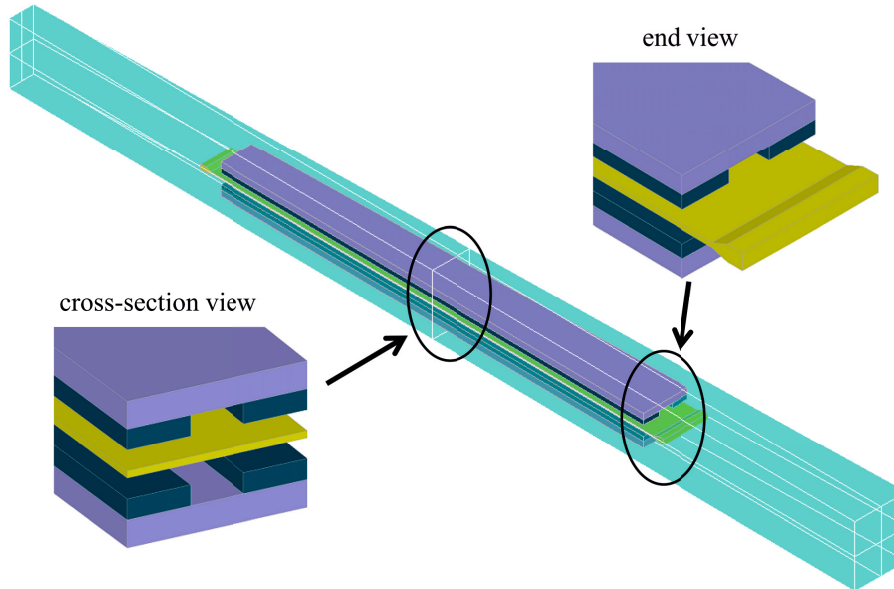
Figure 6.6: Thermal model (l_e is the length of single-side end coil).

flow dynamics [128]. CFD analysis is normally required for a good understanding of the air flow. However, this requires the structural design, because the generator for this kind of large structure will normally not have enclosure. The natural air will directly hit the turbine structures including the rotor yoke. Some air will go into the air gap. Meanwhile, the rotor rotation will produce additional air flow, which can help the cooling of the winding. Therefore, an accurate model should be capable of handling these two air flows. Structural design is out of the scope of this research, air flow and convection are therefore ignored in the thermal analysis. Once the structural design is defined and parametrized, the proposed design strategy can be easily extended to include the CFD analysis. Air gap convection may be replaced with an equivalent thermal conduction [129]. However, this method requires the tests on similar machines for an averaged thermal conductivity. In this research, only heat conduction is considered, and the air equivalent thermal conductivity is set to ten times the thermal conductivity at ambient temperature. The winding is modelled like the practical shape after encapsulation. There is no heat flow in the symmetrical boundaries, and the remaining four boundaries are set to ambient temperature.

6.4.4 Key equations

The iPMG stator is sized according to the approach presented in Chapter 4. There is no need to size the rotor, because the rotor dimensional variables are free variables, and the air gap is 0.15% of the outer diameter. With all these inputs, it is ready to do the magnetic field analysis.

The main task of the magnetic field analysis is to calculate the back-EMF. Normally it requires multiple SFEA or TFEA, which can be time-consuming. The method used in this study only employs a single SFEA.

The rated back-EMF per phase (E_N, in RMS) is calculated with

$$E_N = \Phi_0 k_{ff} \omega_E N_1 k_{w1} / \sqrt{2}, \qquad (6.1)$$

where Φ_0 is the maximal flux produced by a pole, ω_E is electrical angular velocity. Φ_0 is calculated by integrating the z-component of the flux density (B_z) over the conductor plane under a pole in the postprocessing of a 3D SFEA. k_{ff} is calculated with (5.2).

The main heat source is the copper loss (P_{cu}). The power density for the winding (H_w), used at the heat source, is calculated with

$$H_w = \frac{P_{cu}}{m_S} k_f, \qquad (6.2)$$

where m_S is the stator mass. Coil fill factor (k_f) is used to account for the distribution of copper in the stator. Note in practical calculation, the initial copper conductivity is adjusted to that for 90°C. The actual working temperature obtained from the thermal analysis, is used to calculate the copper loss and efficiency. However, to simplify the calculation, this re-calculated copper loss is not used to re-launch the thermal analysis.

3D TFEA shows that the loss in the permanent magnet is at the level of $1\ kW/m^3$, therefore, the power density for the permanent magnet (H_M) is

$$H_M = \frac{1000}{\rho_M} = 0.133 W/kg, \qquad (6.3)$$

where ρ_M is PM density.

The loss in the rotor yoke is very low, thus ignored.

6.4.5 Calculation results

The objective of this optimization example is to find the optimal design in term of highest efficiency. eight cores of the supercomputer Vilje (Appendix C) were used to do the calculation. It took around a week (clock time) to complete the calculation (note: it was attempted to run many calculations simultaneously over dozens of cores, but it turned out that the meshing code prevented the parallel meshing operation, therefore, this attempt was given up). The calculation results are given in Table 6.2.

The current density is close to its lower boundary (2 A/mm^2) and k_M is close to the upper boundary (0.8), which are the necessary inputs for achieving high efficiency solution.

Table 6.2: Optimal machine in term of highest efficiency.

Parameters	Value
Rated frequency (f), Hz	43.2
Ratio of inner diameter to outer diameter (σ)	0.696
Ratio of PM width to pole pitch (k_M)	0.795
Current density (J), A/mm^2	2.25
Thickness of the PM (h_M), mm	20.25
Thickness of the rotor yoke (h_{ry}), mm	19.15
Number of turns per coil (N_s)	4
1st order flux density in air gap (B_{p1}), T	0.442
Winding temperature rise (t),°C	88.64
Power factor	0.997
Active weight, ton	75.2
Active cost, €	3.29
Efficiency, %	98.1
Total calculation (clock) time, hours	156.32

Air gap flux density is low due to the large equivalent air gap. Note the main component of the air gap field is its component at z axis (Figure 6.7). At the ambient temperature (25 °C), the static winding temperature rise is close to the maximal allowable temperature rise. The temperature distribution for the machine end part is given in Figure 6.8. Power factor is high due to the ironless structure. For this optimal design, the torque density and power cost are 105.8 Nm/kg and 0.329 €/W respectively. The calculated efficiency is higher than that given in Chapter 4, this may be due to the air gap conduction that underestimates the air cooling. It is possible to get better results by extending the calculation time, however, it was not tried because the purpose is to demonstrate the feasibility of this design strategy.
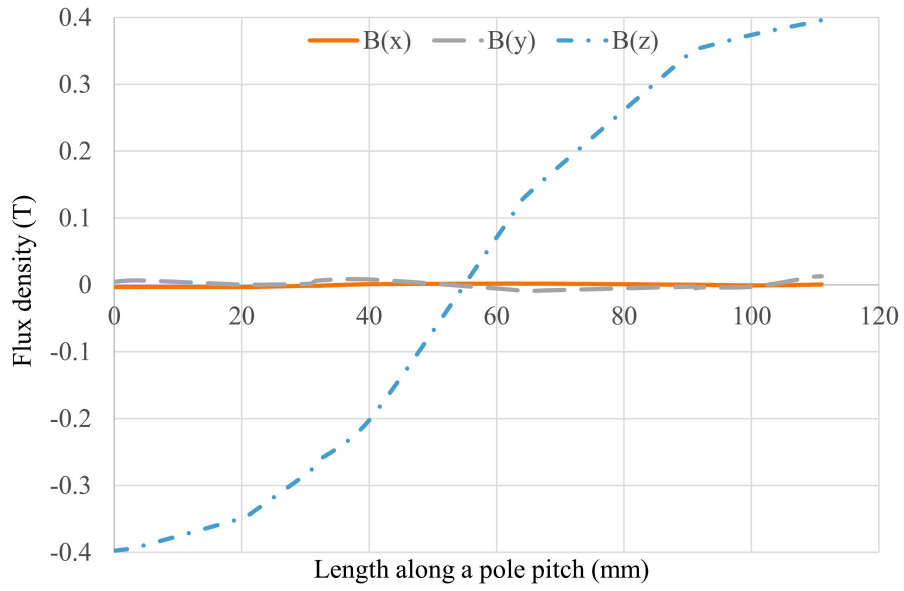
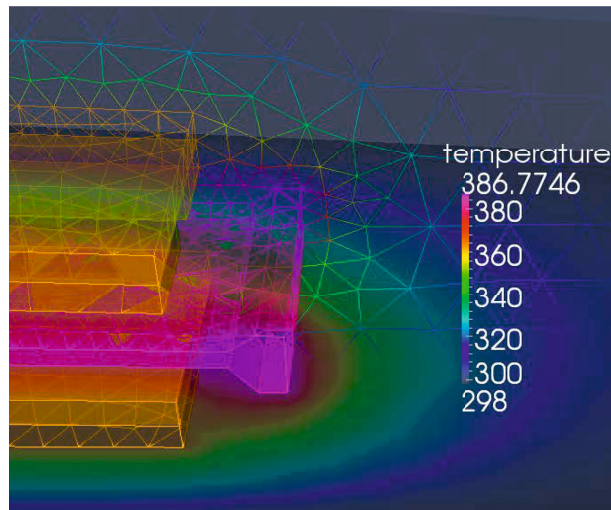Figure 6.7: No-load air gap flux density.

Figure 6.8: Machine end part mesh and temperature distribution.

6.5 Large-scale computing resources

The trick of gaining speedup with LCR is at parallelizing the repetitive calculations. There are two parallel-computing cases. The first one is to "split" one big calculation into small calculations, e.g., use domain decomposition method to divide a large mesh into several small meshes. Unfortunately, because of the so-called memory wall problem [130], the speedup ratio, depending on many factors (models, algorithm, hardware, etc.), is normally limited. The commercial code MagNet demonstrates a speedup of approximate two from one core to four cores [131]. The author's test shows that there is normally no obvious speedup with the latest commercial FEA codes if the CPU core number is greater than 16, and the maximal speedup is around 5-6. As reported in [132], specific-purpose in-house codes may have better performance, however, so far it is still the game of people focusing on numerical calculation. The second way is to distribute a large amount of independent small calculations over the available computing nodes. Because of the independence, the speedup ratio can be near linearly increased. This normally fits the need of machine optimization. However, as aforementioned, the computational cost can be very high, because of the need of large number of licenses if commercial codes are used (note: this claim is valid at least when the work was conducted).

Using open-source codes for machine optimization on LCR is attractive, but some problems should be addressed in the design strategy. As a basic requirement, all FEA tools should be parallelized, e.g., no data messed or codes crash, if more than one session are executed simultaneously.

Furthermore, the optimization algorithm should be capable of working together with the job scheduler, so that it is possible to take advantage of the parallelization. Unfortunately, unlike commercial codes that have well-established interface to integrate parallization into optimization algorithms, such open-source codes are still under development. Using message passing interface (MPI) or similar commands can be an indirect solution, but it demands the scripting skill to piece together the optimization algorithm and parallel mechanism, and depending on the specific parallization method, the optimization performance may be downgraded.

6.6 Summary

Large-diameter iPMGs have small aspect ratio, and this feature demands an approximate design approach. This chapter presents a 3D multiphysics design strategy to meet this need. A design example is given to show the feasibility of this design strategy.

It is found that open source codes have to be used to enable the use of super computer, given the high cost of commercial codes. However, state of the art open source codes

are still needed to be further developed for supporting the parallelization of repetitive calculations.

Chapter 7

Generator Efficiency Improvement

This chapter focuses on the accurate calculation and improvement of the generator efficiency in the direct-driven drive train where large-diameter iPMGs and diode rectifier are used. The shunt active filter controlled with instantaneous ABC theory is investigated for mitigating current harmonics. Section 7.1 presents the background information about this research topic. The studied WECS is presented and modelled in Section 7.2 and Section 7.3. The loss calculation is given in Section 7.4, and Section 7.5 presents the calculation results. Section 7.6 concludes this chapter.

7.1 Introduction

The promising direct-driven WECS with PMG is recommended for offshore wind power application because of the high system efficiency compared to the main-stream geared WECS [52]. However, a high-efficiency system may be not accepted in the market unless the system cost is well controlled.

The converter with active rectifier is normally used in direct-driven drive train for controlling the generator's speed and power. However, the use of controllable switches and the corresponding control techniques introduce several disadvantages to the system. First, high-power controllable switches are relatively expensive and the more controllable switches used, the more expensive the converter is. Second, the harsh offshore environment may affect the normal operation of the controllable switches and other sensitive auxiliaries, such as microprocessors and sensors. Third, the voltage output of the active rectifier consists of steep pulses, which requires the use of the corresponding filter in the converter as well as reinforced insulation in the generator. Therefore, the generator controlled by an active rectifier can be heavy and expensive.

The use of the converter with diode rectifier in direct-driven drive train brings sev-

eral benefits [133], [134]. First, the converter with diode rectifier is cheaper, simpler, and more reliable than the converter with active rectifier. Second, the speed control of the generator is implemented through a DC/DC converter and there is no reactive power control, thus the control algorithm becomes simple. Third, the output voltage profile of diode rectifiers contains less steep pulses, thus there is less need to strengthen the generator insulation than that in the case of active rectifier. Nevertheless, the use of diode rectifier also has drawbacks. Because the excitation of the PMG and the diode rectifier are uncontrollable, normally the reactive power compensation is needed if the generator inductance is relatively large. Furthermore, the operation of the diode rectifier injects low frequency harmonics in the generator current. The solution of using shunt passive filter to filter certain orders harmonics is incapable of following the variable wind speed. The active filter is flexible, but compensated result is much dependent on the type of active filter and the corresponding compensation algorithm. The improper use of compensation techniques may lead to discouraging compensation results [135] or the need of expensive compensator [136].

Generators with reactance higher than 0.5 p.u. are not recommended to be connected to diode rectifiers because of low power production [63]. Large-diameter iPMG is a promising solution for lightweight design [25]. Because of no iron in the stator, the reactance is normally low (< 0.4 p.u.). In such a case, it is not much beneficial to compensate reactive power with active rectifier, whereas the low cost and reliable diode-rectifiers become attractive.

7.2 Energy conversion system

Figure 7.1 shows the studied WECS, where a segmented PMG is connected to several diode rectifiers, and the speed control of the generator is implemented by controlling the DC bus voltage through a DC-DC boost converter.

The generator is an ironless one-stage 2R-CA-AFPMG. Because windings are held in epoxy material and no iron is used, this generator has the advantage of negligible attracting force between the stator and the rotor, which makes the design of supporting structures less challenging and the generators diameter can be very large.

Concentrated overlapping winding is used because of easy mass-production and short end-connection. The stator is segmented and m coils are removed from each segments for a m-phases machine to achieve the physical-separation between segments while maintaining an identical winding sets in each segment. PMs in each pole are axially magnetized.

Each segment of the generator is connected to a diode rectifier. The output of the diode rectifier is connected parallelly to the boost converter. The controlling of the boost converter is out of the scope of this research, so in practical simulation, a resistor connected in the DC-bus is used as the converter's load.
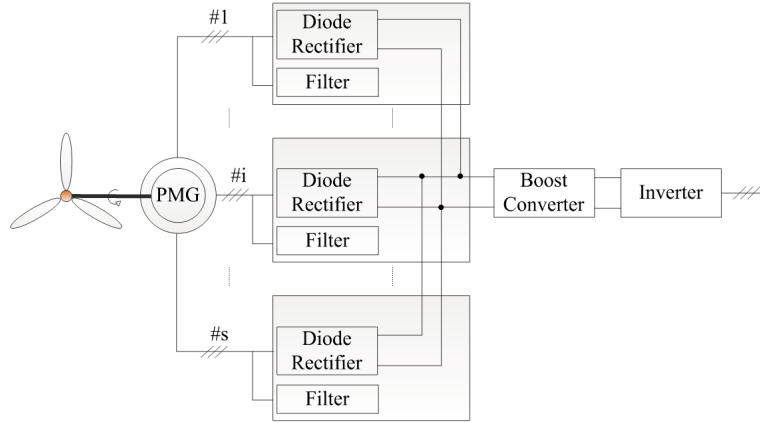
Figure 7.1: Studied wind energy conversion system.

The harmonics sources are the rectifiers which inject low frequency harmonics into the generator current. These current harmonics reduce the generator's capacity of delivering power and induce additional losses in the stator winding.

7.3 Modelling of the energy conversion system
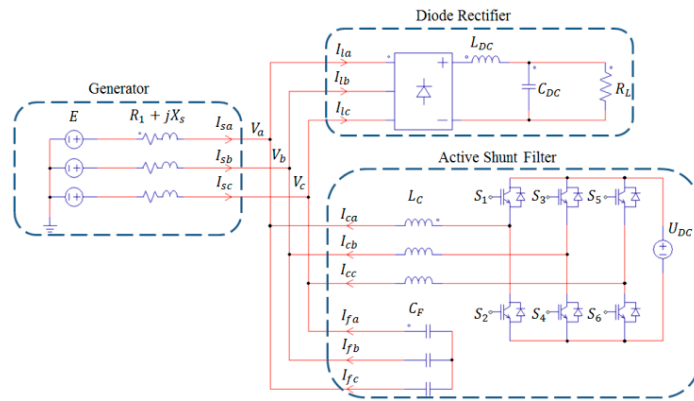
Figure 7.2: Diagram of the simulated wind energy conversion system.

The simulated model is shown in Figure 7.2. This is a part of the studied WECS because each generator segment and the corresponding diode rectifier are identical as in other power branches. Note that only the case of generator operating at rated load is studied, because it is wise to investigate how much the generator efficiency is improved when the generator produces maximal losses under normal operation.

Table 7.1: Generator parameters.

Parameters	Value
Rated power, MW	10
Number of phases	3
Rated speed, rpm	12
Rated line voltage, kV	6.8
Rated frequency, Hz	34.2
Rated load power factor	1
Outer diameter, m	24.8
Number of stator segments	9
Resistance per segment, p.u.	0.0416
Reactance per segment, p.u.	0.3633

7.3.1 Generator

The parameters of the simulated generator are given in Table 7.1, and the machine is designed with the method presented in Chapter 4. This generator is segmented into nine physically-separated three-phase segments with each segment rated at 1.11 MW so that a total of 10 MW output is obtained. The serial connection of an AC voltage source, resistor and inductor is used to model the generators back-EMF E, phase resistance R_1 and synchronous reactance X_s. The phase-neutral back-EMF of the generator is obtained from 2D TFEA and has significant amount of 3rd, 5th, and 7th harmonics. The total harmonics distortion (THD) is 5.96%.

The phase resistance is adjusted to the operating temperature and kept constant in time domain. In traditional iron-cored PMG, the synchronous inductance changes significantly as the rotor position is changed. However, in this ironless machine, the permeability of the PM is almost same as the air, and the thickness of air gap is much larger than PM thickness. Therefore, the variation of the inductance is not obvious. In practical simulation, the inductance is kept constant in time domain.

7.3.2 Compensation

A shunt active filter is used to eliminate the harmonics in the generator current. The main part of this filter is a three phase IGBT converter which supplies the required harmonic current following the specific algorithm according to the compensation purpose. An inductor and a capacitor are used to filter the high-frequency harmonics induced by the switching of the IGBT. A DC voltage source is placed in the DC-bus of the filter instead of a capacitor to simplify the control logic so that no control loop is required to balance the DC-bus voltage.

The modulation of the IGBT converter is based on the instantaneous ABC theory. According to classic ABC theory [137], [138], the current of the nonlinear load in a power system can be decomposed into instantaneous active current and instantaneous reactive currents. In a balanced system with sinusoidal source voltage, the minimal line current should be obtained if the compensator supplies the instantaneous reactive currents. However, if there are harmonics in the source voltage, it is impossible to achieve both sinusoidal source current and minimal source current simultaneously. This theory can be mathematically formulated into an optimization problem as shown below

$$min \sum (I_{lk} - I_{ck})^2, \tag{7.1}$$

subjected to

$$\sum_{k \in \{a,b,c\}} V_k I_{ck} = 0, \tag{7.2}$$

where I_{lk} is the instantaneous current of the nonlinear load at phase k, I_{ck} is the instantaneous compensation current at phase k, V_k is the instantaneous voltage at phase k. The target of this optimization problem is to have minimal line loss (7.1) at the requirement of no instantaneous active power supplied by compensator (7.2). By solving this problem, the reference current for modulating the compensator is obtained with (7.3).

$$I_{ck} = I_{lk} - \frac{P}{V_a^2 + V_b^2 + V_c^2}, \tag{7.3}$$

where the denominator is the sum of the squares of all the three-phase instantaneous voltages, and P is defined with

$$P = \sum_{k \in \{a,b,c\}} V_k I_{lk}. \tag{7.4}$$

In the studied WECS, the line loss is represented as the loss in the generator resistance. The control logic is shown in Figure 7.3.
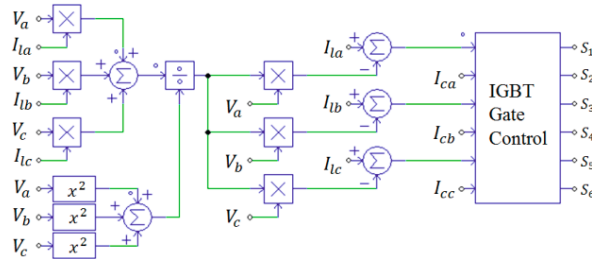

Figure 7.3: Diagram of the control logic.

7.4 Generator loss calculation

The main generator losses is the winding copper loss (P_{cu}). Litz wire is used in this machine to reduce the eddy current loss in the winding. The total copper loss in the generator winding can be described with

$$P_{cu} = n_s m \sum_{n=1}^{\infty} (I_n^2 R_n),$$ (7.5)

where I_n is the RMS value of the nth order harmonic current in each segment, and R_n is the winding AC resistance for n^{th} order frequency per segment.

The stator current is not evenly distributed in the cross section of the stator winding due to skin effect and proximity effects, which increase the AC resistance and loss. The phenomenon is described by the AC resistance ratio. In ironless machines, the AC resistance ratio of Litz wires is much lower than that in the iron-cored machines for the source of same frequency (Figure 4.11). In practical calculation, the influence of skin and proximity effects is neglected and the AC resistance ratio is set to one. Consequently, the copper loss becomes proportional to the square of the RMS value of the total current.

It is hard to know the exact temperature in the wires without the co-simulation of electromagnetic and thermal fields, which are much time-consuming and computationally demanding. Therefore, the conductivity is adjusted to the predefined working temperature rather than temperature-dependent.

The current-carrying capability of the conductors is limited by the cooling arrangement. Current harmonics occupy part of this capacity, induce additional losses, but have little contribution to the effective power production. So it is critical to analyse the current harmonics and eliminate them.

All the rest losses are calculated with the methods presented in Chapter 4.

7.5 Simulation results

Generators at different working conditions are compared to investigate the effect of compensation. Two cases are simulated: no compensation at rated load and compensating at rated load. The analysis process is illustrated in Figure 7.4, and the simulation parameters are given in Table 7.2.

The following assumptions are made during the simulations:
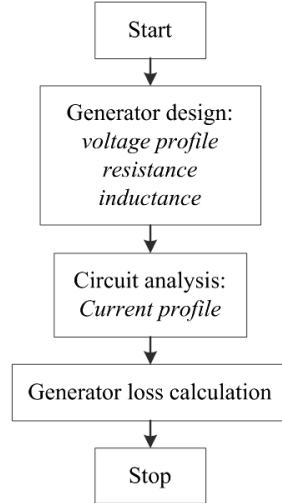
Figure 7.4: Analysis procedure.

Table 7.2: Simulation parameters.

Parameters	Value
L_{DC}, mH	1
C_{DC}, mF	0.47
L_C, mH	5
C_F, μF	0.5
U_{DC}, kV	12.5
	Case I: 51.45
R_L, Ω	Case II: 70.22

- All the components in the simulation are lossless.

- The variations of wind speed and grid are ignored.

- All the generator segments and diode rectifiers are identical.

- All the switches are ideal.

7.5.1 Case I: no compensation at rated load

In this case, the generator is operated at the rated power (1.11 MW). Diode rectifier is the only load and no compensation device is applied. The generator line current, phase voltage and line voltage per segment are given in Figure 7.5. As it shows, there are

significant harmonics in the current and voltage. The line voltage has less harmonics than the phase voltage because of the cancelling of the third harmonic.

(a)

(b)
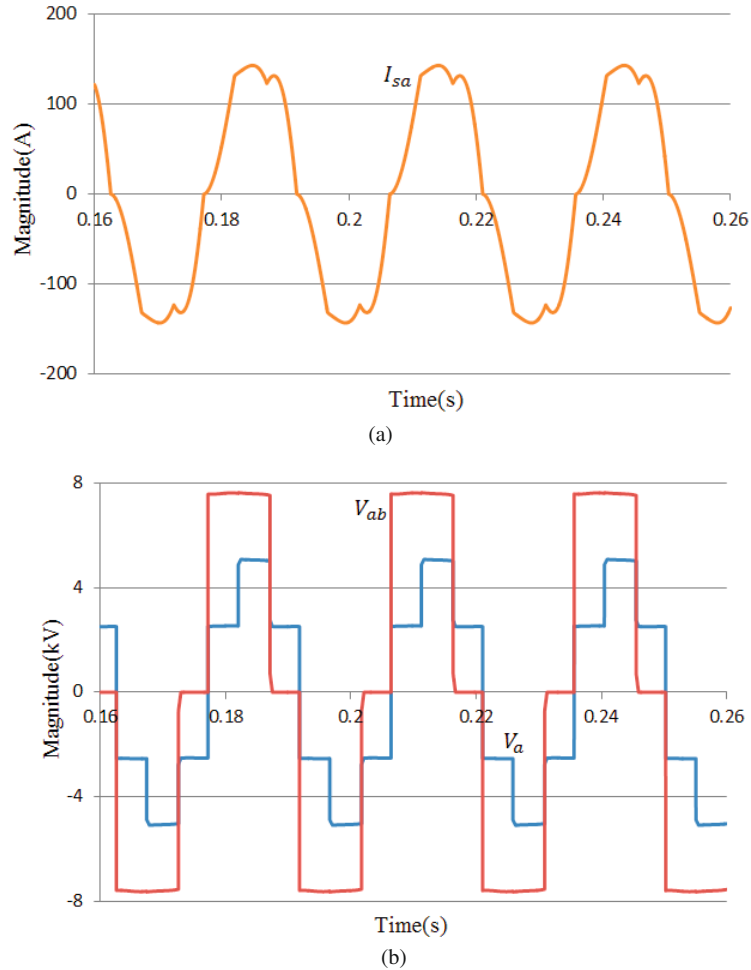
Figure 7.5: Case I: no compensation at rated load. (a) Generator line current; (b) Generator phase voltage and line voltage.

7.5.2 Case II: compensating at rated load

In this case, the power of the diode rectifier load is fixed (1.11 MW). The generator current, phase voltage and line voltage per segment are given in Figure 7.6. Compared to the first case, the current is closer to sinusoidal curve because of the compensation. However, the harmonics are not fully eliminated. The phase voltage curve is improved,

though there are significant high-frequency harmonics because of the switching of the active filter.

Quantitative analyses are given in Table 7.3 for showing the differences of above two cases.

(a)

(b)

Figure 7.6: Case II: compensating at rated Load. (a) Generator line current; (b) Generator phase voltage and line voltage.

7.5.3 Comparison

The simulation results are summarized in Table 7.3, and the following conclusions can be drawn.

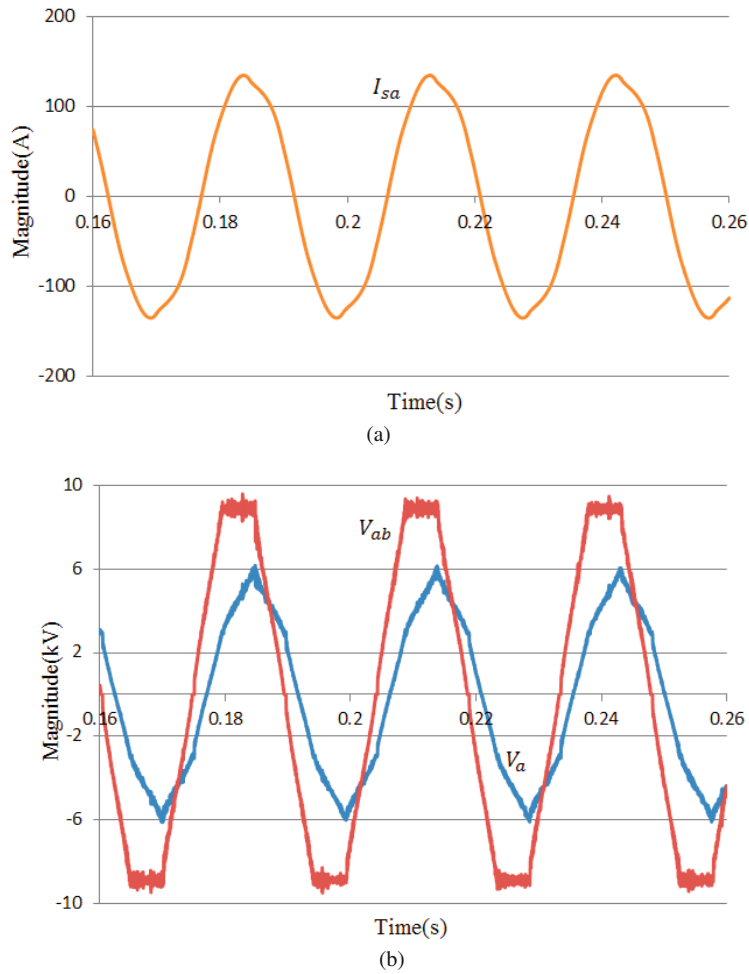- The filter with its reference current calculated from instantaneous ABC theory can significantly reduce the harmonics in the generator voltage and current, and the magnitude of the generator current is reduced as well. Nonetheless, pure sinusoidal generator current is not achieved, which matches the estimation.

- By keeping the load power unchanged, after compensation (from Case I to Case II), the generator efficiency is improved by 0.9%, and almost 100 kW saved from the stator copper loss. If the efficiency of the filter is assumed to be 97%, then the total loss of the filters for all the 9 segments will be 91.8 kW. Hence, the system efficiency improving by using active shunt filter is not significant.

- Even though the active shunt filter controlled with the instantaneous ABC theory shows better performance than the active shunt filter controlled with the p-q theory [135], and cheaper than the static synchronous series compensation [136], the effect of improving system efficiency with this method is not obvious because of high rating of the filter which produces additional loss.

Table 7.3: System performance comparison.

Parameters	Case I	Case II
Generator Line Voltage (RMS, V)	6295	6711
Generator Line Voltage THD	30.06%	5.26%
Generator current (RMS, per segment, A)	108.27	97.88
Generator current THD	10.61%	5.08%
Rectifier load (per segment, kW)	1111	1111
Filter apparent power (per segment, kVA)	0	340
Generator copper loss (whole machine, kW)	547.95	447.59
Generator other losses (whole machine, kW)	75.90	75.90
Generator efficiency (whole machine)	94.13%	95.03%

7.6 Summary

Compared to iron-cored PMGs, iPMGs have lower reactance, which makes it less beneficial using the expensive active rectifier for maximizing the power output of the generator. The features of low cost, simplicity, and reliability, make the converter with diode rectifier promising in WECS.

The instantaneous ABC theory aims at minimizing the supply current while delivering the same amount of power. This theory is used to control the active shunt filter, and the simulation results show that the generator loss can be significantly reduced. However, the system efficiency is not significantly improved, because the loss of the high-rating filter offsets the gain in generator efficiency. It is therefore not suggested to employ the

active shunt filter for harmonics mitigation and efficiency improvement. Nonetheless, it is still an attractive solution to use the converter with diode rectifier, as a trade-off of cost, reliability, and power yield.

Chapter 8

Conclusions

This chapter concludes the whole thesis. Section 8.1 highlights the findings obtained in this thesis, and discussions are provided to extend the thinking. Some research topics are recommended as the future works in Section 8.2.

8.1 Main findings and discussions

The first objective of this thesis has been to understand the state of the art generator technology for offshore wind power application. It is found that offshore wind power industry has seen fast development since the beginning of this century, and the dominant solution is the multi-stage geared drive train with induction generators, at the power of 3 MW. This is due to the borrowed technology from proven onshore wind turbines. Even though induction machines do not have high efficiency at partial load, their efficiencies (e.g. DFG) can be comparable to that of low speed PMGs. Several new concepts are now being developed in industry and academia. Among these new solutions, direct-driven iPMG seems promising for its relatively high reliability, low weight, and low cost.

The second objective has been to evaluate the iron-cored PMGs for offshore wind power application. It is found that most weight and cost of the iron-cored PMGs go to their inactive parts, which implies that using iron-cored PMGs is not a weight-/cost-effective solution for high-power wind turbines. Therefore, it is necessary to develop the technology for lightweight generators. Note that this finding is different with the claim in previous publication claiming that the percentage of the structural weight in the total weight increases faster than machine torque.

The third objective has been to investigate the performances of various iPMG designs. It is found that at the investigated outer diameter (20 m), optimal solutions can be obtained with 2R-CA-PMGs. The investigation on the diameter-dependency indicates that at large

diameter ($\geq$ 25 m), 2R-CA-AFPMG and 2R-CA-RFPMG start to follow the same torque density curve and similar efficiency curve. Whereas at small diameter ($<$ 25 m), RF machine has higher torque density than AF machine and similar efficiency as AF machine. At 10 MW level, a 12-rpm single-stage iPMG with a diameter of 20 m is lighter and less expensive than a 12-rpm iron-cored PMG with a diameter of 9.9 m. Without considering the inactive weight, it is always preferred to build an ironless single-stage AFPMG. However, if there are dimensional constraints, the MS solutions may outperform 1S solution. When the design has to deal with multiple objectives, the optimization becomes complicated, and the case-by-case investigation is needed.

The fourth objective has been to investigate the state of the art FEA codes and explore the frontier of machine simulation techniques. In this thesis, different calculation codes are used, including both open source codes and commercial codes. The machine models cover 1D, 2D, and 3D. The computing resources used range from ordinary PCs, multiple workstations, a computing server, and a super computer (tried). Using FEA codes to assist machine design improves the calculation accuracy, but the calculation can be time-consuming. Even though the design and optimization strategies are specially developed to reduce the calculation time, it takes from a week to ten days for optimizing the iron-cored PMGs or iPMGs with commercial or open source codes. It is tried to parallelize the repetitive calculations with open source codes in a super computer, but this attempt is not successful, because of the incapability of the 3D meshing and optimization codes.

The last objective has been to investigate the effect of using the instantaneous ABC theory for compensating the generator current harmonics and improving generator efficiency. It is found that the generator loss can be significantly reduced with an active shunt filter controlled with the instantaneous ABC theory. However, the system efficiency is not significantly improved, because the loss of the high-rating filter offsets the gain in generator efficiency. It is therefore not suggested to employ the active shunt filter for harmonics mitigation and efficiency improvement. Nonetheless, it is still an attractive solution to use the converter with diode rectifier, as a trade-off of cost, reliability, and power yield.

8.2 Future work

8.2.1 Structural design and CFD

The multiphyscs 3D approach presented in Chapter 6 ignores the convection phenomenon that happens in the air gap. This convection can affect the winding cooling significantly. CFD analysis helps to predict the air flow, which is essential to account for convection. However, taking into account CFD in a multiphysics optimization approach requires the structural design parametrized. Structural design is out of the scope of this thesis. Therefore, it is recommended to investigate the structural design of large diameter structures.

8.2.2 Parallel calculations with super computers

So far the best utilization of super computer is to do parallel optimization. This requires that all the codes can be parallelized, i.e. no data messed up for parallel sessions. However, not all the open source codes are developed for parallel calculation. This meshing code used in Chapter 6 prevents the parallel meshing operation. Therefore, how to parallel multiple calculations on super computer remains the work to be investigated.

8.2.3 Optimization algorithm

Given the high cost of using commercial optimization codes for parallel calculation, it is only practical to do machine optimization in super computer with open source codes. However, according to the author's knowledge, a descent optimization code, especially the kind that can be combined with parallel calculation, is hardly available. In addition, machine optimization has to figure out the global minimum from a large amount of local minima, which can be a challenge to ordinary optimization algorithm. Only genetic algorithm was tried in this thesis, it is recommended to explore other algorithms, and if possible, develop new algorithm, based on the open source codes.

Appendix A

Symbols and Abbreviations

A.1 Symbols

B_{p1}	1st order air gap flux density
B_{p1}^{ref}	reference air gap flux density
B_p	absolute air gap flux density or magnetic load
B_r	PM remanence
B_{ry}^{ref}	maximal flux density in rotor yoke
B_z	z-component flux density
C_{DC}	DC bus capacitance
C_F	filter capacitance
C_t	total cost of the active parts
D_a	average diameter
D_i	inner diameter
D_o	outer diameter
E	back-EMF
E_L	electric load
I_N	rated current for Y connection
I_{ca}, I_{cb}, I_{cc}	compensator currents
I_{ck}	instantaneous compensation current at phase k
I_{fa}, I_{fb}, I_{fc}	filter currents
I_{la}, I_{lb}, I_{lc}	load currents
I_{lk}	instantaneous current of the nonlinear load at phase k
I_{sa}, I_{sb}, I_{sc}	source currents
I_{ph_s}	rated current per segment
J	current density
L	phase self-inductance
L_C	compensator inductance
L_{DC}	DC bus inductance

L_e	end leakage inductance
L_s	synchronous inductance per phase
M	phase to phase mutual inductance
M_t	total machine weight
N_1	number of serial-connected turns per phase
N_s	number of turns
P	power
P_{Lconv}	converter loss
P_{Lgear}	gearbox loss
P_N	rated power
U_N	rated line voltage
U_{ph}	rated phase voltage
P_M	loss in PM
P_R	rotor power
P_d	power density
P_{cu}	copper loss
P_e	eddy current loss in winding
P_{fe}	iron loss
P_r	rotational loss
Q	total number of coils
Q_0	total number of coils before segmentation
Q_1	total number of coils after segmentation
Q_s	number of coils per segment
R_1	AC resistance per phase
R_{AC}	AC resistance
R_{DC}	DC resistance
R_L	load resistance
S_1-S_6	controllable switches
S_T	cross section of one turn coil
T	working torque
T_N	rated torque
T_d	torque density
U_{DC}	compensator DC bus voltage
V	machine volume
V_M	PM volume per pole
V_a, V_b, V_c	generator terminal voltages
V_k	instantaneous voltage at phase k
X_s	synchronous reactance
a	number of parallel branches
e	transient back-EMF
f	frequency
g	air gap thickness
h	coil thickness
h_M	PM thickness
h_{ry}	rotor yoke thickness

h_{sy}	stator yoke thickness
h_t	tooth height
h_w	wedge height
k_P	power constant
k_T	torque constant
k_M	ratio of PM width to pole pitch
k_e	PM surface loss density
k_f	coil fill factor
k_{ff}	form factor
k_{le}	leakage coefficient
k_{p1}	winding pitch factor
k_{r1}	AC resistance ratio for the fundamental harmonic
k_s	stacking factor
k_t	ratio of tooth width to slot pitch
k_{ts}	ratio of slot height to slot width
k_{w1}	coil factor for 1st harmonic
l	machine length
l_{adj}	coil bending length
l_c	coil total length
l_e	averaged half-length of the total end coils
l_{ef}	machine effective length
m	number of machine phases
m_F	total weight of iron for the active parts
m_M	total weight of PM
m_S	total weight of stator copper
m_T	total weight of the active parts
n_N	rated speed
n_r	number of rotors
n_s	number of stator segments
n_{st}	number of machine stages
r	cylindrical coordinate
r_a	average radius
r_i	inner radius
r_o	outer radius
p	pole number
p_M	PM specific loss density
p_{conv}	converter rated loss
p_s	pole number per segment
q	number of coils per phase per pole
s	slip
t	time or temperature
w	coil width
z	cylindrical coordinate
α	voltage drop ratio
ε	error

η_{dt}	drive train efficiency
η_{gea}	gearbox efficiency
η_{gen}	generator efficiency
η_{con}	converter efficiency
θ	cylindrical coordinate
θ_p	pole pitch in radian
κ	voltage drop ratio
μ_0	vacuum permeability
ρ_{av}	machine average density
ρ_{cu}	copper density
ρ_{cu_t}	copper density at operating temperature
ρ_{fe}	iron density
ρ_M	PM density
σ	ratio of inner diameter to outer diameter
τ_p	pole pitch in mm
τ_s	slot pitch in mm
ω_M	mechanical angular speed in rad
ω_E	electrical angular speed in rad

A.2   Abbreviations

1R	one rotor
1S	one stage
2D	two dimensions
2R	two rotors
2S	two stage
3D	three dimensions
3S	three stage
AF	axial flux
BDFG	brushless doubly-fed induction generator
CA	conventional array
DFG	doubly-fed induction generator
EEG	electrically excited synchronous generator
EL	electric load
FEA	finite element analysis
FEM	finite element method
FFT	fast Fourier transformation
GA	genetic algorithm
HA	Halbach array
HTS	high temperature superconducting
IGBT	insulated-gate bipolar transistor
MMF	megneto-motive force
MS	multi-stage
PM	permanent magnet
PMG	permanent magnet generator
RF	radial flux
SCG	squirrel-cage induction generator
SFEA	static finite element analysis
TF	transverse flux
TFEA	transient finite element analysis
THD	total harmonics distortion
WECS	wind energy conversion system
WRG	wound-rotor induction generator
dd	direct-driven
ddT	direct-driven drive train
hs	high speed
iPMG	ironless permanent magnet generator
ls	low speed
mg	multi-stage gearbox
mgT	multi-stage geared drive train
ms	medium speed
sg	single-stage gearbox
sgT	single-stage geared drive train

Appendix B

Electrical Steel Datasheet

The used electrical steel is DW460-50. Its BH table and BP curve are given below. Note that the BP curve is not available, therefore the BP curve is taken from another electrical steel which has similar magnetic properties as DW460-50.
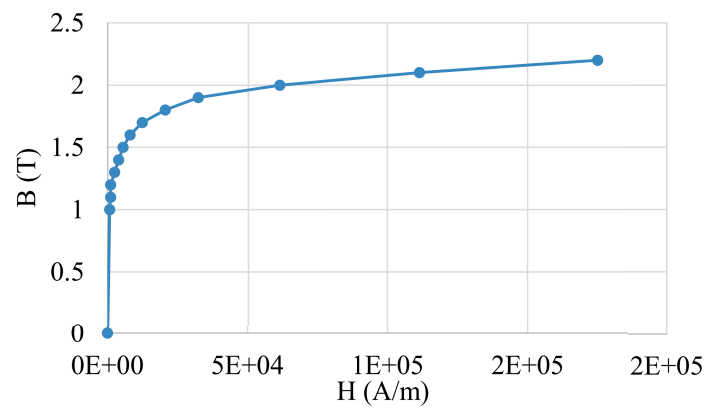
B.1 BH curve

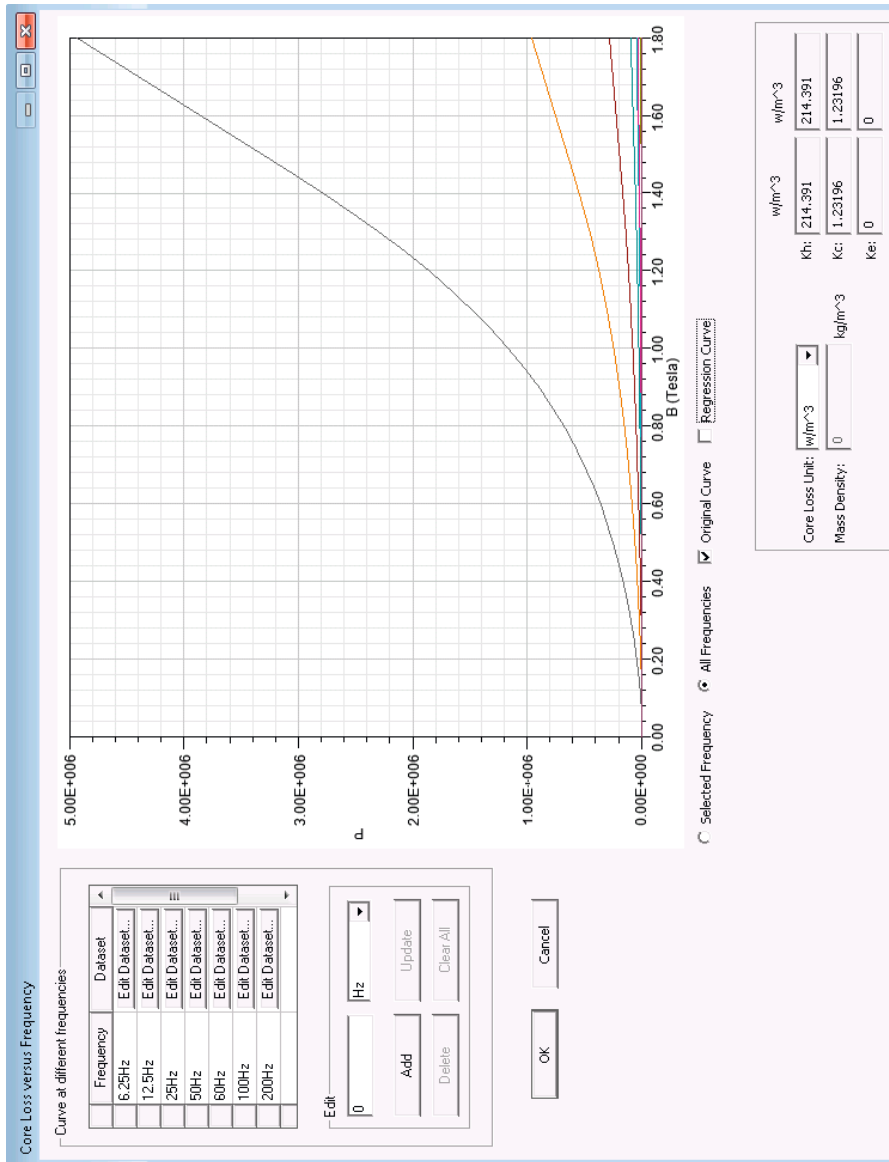Figure B.1: Electrical steel BH curve.

B.2 BP curve

Figure B.2: Electrical steel BP curve.

135

Appendix C

Scientific Computing Lab

A scientific computing lab of Elkraft NTNU was built during the execution of this project. This lab consists of four local workstations and one computing server. It is also possible to access to the NOTUR super computers for ultra large calculations. The layout and configuration of this lab are given below.
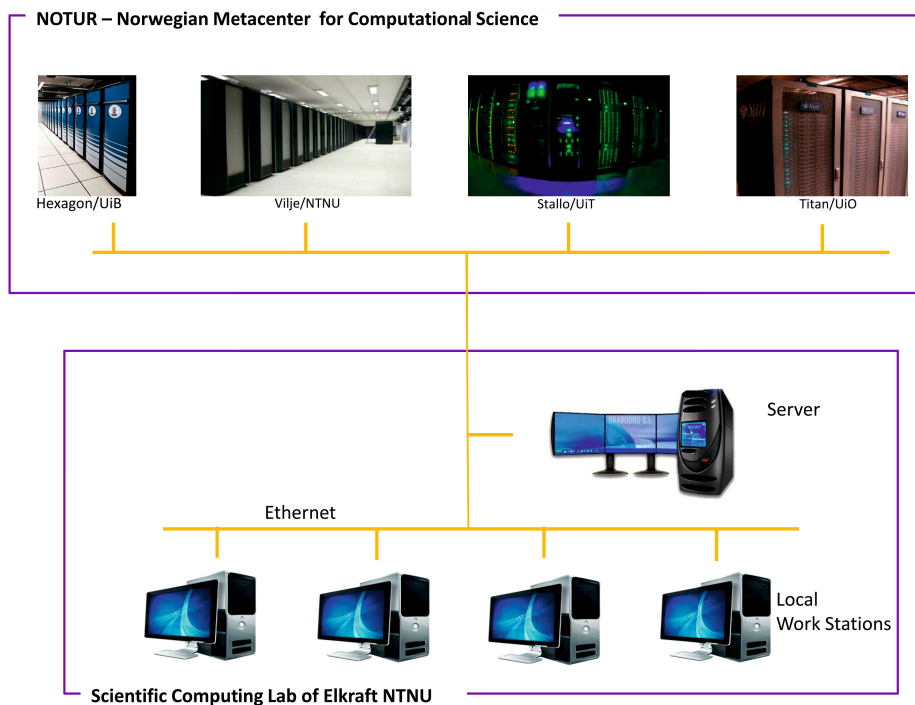

Figure C.1: Computing lab.

Local workstations: Intel Xeon X5687@3.60GHz (two processors, four cores each); Windows 7 Enterprise.

Server: AMD Opteron 6174@2.2GHz (four processors, 12 cores each); 128 GB RAM; Windows Server 2008 R2 Enterprise.

Vilje: Number of nodes 1404, 16 cores per node, total number of cores 22464; 32GB RAM per node; SUSE Linux Enterprise Server 11.

Appendix D

Lab Test

It is expensive to build an iPMM that can show the main design features for the offshore application, therefore, an axial-flux PM generator built by SmartMotor [139] was used to validate the key parts of the modelling approach.
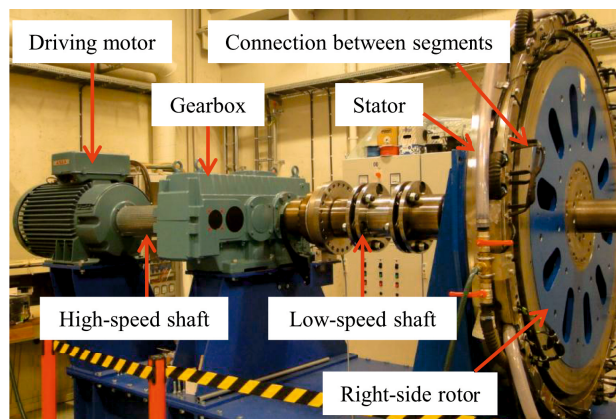
D.1 Test setup

Figure D.1: Test setup.

The test setup (Figure D.1) consists of an induction motor (driving motor), a gear box (to step down the speed), the test machine, and the corresponding mechanical couplings. Because of the limitation in the gear ratio, the maximal speed of the test machine is limited to approximate 50% of its rated speed, i.e. 38 rpm. It is possible to drive the induction motor to over speed, so that to achieve higher speed at the low-speed shaft, however, this is not tried due to the concern on the reliability of this aged gearbox.

In a pre-running check, it is found that there is a fault in the cooling pipe. So only no-load test was conducted.

D.2 Test machine

D.2.1 Machine topology

This SmartMotor machine is named AX50. It has 48 poles and 63 coils. According to the symmetry, this machine can be divided into three identical sub-machines (Figure D.2). Each sub-machine has 16 poles and 21 coils. This machine is a type of 2R-CA-AFPMG. The stator is segmented into 9 segments. In one segment, the numbers of coils per phase are not same. By repeating this irregularity, each phase has the same number of coils in one sub-machine. The coil is made of rectangular wires.
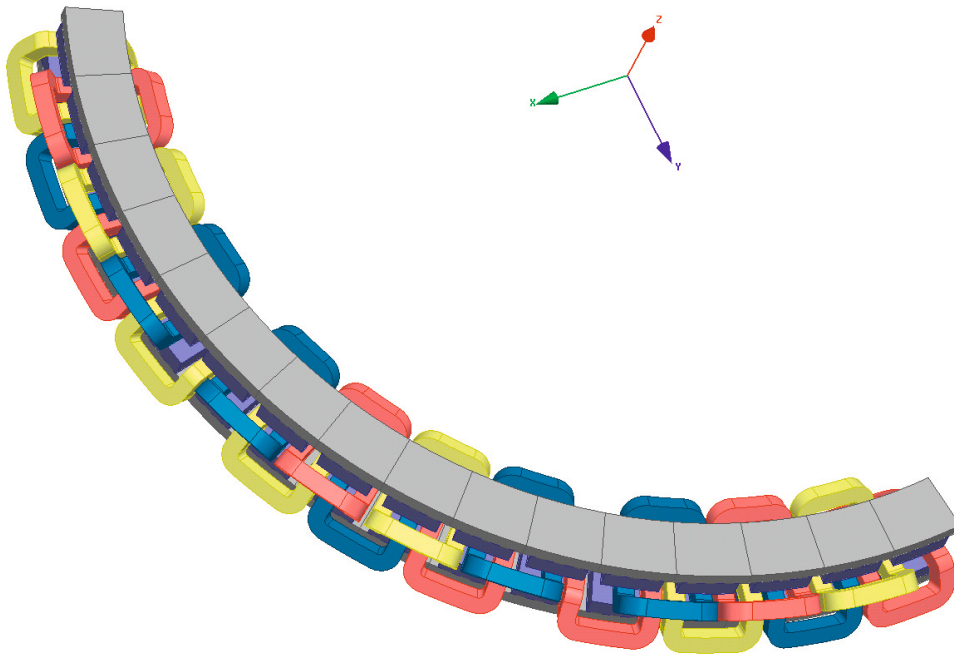

Figure D.2: Topology of one third AX50.

139

D.2.2 Specification

The specification at the 38 rpm is "converted" from its specification for rated speed (74 rpm).

Table D.1: Prototype specification.

| Parameters	Value
Rated power, kW	23
Number of phases	3
Rated speed, rpm	38
Winding connection	Y
Rated line voltage, V	128
Rated current, A	110
Synchronous reactance, pu	0.33
Winding DC resistance, Ω	0.19
Power factor	0.965
Number of poles	48
Number of stator segments	9
Number of coils per segment	7
Number of turns per coil	20
Number of parallel branches	1
PM(N35H) B_r at room temperature, T	1.2
Permeability of PM	1.05
Outer diameter, mm	1556
Thickness of the air gap, mm	3.5
PM thickness, mm	28
Thickness of the rotor yoke, mm	20
Ratio of PM width to pole pitch	0.8
Coil width, mm	30
Coil thickness, mm	37
Coil active length, mm	94.1
Coil bending length, mm	38.6
PM mass, kg	116
Mass of rotor yoke (S355J2G3), kg	582
Copper mass, kg	255
Bearing mass, kg	16
Structure mass, kg	1169
Total mass, kg	2138
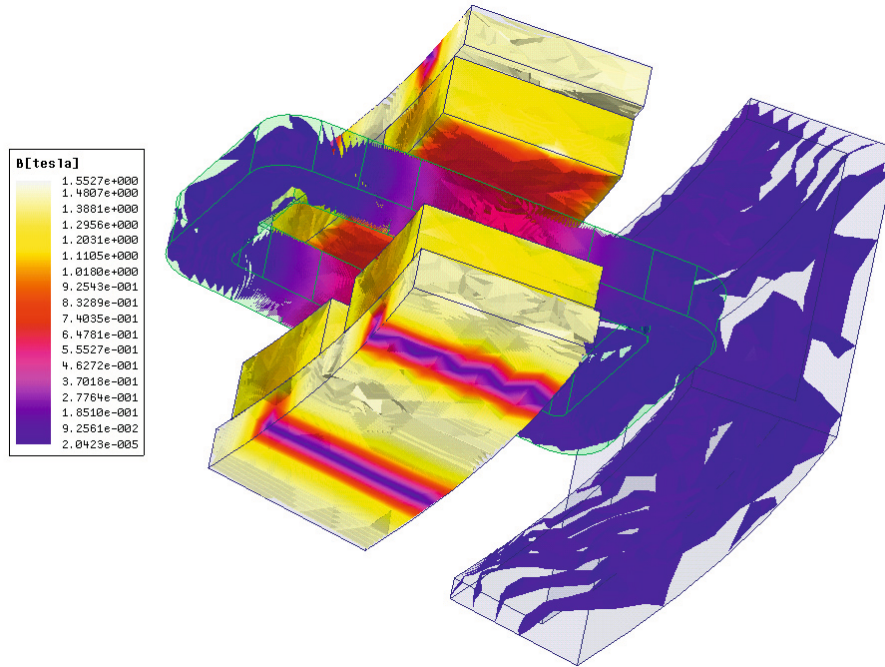
Figure D.3: AX50 FEA model (Note the part on the right side is the steel support of the winding).

D.2.3 3D FEA model

A pole pair is modelled in the field and inductance calculations. The BH curve of the rotor yoke (S355J2G3) is not available. therefore, the practical used BH curve is given in Figure D.4. The FEA tool is Maxwell 3D 16.0.0 [103].
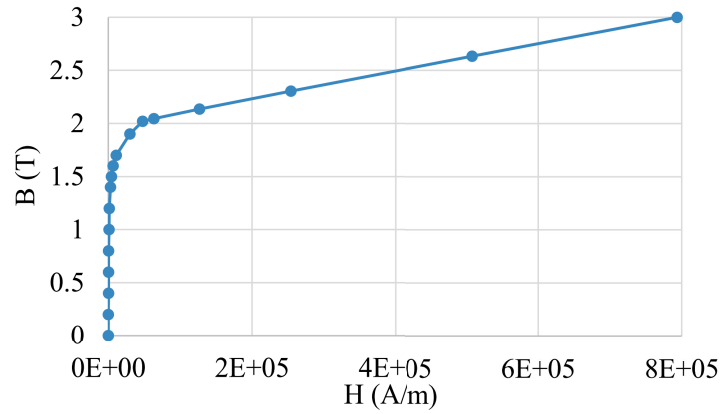
Figure D.4: Rotor yoke BH curve.

D.3 Measurements

D.3.1 Back-EMF

The back-EMF was measured by leaving the generator terminal open-circuit and measuring the induced voltages at different speeds (D.5). The instrument is Tektronix TDS 2014. At the original test setup, the maximal rotating speed is limited to 40 rpm due to the constraint at the gear ratio of the gearbox. The curve fitting of Figure D.6 shows the clear linear relationship between the back-EMF and speed. The constant in the fitting equation can be considered as the measurement error.

Figure D.5: Back-EMF at 38 rpm.

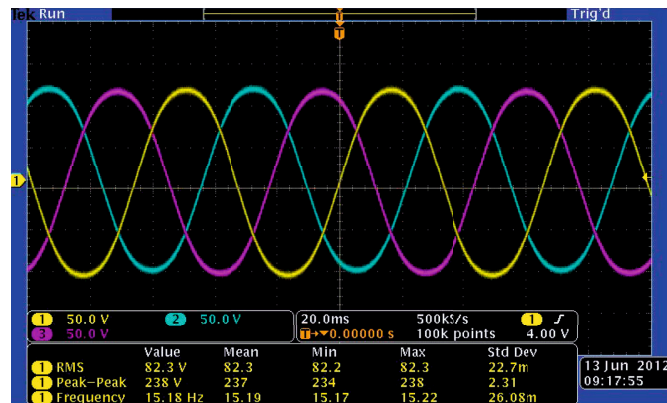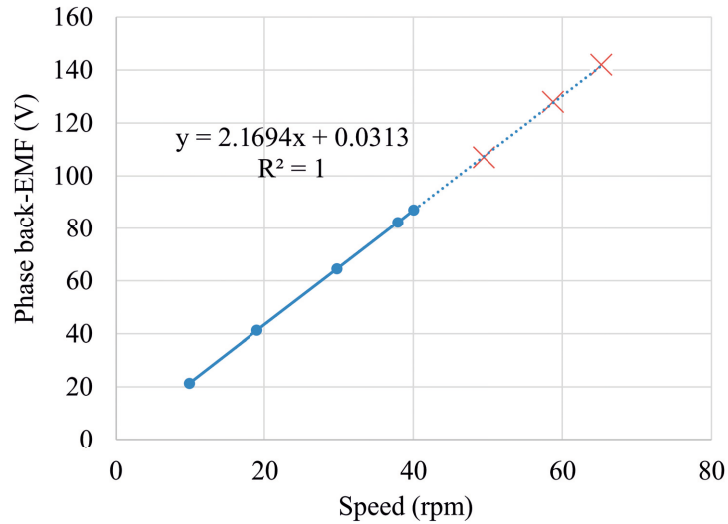Figure D.6: Phase back-EMF vs. speed (Round dots are measured back-EMFs with the original test setup, crossings are the measured back-EMFs with upgraded test setup).

Lately, the test setup was upgraded (Section C.3.3) so that it was possible to test at high speed. The measured back-EMFs are given as crossings in Figure D.6. It was expected that the measured back-EMFs at high speed would be lower than the values estimated with the fitting curve (the dotted extension of the solid line), because rectangular wire is used in this machine, and there will be more eddy current loss at high speed, the terminal voltage is therefore expected to be reduced. However, this is not observed.

D.3.2 Inductance

Each phase self-inductance was measured by leaving the other two disconnected and measuring the inductance (@50 Hz) between the phase input and the neutral point. The instrument is a RCL meter (PM6306 Programmable automatic RCL-meter). The measured results are given in Table D.2. Note measurement includes the inductance of the connection cable, which is estimated to be 0.01 mH at average. Therefore, the averaged self-inductance per phase is 1.80 mH.

Table D.2: Measured inductances.

A phase	B phase	C phase
1.810 mH	1.795 mH	1.820 mH

D.3.3 Eddy current loss in the winding

As an attempt to investigate the eddy current loss in the rectangular wires, it was tried to measure the induced eddy current loss in the winding. The test plan was to replace the stator with a dummy one. The dummy stator was made of a non-conducting material (actually high-density foam, as shown in Figure D.7). Two no-load measurements are needed. First run the machine with normal stator at rated speed (prefer high speed, because of more measurable eddy current loss), record the shaft torque. Then run the machine with dummy stator at rated speed, record the shaft torque. The shaft power difference of the above two no-load tests gives the eddy current loss in the winding.

Figure D.7: One part (1/18) of the dummy stator.

To be possible to run the machine at high speed, the original test setup was upgraded, and the original torque sensor was replaced with a more accurate one. The upgraded test setup is shown in Figure D.8. This test plan was lately cancelled, because the workshop does not have the capability to replace the stator, and there is no budget to pay external resources to do it.
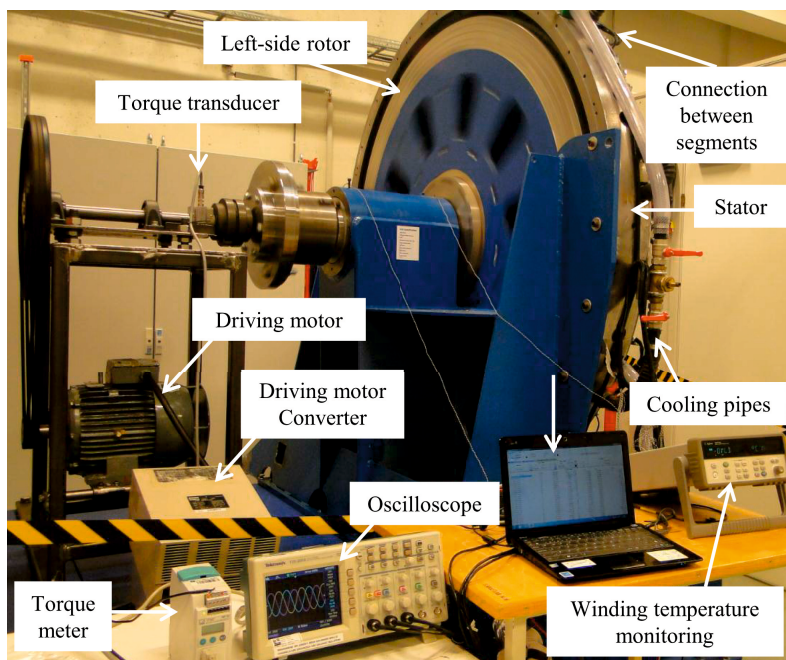
Figure D.8: The upgraded test setup.

Bibliography

[1] Commission of the European Communities, *Offshore wind energy: action needed to deliver on the energy Policy objectives for 2020 and beyond*, Communication to the European Parliament 2008, COM(2008) 768.

[2] E. Spooner, P. Gordon, J. R. Bumby, and C. D. French, "Lightweight ironless-stator PM generators for direct-drive wind turbines," *Proc. Inst. Elec. Eng. Elec. Power Appl.*, vol. 152, no. 1, pp. 17-26, 2005.

[3] A. S. McDonald, M. A. Mueller, and H. Polinder, "Structural mass in direct-drive permanent magnet electrical generators," *EWEC2007*, Italy.

[4] M. A. Mueller and A. S. Mcdonald, "A Lightweight low-speed permanent magnet electrical generator for direct-drive wind turbines," *Wind Energy*, vol. 12, no. 8, pp. 768-780, 2009.

[5] H. Kobayashi, Y. Doi, K. Miyata, and T. Minowa, "Design of the axial-flux permanent magnet coreless generator for the multi-megawatts wind turbine," *EWEC2009*, France.

[6] W. Fei and P. C. K. Luk, " "Plastic" electric motors: a viable solution for axial flux machines," *ISIE2002*, Italy, vol. 1, pp. 1-10.

[7] Societe Nationale Industrielle Aerospatiale, "Flywheel for artificial satellites," French Patent FR6924210, 16 July 1969.

[8] C. Gabrys, "Wind turbine," U.S. Patent 7042109 B2, 8 May 2006.

[9] G. H. Jang and J. H. Chang, "Development of an axial-gap spindle motor for computer hard disk drives using PCB winding and dual air gaps," *IEEE Tran. Magn.*, vol. 38, No. 5, pp. 3297-3299, 2002.

[10] T. F. Chan and L. L. Lai, "An axial-flux permanent-magnet synchronous generator for a direct-coupled wind-turbine system," *IEEE Tran. Energy Convers.*, vol. 22, No. 1, pp. 86-95, 2007.

[11] S. M. Hosseini, M. Agha-Mirsalim, and M. Mirzaei, "Design, prototyping, and analysis of a low cost axial-flux coreless permanent-magnet generator," *IEEE Tran. Magn.*, vol. 44, No. 1, pp. 75-80, 2008.

[12] J. F. Gieras, R. J. Wang, and M. J. Kamper, *Axial flux permanent magnet brushless machines*, Springer-Verlag, 2nd ed., 2008.

[13] W. Fei and P. C. K. Luk, "Design and performance analysis of a high-speed air-cored axial-flux permanent-magnet generator with circular magnets and coils," *IEMDC2009*, USA, vol. 1, pp. 1617-1624.

[14] H. C. Lovatt, V. S. Ramsden, and B. C. Mecrow, "Design of an in-wheel motor for a solar-powered electric vehicle," *Proc. Inst. Elec. Eng. Elec. Power Appl.*, vol. 145, No. 5, pp. 402-408, 1998.

[15] J. R. Bumby and R. Martin, "Axial-flux permanent-magnet air-cored generator for small-scale wind turbines," *Proc. Inst. Elec. Eng. Elec. Power Appl.*, vol. 152, No. 5, pp. 1065-1075, 2005.

[16] F. G. Capponi, R. Terrigi, F. Caricchi, and L. Del Ferraro, "Active output voltage regulation for an ironless axial-flux PM automotive alternator with electromechanical flux weakening," *IEEE Tran. Ind. Appl.*, vol. 45, No. 5, pp. 1785-1793, 2009.

[17] J. F. Eastham, F. Profumo, A. Tenconi, R. Hill-Cottingham, P. Coles, *et al.*, "Novel axial flux machine for aircraft drive: design and modeling," *IEEE Trans. Magn.*, vol. 38, no. 5, pp. 3003-3005, 2002.

[18] N. F. Lombard and M. J. Kamper, "Analysis and performance of an ironless stator axial flux PM machine," *IEEE Trans. Energy Convers.*, vol. 14, No. 4, pp. 1051-1056, 1999.

[19] J. A. Stegmann and M. J. Maarten, "Design aspects of double-sided rotor radial flux air-cored permanent-magnet wind generator," *IEEE Tran. Ind. Appl.*, vol. 47, No. 2, pp. 767-778, 2011.

[20] F. Caricchi, F. Crescimbini, and A. Di Napoli, "Prototype of innovative wheel direct drive with water-cooled axial-flux Pm motor for electric vehicle applications," *APEC1996*, USA, vol. 2, pp. 764-770.

[21] A. S. McDonald, M. Benatmane, and M. A. Mueller, "A multi-stage axial flux permanent magnet machine for direct drive wind turbines," *IET Conf. Renewable Power Generation*, UK, 2011.

[22] T. S. El-Hasan, P. C. K. Luk, F. S. Bhinder, and M. S. Ebaid, "Modular design of high-speed permanent-magnet axial-flux generators," *IEEE Trans. Magn.*, vol. 36, no. 5, pp. 3558-3561, 2000.

[23] F. Caricchi, F. Crescimbini, O. Honorati, G. L. Bianco, and E. Santini, "Performance of coreless-winding axial-flux permanent-magnet generator with power output at 400 Hz, 3000 r/min," *IEEE Trans. Ind. Appl.*, vol. 34, No. 6, pp. 1263-1269, 1998.

[24] R. Wang, M. J. Kamper, K. V. D. Westhuizen, and J. F. Gieras, "Optimal design of a coreless stator axial flux permanent-magnet generator," *IEEE Trans. Magn.*, vol. 41, no. 1, pp. 55-64, 2005.

[25] Z. Zhang, A. Matveev, R. Nilssen, and A. Nysveen, "Large-diameter ironless permanent magnet generator for offshore wind power application," *ICEM2012*, France, pp. 684-690.

[26] A. S. McDonald, N. Al-Khayat, D. Belshaw, M. Ravlious, A. Kumaraperumal, A. M. Benatamane, *et al.*, "1MW multi-stage air-cored permanent magnet generator for wind turbines," *PEMD2012*, UK.

[27] W. Wang, K. W. E. Cheng, K. Ding, and L. C. Meng, "A novel approach to the analysis of the axial-flux permanent-magnet generator with coreless stator supplying a rectifier load," *IEEE Trans. Magn.*, vol. 47, no. 10, pp. 2391-2394, 2011.

[28] M. Aydin, S. Huang, and T. A. Lipo, "Axial flux permanent magnet disc machines: a review," Research Report of University of Wisconsin-Madison, USA, 2004.

[29] F. G. Capponi, G. D. Donato, and F. Caricchi, "Recent advances in axial-flux permanent-magnet machine technology," *IEEE Trans. Ind. Appl.*, vol. 48, no. 6, pp. 2190-2205, 2012.

[30] S. Javadi and M. Mirsalim, "A coreless axial-flux permanent-magnet generator for automotive applications," *IEEE Trans. Magn.*, vol. 47, no. 12, pp. 4591-4598, 2008.

[31] S. Sadeghi and L. Parsa, "Multiobjective design optimization of five-phase Halbach array permanent-magnet machine," *IEEE Trans. Magn.*, vol. 47, no. 6, pp. 1658-1666, 2011.

[32] T. J. Woolmer and M. D. McCulloch, "Analysis of the yokeless and segmented armature machine," *IEMDC2007*, Turkey, vol. 1, pp. 704-708.

[33] S. M. Sharkh and S. H. Lai, "Slotless PM brushless motor with helical edge-wound laminations," *IEEE Trans. Energy Convers.*, vol. 24, no. 3, pp. 594-598, 2009.

[34] Z. Zhang, A. Matveev, S. Øvrebø, R. Nilssen, and A. Nysveen, "Review of modeling methods in electromagnetic and thermal design of permanent magnet generators for wind turbines," *ICCEP2011*, Italy, pp. 377-382.

[35] D. C. Hanselman, *Brushless permanent magnet motor design*, Magna Physics Pub, 2nd ed., 2006.

[36] J. R. Bumby, R. Martin, M. A. Mueller, E. Spooner, N. L. Brown, and B. J. Chalmers, "Electromagnetic design of axial-flux permanent magnet machines," *Proc. Inst. Elec. Eng. Elec. Power Appl.*, vol. 151, no. 2, pp. 151-160, 2004.

[37] Z. Q. Zhu, D. Howe, E. Bolte, and B. Ackermann, "Instantaneous magnetic field distribution in brushless permanent magnet dc motors, part I: open-circuit field," *IEEE Tran. Magn.*, vol. 29, no. 1, pp. 124-135, 1993.

[38] H. Jussila, *Concentrated winding multiphase permanent magnet machine design and electromagnetic properties-case axial flux machine*, Doctoral dissertation, Lappeenranta University of Technology, pp. 33-76, 2009.

[39] P. Kurronen, *Torque vibration model of axial-flux surface-mounted permanent magnet synchronous machine*, Doctoral dissertation, Lappeenranta University of Technology, pp. 34-50, 2003.

[40] J. K. Tangudu, T. M. Jahns, and A. EL-Refaie, "Lumped parameter magnetic circuit model for fractional-slot concentrated-winding interior permanent magnet machines," *ECCE2009*, Canada, pp. 2423-2430.

[41] A. Boglietti, *et al.*, "Evolution and modern approaches for thermal analysis of electrical machines," *IEEE Tran. Ind. Electro.*, vol. 56, no. 3, pp. 871-882, 2009.

[42] R. Tao and E. Wang, "A new boundary element method for calculating the magnetic field of permanent magnetic machine," *ICEMS2001*, China, pp. 1181-1183.

[43] T. C. O'Connel, *An investigation of boundary-based field analysis method for electric machines: the Schwartz-Christoffel and boundary element methods*, Doctoral dissertation. University of Illinois at Urbana-Champaign, 2008.

[44] T. C. O'Connel and P. T. Krein, "A time-harmonic three-dimensional vector boundary element model for electromechanical devices," *IEEE Tran. Energy Convers.*, vol. 25, no. 3, pp. 606-618, 2010.

[45] Integrated Engineering Software, available at: `http://www.integratedsoft.com`, last access: 16 Apr. 2014.

[46] N. Ottosen and H. Petersson, *Introduction to the finite element method*, Prentice Hall ISBN 0-13-473877-2, 1992.

[47] Commercial electromagnetic modelling codes, available at: `http://emclab.mst.edu/csoft/index.html`, last access: 16 Apr. 2014.

[48] T. Yamada, "Development plan for JMAG," *JMAG Users Conf.*, Japan, 2009.

[49] M. Polikarpova, P. Roytta, J. Alexandrova, S. Semken, J. Nerg, and J. Pyrhonen, "Thermal design and analysis of a direct-water cooled direct drive permanent magnet synchronous generator for high-power wind turbine application," *ICEM2012*, France, pp. 1488-1495.

[50] G. Airoldi, "Computations on heat transfer in axial flux permanent magnet machines," *ICEM2008*, Portugal.

[51] C. H. Lim, "2D lumped-parameter thermal modeling of axial flux permanent magnet generators," *ICEM2008*, Portugal.

[52] Z. Zhang, A. Matveev, S. Øvrebø, R. Nilssen, and A. Nysveen, "State of the art in generator technology for offshore wind energy conversion systems," *IEMDC2011*, Canada, pp. 1131-1136.

[53] Z. Zhang, A. Chen, A. Matveev, R. Nilssen, and A. Nysveen, "High-power generators for offshore wind turbines," *Energy Procedia*, vol. 35, pp. 52-61, 2013.

[54] A. D. Hansen and L. H. Hansen, "Wind turbine concept market penetration over 10 years (1995-2004)," *Wind Energy*, vol. 10, issue. 1, pp. 81-97, 2007.

[55] H. Li and Z. Chen, "Overview of different wind generator systems and their comparisons," *IET Renewable Power Generation*, vol. 2, no. 2, pp. 123-138, 2008.

[56] G. Shrestha, H. Polinder, D. Bang, and J. A. Ferreira, "Review of energy conversion system for large wind turbines," *EWEC2008*, Belgium.

[57] R. C. Bansal, "Three-phase self-excited induction generators: an overview," *IEEE Trans. on Energy Convers.*, vol. 20, no. 2, pp. 292-299, 2005.

[58] G. Bywaters, V. John, J. Lynch, P. Mattila, G. Northon, and J. Stowell, *Northern power systems WindPact drive train alternative design study report*, NREL report, pp. A-13 to A-18, 2005.

[59] L. H. Hansen, L. Helle, F. Blaabjerg, *et al.*, *Conceptual survey of generators and power electronics for wind turbines*, Risø National Laboratory 2001. Risø-R-1205(EN), pp. 41-46.

[60] R. A. McMahon, P. C. Roberts, W. Wang, and P. J. Tavner, "Performance of BDFM as generator and motor," *Proc. Inst. Elec. Eng. Elec. Power Appl.*, vol. 153, issue. 2, pp. 289-299, 2006.

[61] R. A. McMahon, X. Wang, P. J. Tavner, P. C. Roberts, and M. Jagiela, "The BDFM as a generator in wind turbines," *PEMC2006*, Slovenia, pp. 1859-1865.

[62] T. Logan, J. Wariington, S. Shao, and R. McMahon, "Practical development of the brushless doubly-fed machine in a medium scale wind turbine," *PEDS2009*, Taipei, pp. 470-474.

[63] A. Grauers, *Design of direct-driven permanent-magnet generators for wind turbines*, Doctoral dissertation, Chalmers University of Technology, Sweden, 1996.

[64] P. Lampola, *Directly driven, low-speed permanent-magnet generators for wind power applications*, Doctoral dissertation, Helsinki University of Technology, Finland, 2000.

[65] E. Spooner and B. J. Chalmers, "TORUS: a slotless, toroidal-stator, permanent magnet generator," *Proc. Inst. Elec. Eng. Elec. Power Appl. B*, vol. 139, no. 6, pp. 497-506, 1992.

[66] L. Soderlund, A. Koski, H. Vihriala, J. T. Eriksson, and R. Perala, "Design of an axial flux permanent magnet wind power generator," *Proc. of IEE Conf. of Electrical Machines and Drives*, UK, pp. 224-228, 1997.

[67] H. Weh, "Transverse-flux(TF) machines in drive and generator application," *IEEE Symposium on Electric Power Eng.*, Sweden, 1995.

[68] D. Bang, H. Polinder, G. Shrestha, and J. A. Ferreira, "Review of generator systems for direct-drive wind turbines," *EWEC2008*, Belgium.

[69] E. Borgen, "Direct drive generator/motor for a windmill/hydropower plant/vessel where the generator/motor is configured as a hollow profile and method to assemble such a windmill/hydropower plant," Patent No., WO 2007/043894, 19 Apr. 2007.

[70] Wind turbine list of main manufacturers, available at: http://www.thewindpower.net, last access: 16 Apr. 2014.

[71] D. Bang, H. Polinder, G. Shrestha, and J. A. Ferreira, "Possible solutions to overcome drawbacks of direct-drive generator for large wind turbines," *EWEC2009*, France.

[72] G. Shrestha, H. Polinder, D. Bang, A. K. Jassal, and J. A. Ferreira, "Investigation on the possible use of magnetic bearings in large direct drive wind turbines," *EWEC2009*, France.

[73] S. Engstrom, B. Hernnas, C. Parkegren, and S. Waernulf, "Development of NewGen-a new type of direct-drive generator," *EWEC2007*, Italy.

[74] C. J. A. Versteegh, "Design of Zephyros Z72 wind turbine with emphasis on the direct drive PM generator," *NORPIE2004*, Norway.

[75] G. Bohmeke, "Direct drive, geared drive, intermediate solutions-comparison of design features and operating economics," *EWEC1997*, Ireland.

[76] S. Siegfriedsen and G. Bohmeke, "Multibrid technology-a significant step to multi-megawatt wind turbines," *Wind Energy*, vol. 1, issue. 2, pp. 89-100, 1998.

[77] M. Rees and J. Sancho, "Rotor schemes and a new structural design for a very large rotor blade for the multibrid OWECS," *3rd Offshore Wind Energy in Mediterranean and other European Seas (OWEMES 2000)*, Italy, 2000.

[78] H. Li and Z. Chen, "Optimization of multibrid permanent-magnet wind generator systems," *IEEE Trans. on Energy Convers.*, vol. 24, no. 1, pp. 82-92, 2009.

[79] D. W. Dudley, J. Sprengers, *et al.*, *Gear motor handbook*, ISBN 3-540-58988-0, Springer-Verlag Berlin Heidelberg, pp.314-325, 1995.

[80] E. Hau, *Wind turbines, fundamentals, technologies, application, economics*, Springer Berlin Heidelberg, New York, pp.297-299, 2006.

[81] T. Karna and R. Sakki, "Wind power generators," *Wind Customer Expert Days*, Germany, 2010.

[82] H. Li and Z. Chen, "Design optimization and evaluation of different wind generator systems," *ICEMS2008*, China, pp. 2396-2401.

[83] V. D. Colli, F. Marignetti, and C. Attaianese, "2-D mechanical and magnetic analysis of a 10 MW doubly fed induction generator for direct-drive wind turbines," *IECON09*, Portugal, pp. 3863-3867.

[84] V. D. Colli, F. Marignetti, and C. Attaianese, "Feasibility of a 10 MW doubly fed induction generator for direct-drive wind turbines," *Proc. IEEE PES/IAS Conf. Sustainable Alternative Energy*, Spain, 2009, pp. 1-5.

[85] V. D. Colli, F. Marignetti, and C. Attaianese, "Analytical and multiphysics approach to the optimal design of a 10-MW DFIG for direct-drive wind turbines," *IEEE Trans. Ind. Electro.*, vol.59, no. 7. pp. 2791-2799, 2012.

[86] H. Polinder, D. Bang, R. P. J. O. M. Van Rooij, A. S. McDonald, and M. A. Mueller, "10 MW wind turbine direct-drive generator design with pitch or active speed stall control," *IEMDC2007*, Turkey, pp. 1390-1395.

[87] Y. Alexandrova, S. Semken, M. Polikarpova, and J. Pyrhonen, "Defining proper initial geometry of an 8 MW liquid-cooled direct drive permanent magnet synchronous generator for wind turbine applications based on minimizing mass," *ICEM2012*, France, pp. 1250-1255.

[88] M. Lesser and J. Muller, "Superconductor technology-generating the future of offshore wind power," *Renewable Energy World Conf. and Exhib.*, Germany, 2009.

[89] A. Abrahamsen, N. Magnusson, B. Jenson, and M. Runde, "Large superconducting wind turbine generators," *Energy Procedia*, vol. 24, pp. 60-67, 2012.

[90] X. Li, *et al.*, "Design of a high temperature superconducting generator for wind power applications," *IEEE Trans. Applied Supercond.*, vol. 21, no. 3, pp. 1155-1158, 2011.

[91] S. F. Philp, "The vacuum-insulated, varying-capacitance machine," *IEEE Trans. Electr. Insul.*, vol. EI-12, no. 2, p.130-136, 1977.

[92] R. O'Donnell, N. Schofield, A. C. Smith, and J. Cullen, "Design concepts for high-voltage variable-capacitance DC generators," *IEEE Trans. Ind. Appl.*, vol.45, no. 5, pp. 1778-1784, 2009.

[93] Close up - Sway Turbine's ST10 10MW turbine, available at: `http://www.windpowermonthly.com`, last access: 16 Apr. 2014.

[94] G. Shrestha, H. Polinder, D. Bang, and J. A. Ferreia, "Structural flexibility: a solution for weight reduction of large direct-drive wind-turbine generators," *IEEE Trans. Energy Convers.*, vol. 25, no.3, pp. 732-740, 2010.

[95] The Switch, "Specifications of low speed permanent magnet generators," available at: `http://www.theswitch.com`, last access: 16 Apr. 2014.

[96] XEMC Darwind XD115 5 MW offshore data sheet, available at: `http://www.darwind.nl/`, last access: 16 Apr. 2014.

[97] SWAY Turbine ST10, available at: `http://www.swayturbine.no/`, last access: 16 Apr. 2014.

[98] R. Wrobel, D. Salt, A. Griffo, N. Simpson, and P. Mellor, "Derivation and scaling of AC copper Loss in thermal modeling of electrical machines," *IEEE Trans. Ind. Electro.*, vol. 61, no. 8, pp. 4412-4420, 2013.

[99] H. Li and Z. Chen, "Design optimization and site matching of direct-drive permanent magnet wind power generator systems," *Renewable Energy*, vol. 34, issue. 4, pp. 1175-1184, 2009.

[100] J. Pyrhonen, T. Jokinen, Valeria, and Hrabovcova, *Design of rotating electrical machines*, Wiley, 1st ed., pp. 294, 2009.

[101] A. S. McDonald, *Structural analysis of low speed, high torque electrical generators for direct drive renewable energy converters*, Doctoral dissertation, The University of Edinburgh, UK, pp. 156, 2008.

[102] D. Meeker, FEMM 4.2, available at: `http://www.femm.info`, last access: 16 Apr. 2014.

[103] Maxwell 2D and 3D, available at: `http://www.ansys.com`, last access: 16 Apr. 2014.

[104] G. Shrestha, H. Polinder, D. J. Bang, and J. A. Ferreira, "Direct drive wind turbine generator with magnetic bearing," *EWEC2007*, Germany, pp. 1-10.

[105] M. Liserre, R. Cardenas, M. Molinas, and J. Rodriguez, "Overview of multi-MW wind turbines and wind parks," *IEEE Trans. Ind. Electro.*, vol. 58, no. 4, pp. 1081-1095, 2011.

[106] Z. Q. Zhu and D. Howe, "Halbach permanent magnet machines and applications: a review," *Proc. Inst. Elec. Eng. Elec. Power Appl.*, vol. 148, no. 4, pp. 299-308, 2001.

[107] Y. Duan and D. M. Ionel, "A review of recent developments in electrical machine design optimization methods with a permanent-magnet synchronous motor benchmark study," *IEEE Trans. Ind. Appl.*, vol. 49, no. 3, pp. 1268-1275, 2013.

[108] N. Hodgins, O. Keysan, A. S. Mcdonald, and M. A. Mueller, "Design and testing of a linear generator for wave-energy applications," *IEEE Trans. Ind. Electron.*, vol. 59, no. 5, pp. 2094-2103, 2012.

[109] A. Cavagnino, M. Lazzari, F. Profumo, and A. Tenconni, "A comparison between the axial flux and the radial flux structures for PM synchronous motors," *IEEE Trans. Ind. Appl.*, vol. 38, no. 6, pp. 1517-1524, 2002.

[110] B. Boone, "Design ideas in permanent magnet generators," available at: `http://www.windpowerengineering.com/design/electrical/generators/design-ideas-permanent-magnet-generators/`, last access: 25 Mar. 2014.

[111] Boulder Wind Power, "Boulder Wind Power Advanced Gearless Drivetrain ," US DOE Wind and Water Power Program, 31 Aug. 2012.

[112] F. Caricchi, F. Crescimbini, and O. Honorati, "Modular axial-flux permanent-magnet motor for ship propulsion drives," *IEEE Trans. Energy Convers.*, vol. 14, no. 3, pp. 673-679, 1999.

[113] F. Dumas, P. Enrici, and D. Matt, "Design and comparison of two multi-disc permanent magnet motors for aeronautical application," *ICEM2012*, France, pp. 647-652.

[114] A. D. Gerlando, G. Foglia, M. F. Iacchetti, and R. Perini, "Axial flux PM machines with concentrated armature windings: design analysis and test validation of wind energy generators," *IEEE Trans. Ind. Electron.*, vol. 58, no. 9, pp. 3795-3805, 2011.

[115] Z. Zhang, A. Matveev, R. Nilssen, and A. Nysveen, "Ironless multi-stage axial-flux permanent magnet generator for offshore wind power application," *12th Joint MMM/Intermag Conf.*, USA, 2013.

[116] Z. Zhang, A. Matveev, R. Nilssen, and A. Nysveen, "Ironless permanent magnet generator for offshore wind turbines," *IEEE Trans. Ind. Appl.*, vol. 50, No. 3, pp. 1835-1846, 2014.

[117] M. A. Mueller, A. S. McDonald, and D. E. Macpherson, "Structural analysis of low speed axial-flux permanent-magnet machines," *Proc. Inst. Elec. Eng. Elec. Power Appl.*, vol. 152, no. 6, pp. 1417-1426, 2005.

[118] J. Pippuri, A. Manninen, J. Kernen, and K. Tammi, "Torque density of radial, axial and transverse flux permanent magnet machine topologies," *IEEE Trans. Magn.*, vol. 49, no. 5, pp. 2339-2342, 2013.

[119] Y. Yang, Y. Luh, and C. Cheung, "Design and control of axial-flux brushless DC wheel motors for electric vehicles - part I: multiobjective optimal design and analysis," *IEEE Trans. Magn.*, vol. 40, no. 4, pp. 1873-1882, 2004.

[120] D. G. Dorrell, S. S. Ngu, and C. Cossar, "Comparison of high pole number ultra-low speed generator designs using slotted and air-gap windings," *IEEE Trans. Magn.*, vol. 48, no. 11, pp. 3120-3123, 2012.

[121] H. Tiegna, A. Bellara, Y. Amara, and G. Barakat, "Analytical modeling of the open-circuit magnetic field in axial flux permanent-magnet machines with semi-closed slots," *IEEE Trans. Magn.*, vol. 48, no. 3, pp. 1212-1226, 2012.

[122] Norsk 10 MW havvindturbin, available at: `http://lekegrind.tumedia.no/kraft/2012/10/24/norsk-10-mw-havvindturbin`, last access: 16 Apr. 2014.

[123] Salome 6.6.0, available at: `http://www.salome-platform.org/`, last access: 16 Apr. 2014.

[124] Elmer 7.0, available at: `http://www.csc.fi/english/pages/elmer`, last access: 16 Apr. 2014.

[125] Paraview 3.14.1, available at: `http://www.paraview.org/`, last access: 16 Apr. 2014.

[126] Genetic optimization code, available at: `http://octave.sourceforge.net/`, last access: 16 Apr. 2014.

[127] T. Nakano, Y. Kawase, T. Yamaguchi, M. Nakamura, N. Nishikawa, and H. Uehara, "Thermal model with winding homogenization and FIT discretization for stator slot," *IEEE Trans. Magn.*, vol. 47, no. 12, pp. 4822-4826, 2011.

[128] D. A. Howey, *Thermal design of air-cooled axial flux permanent magnet machines*, Doctoral dissertation, Imperial College London, UK, pp. 31, 2010.

[129] J. P. Bastos, M. F. R. R. Cabreira, N. Sadowski, S. R. Arruda, and S. L. Nau, "A thermal analysis of induction motors using a weak coupled modeling," *IEEE Trans. Magn.*, vol. 33, no. 2, pp. 1714-1717, 1997.

[130] T. Iwashita, "Recent technologies for fast electromagnetic field analysis," *JMAG User Conf.*, paper No. 11, 2008.

[131] MagNet application example, "Simulating a claw-pole alternator in an automobile electrical system environment," available at: `http://www.infolytica.com/en/applications/ex0127/`, last access: 16 Apr. 2014.

[132] T. Nakano, Y. Kawase, T. Yamaguchi, M. Nakamura, N. Nishikawa, and H. Uehara, "Parallel computing of magnetic field for rotating machines on the earth simulator," *IEEE Trans. Magn.*, vol. 46, no. 8, pp. 3273-3276, 2010.

[133] Z. Chen and E. Spooner, "Grid power quality with variable speed wind turbines," *IEEE Trans. on Energy Convers.*, vol. 16, no. 2, pp. 148-154, 2001.

[134] A. Gerlando, G. Foglia, M. Lacchetti, and R. Perini, "Simulation and test results of grid connected WECSs with diode rectifiers and modular PMSGs," *ICEM2010*, Italy.

[135] F. Reis, J. Ale, F. Adegas, R. Tonkoski Jr., S. Slan, and K. Tan, "Active shunt filter for harmonic mitigation in wind turbines generators," *37th IEEE Power Electro. Specialists Conf.*, Korea, 2006.

[136] A. Singer, *External reactive power compensation of permanent magnet synchronous generator*, Doctoral dissertation, Technical University of Chemnitz, Germany, 2009.

[137] H. Akagi, E. Watanabe, and M. Aredes, *Instantaneous power theory and applications to power conditioning*, Wiley-IEEE Press, 1st ed., 2007.

[138] A. Garcdes, M. Molinas, and P. Rodriguez, "A generalized compensation theory for active filters based on mathematical optimization in ABC frame," *Electric Power Systems Research*, vol. 90, pp. 1-10, 2012.

[139] SmartMotor, `http://www.smartmotor.no/`, last access: 16 Apr. 2014.